LEAN BLOWOFF CHARACTERISTICS OF SWIRLING $H_2/CO/CH_4$ FLAMES

A Dissertation
Presented to
The Academic Faculty

by

Qingguo Zhang

In Partial Fulfillment
of the Requirements for the Degree
Doctor of Philosophy in
Aerospace Engineering

Georgia Institute of Technology

May 2008

LEAN BLOWOFF CHARACTERISTICS OF SWIRLING H_2/CO/CH_4 FLAMES

Approved By:

Dr. Tim Lieuwen, Advisor
School of Aerospace Engineering
Georgia Institute of Technology

Dr. Suresh Menon
School of Aerospace Engineering
Georgia Institute of Technology

Dr. Ben T. Zinn
School of Aerospace Engineering
Georgia Institute of Technology

Dr. Fei Han
Global Research Center
General Electric

Dr. Jerry Seitzman
School of Aerospace Engineering
Georgia Institute of Technology

Date Approved: 22 February 2008

To my wife

ACKNOWLEDGEMENTS

I would like to acknowledge the support and help of many people, without whom this thesis would not have been possible:

First of all, I would like to thank my advisor, Dr. Tim Lieuwen for his guidance and mentoring throughout my research work.

I would also like to thank my thesis committee members, Dr. Ben T. Zinn, Dr. Jerry Seitzman, Dr. Suresh Menon and Dr. Fei Han, for their insightful comments.

I am thankful for the past and present students and engineers at Aerospace Combustion Laboratory: Alex, Antonio, Arun, Ben, Bibik, Bobby, David, Dmitriy, Eugene, Gabe, JP, Mohan, Murgi, Nair, Nori, Preetham, Ping, Priya, Rajesh, Santosh S., Santosh H., Sai, Shai, Shashvat, Thao and Venkat.

The financial support from United States Department of Energy through University Turbine Systems Research is gratefully acknowledged.

Finally, I would like to thank my wife, Jingzhu, and my family for their love and support throughout my study at Georgia Tech.

TABLE OF CONTENTS

LIST OF FIGURES

SUMMARY

This thesis describes an experimental investigation of lean blowoff for H_2/CO/CH_4 mixtures in a swirling combustor. This investigation consisted of three thrusts. The first thrust focused on correlations of the lean blowoff limits of H_2/CO/CH_4 mixtures under different test conditions. It was found that a classical Damköhler number approach with a diffusion correction could correlate blowoff sensitivities to fuel composition over a range of conditions.

The second part of this thesis describes the qualitative flame dynamics near blowoff by systematically characterizing the blowoff phenomenology as a function of hydrogen level in the fuel. These near blowoff dynamics are very complex, and are influenced by both fluid mechanics and chemical kinetics; in particular, the role of thermal expansion across the flame and extinction strain rate were suggested to be critical in describing these influences.

The third part of this thesis quantitatively analyzed strain characteristics in the vicinity of the attachment point of stable and near blowoff flames. Surprisingly, it was found that in this shear layer stabilized flame, flow deceleration is the key contributor to flame strain, with flow shear playing a relatively negligible role. Near the premixer exit, due to strong flow deceleration, the flame is negatively strained – i.e., compressed. Moving downstream, the strain rate increases towards zero and then becomes positive, where flames are stretched. As the flame moves toward blowoff, holes begin to form in the flame sheet, with a progressively higher probability of occurrence as one moves

downstream. It is suggested that new holes form with a more uniform probability, but that this behavior reflects the convection of flame holes downstream by the flow.

It has been shown in prior studies, and affirmed in this work, that flames approach blowoff by first passing through a transient phase manifested by local extinction events and the appearance of holes on the flame. A key conclusion of this work is that the onset of this boundary occurs at a nearly constant extinction strain rate. As such, it is suggested that Damköhler number scalings do not describe blowoff itself, but rather the occurrence of this first stage of blowoff. Given the correspondence between this first stage and the actual blowoff event, this explains the success of classical Damköhler number scalings in describing blowoff, such as shown in the first thrust of this thesis. The physics process associated with the actual blowoff event is still unclear and remains a key task for future work.

CHAPTER 1

INTRODUCTION

1.1 Motivation

This research work is motivated by the strong interest in developing *fuel flexible,* low emissions gas turbines, which can use highly variable and potentially low quality fuels, while producing minimal air pollutants, yet still retain a stable flame

Modern gas turbines have high performance in several aspects: efficiency, reliability, and low emissions. To meet environmental restrictions, these systems are operated in a lean, premixed mode of combustion.

Currently, natural gas is the primary fuel for land-based gas turbines. While natural gas is keeping its position as a clean, effective fuel source, it can not be relied upon as the exclusive source for fueling the entire new demand for power generation of the future.

Coal is the most abundant fossil fuel source throughout the world, and the development of clean coal technologies, such as integrated gasification combined cycle (IGCC), enables the combustion of gasified solids, while maintaining aggressive emissions targets and high efficiency [1]. Depending upon the source and particular processing technique, however, the compositions of these alternative fuels, such as synthetic gas (syngas), vary in a significant range. The inherent variability in composition and chemical energy of these fuels provides one of the largest barriers towards their usage in current gas turbines. Expensive test programs and hardware modifications are currently required if there are significant changes to gas fuel properties.

Fuel variability has profound influences upon combustor operability issues, including lean blowoff. Lean blowoff is a major concern in land-based, industrial systems, where the engines are required to operate in lean conditions and reliably over a long period with minimal shutdown time[2]. Strict emissions requirements, such as those for NOx, have motivated these engines to operate a lean premixed combustion [3], in order to minimize flame temperatures for lower level of NO_x emission. Such lean operation normally requires the engines operated in the vicinity of the lean blowout point. If lean blowoff happens, it usually requires a system shutdown and restart, which increases maintenance costs and reduces engine life and availability. For fuel flexible gas turbines, variability in fuel composition influences the blowoff limits. It is a significant problem, because low emission combustion systems are typically optimized to operate based on the fuel specifications.

The objective of this research is to improve the understanding of lean blowoff in low emissions, fuel flexible gas turbines, and the development of models and predicting methods needed to design fuel flexible combustion systems. This is the main motivation behind this study.

1.2 Background

Lean premixed (LP) combustion is currently the main method used in low NOx land-based gas turbines. A lower peak flame temperature is the main focus of this approach to reduce the thermal nitrogen oxides (NOx) emissions. NOx indicates the sum of NO (nitric oxide) and NO_2 (nitrogen dioxide), which have long been identified as harmful atmospheric pollutants. There are mainly three NOx formation mechanisms, and among

them, the dominant one at high temperatures, like those found in many combustion systems, is the Zeldovich mechanism, or the thermal NOx mechanism.

For the Zeldovich mechanism, temperature has a great effect on NOx formation (NOx increase exponentially with temperature [4]). Therefore, the method to reduce NOx emissions is generally based on the scheme to reduce the peak flame temperature. For example, at a given O_2/N_2 ratio, the amount of NOx produced at a temperature of 1800 K is much lower than the NOx produced when the temperature is at 2100 K[5]. For gas turbines operated in a diffusion (non-premixed) mode, the fuel and air burn at stoichiometric equivalence ratio, which generates a higher flame temperatures and NOx emission.

Currently, the primary methods used to reduce NOx in gas turbines are water injection, gas recirculation, rich burn–quick quench–lean burn (RQL) combustion, catalytic combustion, and lean premixed combustion [6]. All these methods can significantly reduce the NOx level; however, each method has its own difficulties in design or operation. Among all these methods, lean premixed combustion is the most commonly used for power generation applications. Lean premixed combustion system can avoid stoichiometry combustion of diffusion combustion, so that it generates lower flame temperatures (below ~1800 K), where thermal NOx production is greatly reduced.

Currently, most of the lean premixed gas turbines operate with natural gas, which is mainly composed of methane. It is clear that natural gas can not be relied upon as the exclusive source for fueling the entire new demand for power generation of the future. Coal is the most abundant energy source throughout the world, and the development of clean coal technologies, such as integrated gasification combined cycle (IGCC), enables

the combustion of gasified solids, while maintaining aggressive emissions targets and high efficiency. The resulting gas mixture from the gasification process is called synthetic gas (syngas).

Syngas fuels are composed primarily of H_2, CO, and N_2, and may also contain smaller amounts of CH_4, O_2, CO_2, and other higher order hydrocarbons[7]. For these alternative fuels, depending upon the source and particular processing technique, the compositions can vary significantly.

For example, Moliere [8] presents a comparison of compositions for twelve different syngas fuels, showing that the volumetric H_2/CO ratio varies from a low of 0.33 to a high of 40, the percentage of diluents gases (e.g., N_2, CO_2, Ar) from 4 – 51%, see Table 1.

Table 1: Syngas mixtures compositions. Red and green colors indicate maximum and minimum of specie molar fractions, respectively.

	A	B	C	D	E	F	G	H	I	J	K	L
H2	24.8	37.2	35.4	34.4	14.5	8.6	61.9	22.7	34.4	44.5	32	40
CO	39.5	46.6	45	35.1	23.6	26.2	26.2	30.6	55.4	35.4	49.5	1
CH4	1.5	0.1	0	0.3	1.3	8.2	6.9	0.2	5.1	0.5	0.1	9
CO2	9.3	13.3	17.1	30	5.6	14	2.8	5.6	1.6	17.9	15.8	6
H2O	22.7	0.3	0.4	0	5.7	0	0	39.8	0	0.1	0.44	0
N2+ others	2.2	2.5	2.1	0.2	49.3	43	2.2	1.1	3.5	1.6	2.16	44

Fuel compositions have substantial effects on the properties of flames. To illustrate, two sets of CHEMKIN results (using GRI 3.0 mechanism) are included to illustrate the effects of fuel compositions. Consider first the flame speed, S_L. **Figure 1** (a) illustrates the dependence of the flame speed upon fuel composition at a fixed adiabatic flame temperature, 2000 K. The fuel composition by volume is given by the location within the triangle, where the three vertices denote pure CO, H_2 or CH_4. At each point, the mixture

equivalence ratio is adjusted such that the mixture has the given flame temperature. As expected, the high H_2 mixtures have the highest flame speeds. Note also the variation in flame speeds, in a range of 15 to. 90 cm/s, shown in **Figure 1** (a). **Figure 1** (b) shows the dependence of the chemical time, $\tau_{chem} = \alpha / S_L^2$, upon fuel composition at a fixed flame temperature 1500K, where α and S_L represents thermal diffusivity of the mixture and laminar flame speed, respectively. Note the order of magnitude variation in chemical time from the fast H_2 mixtures to the slow CO mixtures.

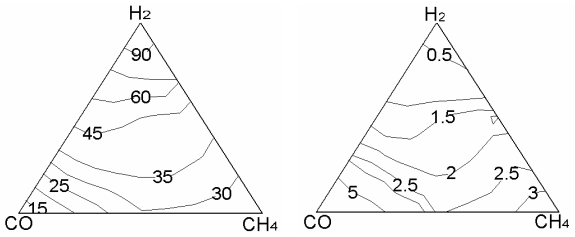

Figure 1: Dependence of flame speed (cm/s) upon fuel composition at fixed adiabatic flame temperatures of 2000 K (left); Dependence of chemical time (ms) upon fuel composition at fixed adiabatic flame temperature of 1500 K (right); at inlet temperature of 300K, pressure of 1 atm, by CHEMKIN with GRI 3.0 mechanism.

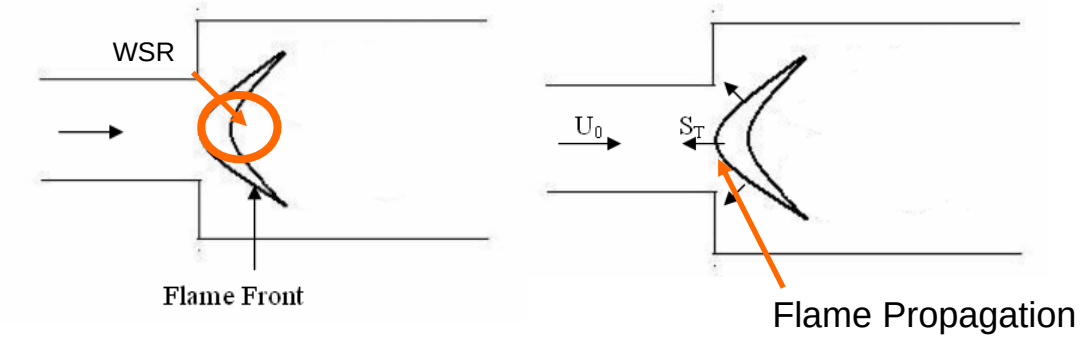

(a) (b)

Figure 2: Diagram of blowoff mechanisms

Consequently, the variety in fuel compositions substantially affects flame stabilization. Stabilization of flames in high speed flows, such as in gas turbines, has been studied for decades. Flame stabilization in practical combustor often involves a competition between the rates of the chemical reactions and the rates of turbulent diffusion of species and energy. Based on this competition, currently there are two main approaches, well stirred reactor (Damköhler number) and flame propagation models, used to model blowoff, see Figure 2.

A well stirred reactor (WSR) model assumes that flame stabilization occurs where turbulent and molecular mixing is much faster than chemical reactions, thus transport properties are not limiting phenomena. The WSR modeling approach essentially assumes that flame anchoring is limited by whether the combustion process has a sufficient residence time for combustion to occur. Several different theories or physical considerations, used in past blowout correlation studies, lead to a similar equation of the form,

$$L_1 = \frac{\tau_{res}}{\tau_{chem}} = Da \quad (1)$$

where Da represents the Damköhler number, which is defined as the ratio of flow residence time and flame chemical time. Thus the WSR model represents a competition between two characteristic time scales, the residence time and the chemical time. If the residence time is too short relative to the chemical time, lean blowoff occurs.

The other approach for correlating flame blowout limits is to assume flamelet-like combustion properties, where the stabilization mechanism is related to front propagation, rather than reactor extinction. In this case, a flame would blow off when the turbulent

flame speed is everywhere less than the local flow velocity, $S_T < U_{ref}$, where S_T denotes the turbulent flame speed. If this propagation mechanism is the controlling factor, then blowoff limits should scale with the parameter:

$$L_2 = \frac{S_T}{U_{ref}} \quad (2)$$

The propagation model focuses on a ratio of two speed scales, flow speed and turbulent flame speed. However, evaluating the turbulent flame speed brings additional complications for mixtures with widely varying compositions.

It is clear that these two mechanisms, Damköhler number and flame propagation models are distinctly different in physics. However, mathematically, these two mechanisms are similar and inter-correlated. For example, if we rewrite eqn (2) in the form of eqn (3), this equation also represents somewhat a ratio of a chemical time and flow time. This similarity leads to substantial difficulties in determining the controlling mechanism from correlations of blowoff data. So in this study, even though a Damköhler number correlation is used to correlate blowoff data (see chapter 4), but it does not mean that the physical blowoff mechanism is WSR mechanism.

$$L_2 = \frac{S_T}{U_{ref}} = \frac{S_T / l_{ref}}{U_{ref} / l_{ref}} \quad (3)$$

Compared to the study of correlating blowoff limits, the process of loss of stabilization did not receive much attention. Lean blowoff is often not an abrupt process. Before the lean blowoff, the flame tends to oscillate between extinction and reignition phases. In 1950s, Nicholson and Field [9] reported that the flame detached and

reattached to the flame holder before lean blowoff. These temporary extinction-reignition events can thus be considered as precursors to the imminent total flame loss in the combustor. Several related studies had characterized the dynamic blowoff process of methane fueled flames stabilized by pilot [10], bluff body [11], and swirl [12,13].

From a view of stirred reactor, extinction occurs where the reactor residence time is too short relative to the chemical time. For a given rate of heat loss, flamelet is extinguished if the flame strain rate exceeds a certain value, again a function of reaction heat release rate. A flame subjected to aerodynamic influences is called a stretched flame [14]. In general, a flame front, which is propagating into the non-uniform flow, is subjected to strain and curvature effects. These effects change the flame area, and the flame stretch, κ, is defined as the fractional rate of change of a flame surface element [15].

$$\kappa = \frac{1}{A}\frac{dA}{dt} \quad (4)$$

$$\kappa = \nabla_t \cdot \vec{u} + S_d(\nabla \cdot \vec{n}) = \kappa_s + \kappa_c \quad (5)$$

where A is the surface element; $\vec{u}$ is the flow velocity; S_d is the displacement speed of flame front, and κ_s and κ_c indicate strain effect and curvature effect, respectively.

Flame stretch would modify flame properties, such as flame speed and flame temperature. Diffusive properties of mixtures are very important to stretch flames. For flames with equal diffusivities, the influence is negligible. For non-equil-diffusive flames, however, stretch effects strongly affect the flames. In general, there are two diffusion effects for non-equil-diffusive mixtures.

The first effect is Lewis number effect, which is the ratio of thermal diffusivity and mass diffusivity of the deficient reactant, which is fuel for lean premixed combustions.

For non-equil-diffusive flames, such as most syngas flames, stretched flames show that the flame response exhibits opposite behavior when the stretch changes from positive to negative, and when the mixture's effective Lewis number is greater or less than unity[16].

The second effect is preferential diffusion effect, which is the ratio of mass diffusivities of deficient reactant and excess reactant. If the lean reactant, such as hydrogen, is also the more diffusive one, the reactant concentration in the reaction zone will become closer to stoichiometric. If the stretch rate is constant, this leads to a higher flame temperature. [16]

If the stretch rate is greater than some critical value, the flame will be extinguished because the flame temperature is too low or residence time is too short under such a high stretch rates. This critical stretch rate is defined as the extinction strain rate.

For a turbulent flame, such as swirling flame, the stretch rate along the flame front is not a constant. At one specific point, if local stretch rate is higher than some critical stretch rate, local extinction occurs and a flame hole is generated.

1.3 Literature Review

1.3.1 Lean Blowoff Correlation

In practical combustors, stabilization is often accomplished by recirculation [17]. For example, recirculation can be generated by the wake behind a bluff body, bubble vortex breakdown in swirling flow, and separation due to sudden expansion. The flame is stabilized in a low velocity, high shear region where heat and radicals are recirculated back, continuously igniting the fuel/air mixtures.

Developing physics-based correlations of blowout behavior is complicated by the lack of understanding of the flame characteristics at the stabilization point. In addition,

the unsteady three dimensional flow structures in most of combustors make modeling work more difficult. Although different flow structure and physical theories have been used to model the blowoff limits for the recirculation stabilized flames, these mechanisms ***mathematically*** lead to the basic approaches described in the prior section, well stirred reactor model and flame propagation model, see Figure 2. These two mechanisms also represent a disagreement on whether premixed flames in high turbulent intensity gas turbine environments have flamelet, "thickened" flamelet, or well stirred reactor (WSR) – like properties.

Extensive experimental work was initiated in the 1950's, such as those of Zukoski and Marble [18], Spalding [19], or Longwell [20]. Zukoski and Marble [18] assumed that, for a bluff body stabilized flame, the free-stream is in contact with the recirculation zone for a time L/U_{ref}, and this flow contact time scale equals to the ignition time, τ_{ig}, at blowoff. They expressed this blowoff criterion as:

$$\frac{L/U_{ref}}{\tau_{ig}} = 1 \quad (6)$$

where L, U_{ref}, and τ_{ig} represent reference length, reference flow speed, and ignition time scale. If we define the flow or residence time (τ_{res}) as L/U_{ref}, then the equation above can be write as:

$$1 = \frac{L/U_{ref}}{\tau_{ig}} = \frac{\tau_{res}}{\tau_{chem}} = Da_{zu} \quad (7)$$

Thus Zukoski and Marble's blowoff theory predicts blowoff at Da_{zu}=1.

Spalding [19] assumed that the recirculation region as one of steady-state heat transfer with chemical reaction, which heats the free steam through a mixing layer. Spalding started from the energy equation. Two nondimensional parameters in the

solution of temperature were found important. The blowoff condition is that these two parameters do not equal. These two parameters are expressed as:

$$\frac{U_{ref}L}{\alpha} \propto \frac{ZP^{n-1}L^2}{\alpha} \quad (8)$$

where Z, α, and P denote pre-exponential factor in Arrhenius form, thermal diffusivity, and pressure. Laminar flame speed S_L can be expressed and scaled as:

$$S_L \propto (\alpha RR)^{1/2} \propto (\alpha ZP^{n-1})^{1/2} \quad (9)$$

where RR denotes the globe reaction rate. So these two key parameters can be modified as:

$$\frac{U_{ref}L}{\alpha} \propto \frac{S_L^2L^2}{\alpha^2} \Rightarrow \frac{U_{ref}}{L} \propto \frac{1}{\alpha/S_L^2} \quad (10)$$

If chemical time is estimated as:

$$\tau_{chem} = \alpha/S_L^2 \quad (11)$$

then the relation between these two parameters is

$$\frac{U_{ref}}{L} \propto \frac{1}{\tau_{chem}} \Rightarrow 1 \propto \frac{\tau_{res}}{\tau_{chem}} \Rightarrow 1 \propto Da_{sp} \quad (12)$$

which again leads to a Damköhler number criterion.

Longwell *et al.* [20] considered the wake region after the bluff body as a WSR. Longwell *et al.* started from the mass flow rate entering the WSR, and derived the same mathematical equation as the one derived by Zukoski and Marble [18].

Rizk and Lefebvre [21] reviewed the work of Longwell, Zukoski and Marble, and Herbert [18-8,22], and found all the models yield the same general conclusions in regard to the influences of pressure, temperature, geometry and flow speed. They expressed the lean blowoff limit as:

$$C = \frac{U_{ref}}{L}\frac{\alpha}{S_L^2} \quad (13)$$

where C is a shape factor, whose value is a constant for one specific flame holder. This equation finally leads to a ratio of residence time and chemical time,

$$C = \frac{\tau_{chem}}{\tau_{res}} = \frac{1}{Da} \quad (14)$$

Williams [23] summarized these blowoff correlations for recirculation flow, and expanded the critical blowoff equation as:

$$U_{ref} = L\rho S_L^2 (2\frac{C_p}{\lambda}) \quad (15)$$

where C_P, λ, and ρ denote constant-pressure specific heat, thermal conductivity, and density, respectively. This equation can be rewritten as:

$$\frac{U_{ref}}{L} = 2\frac{S_L^2}{\lambda/\rho C_p} = 2\frac{S_L^2}{\alpha} = \frac{2}{\tau_{chem}} \Rightarrow 2 = \frac{\tau_{res}}{\tau_{chem}} = Da_{Wi} \quad (16)$$

Another standard blowoff correlation is the Peclet number correlation [24]. Putnam and Jensen proposed this kind of correlations for bluff body stabilized flame. Peclet numbers were defined based upon flame and flow velocity:

$$Pe_u = U_{ref}L/\alpha \text{ and } Pe_{SL} = S_L L/\alpha \quad (17)$$

Putnam and Jensen found Pe_U is correlated with Pe_{SL} at lean blowoff:

$$Pe_u = \frac{1}{C}Pe_{SL}^2 \Rightarrow U_{ref}L/\alpha = \frac{1}{C}S_L^2 L^2/\alpha^2 \quad (18)$$

which can be simplified as:

$$C = \frac{L/U_{ref}}{\alpha/S_L^2} = \frac{\tau_{res}}{\tau_{chem}} = Da_{pu} \quad (19)$$

So the Peclet number correlation also represents a *Da* correlation.

Fluid mechanics definitely has significant effects on the blowoff phenomenon. Turbulence and Reynolds number (*Re*) are believed to be important factors, and were included in some studies.

Radhakrishnan *et al.* [25] proposed a correlation for blowoff velocity. A specific turbulent structure is assumed to exist in the combustion zone, combined with the coherent structures, and a model for the combustion process was developed based on this assumption. Finally, a blowoff criterion equation was given as:

$$U_{ref} = R^2 S_L^2 L / \nu \quad (20)$$

where ν represent the kinematic viscosity, and *R* is a dimensionless constant, whose value depends on the turbulent level and the geometry. This equation can be rewritten as:

$$1 = \frac{R^2 \dfrac{L}{U_0}}{\dfrac{\nu}{S_L^2}} \quad (21)$$

The Prandtl number, *Pr*, is defined as,

$$\mathrm{Pr} = \frac{\nu}{\alpha} \quad (22)$$

then

$$1/R^2 = \frac{L/U_0}{\alpha/S_L^2} = \frac{\tau_{res}}{\tau_{chem}} \frac{1}{\mathrm{Pr}} = \frac{Da_{Ra}}{\mathrm{Pr}} \quad (23)$$

which also leads to a Damköhler number model.

Plee and Mellor [26] also studied flame stabilization in terms of characteristic times. They considered lean blowoff in bluff body stabilized flames as a competition between characteristic fluid time and chemical times, (τ_{res}/τ_{chem}), in the shear layer region between the recirculation zone and the free stream. Flame stabilization of three different bluff body flame holders were tested by this model. For premixed gaseous flames at low and high *Re*, the authors confirmed that their model is essentially equivalent to the Peclet number correlations, proposed by Putnam and Jensen [24], and blowoff theory from Zukoski and Marble [18], respectively.

Loblich [27] combined the lean blowoff correlations found by Zukoski and Marble and by Putnam and Jensen. Loblich proposed a physical model by using the transport process of mass and heat transfer. This model emphasized the importance of Reynolds number (*Re*), and pointed out that the model from Zukoski and Marble [18] is valid for Re<10,000. Loblich derived a dimensionless number, stability number (N_X), which is defined as:

$$N_X = U_{ref}\nu / LS_L^2 \quad (24)$$

The stability number can be express as:

$$N_X = \Pr \frac{\alpha / S_L^2}{L / U_{ref}} = \Pr \frac{\tau_{chem}}{\tau_{res}} = \frac{\Pr}{Da_{Lo}} \quad (25)$$

The work of Hoffman *et al.* [28] is of special interest, as it focused on swirling flows. They found good success with the Peclet number correlation of equation (19) to capture the dependence of blowoff limits in swirling, premixed flames upon combustor diameter, flow velocity, and swirl number. Strakey *et al*. [29] studied the blowoff limits in a premixed, swirl stabilized combustor at pressure up to 8 atmospheres and 580 K of

reactants temperature. The blowoff limits were successfully correlated by a well stirred reactor approach.

Based on a large number of lean blowoff data acquired from aircraft combustion chambers, Lefebvre [30] proposed an equation for lean blowoff. He suggested that blowoff is determined by a nondimensional variable *K*:

$$K = \frac{m_A}{V_c P^{1.25} \exp(T/150)} \quad (26)$$

where m_A, Vc, P, and T indicate mass flow rate, characteristic volume of recirculation zone, pressure and temperature. If these parameters are scaled as:

$$m_A = \rho U A \propto P U_0 L^2 \quad (27)$$

$$V_c \propto L^3 \quad (28)$$

$$\exp(T/150) \propto RR \propto (\alpha RR/\alpha) \propto (S_L^2/\alpha) \quad (29)$$

Then equation (30)is given by substituting (27)-(29)into(26):

$$K = \frac{P U_0 L^2}{L^3 P^{1.25} \frac{S_L^2}{\alpha}} = P^{0.25} \frac{U_0 \alpha}{L S_L^2} = P^{0.25} \left(\frac{L/U_0}{\alpha / S_L^2} \right)^{-1} = P^{0.25} \left(\frac{\tau_{res}}{\tau_{chem}} \right)^{-1} = P^{0.25} Da_{Le}^{-1} \quad (30)$$

It is clear that the essential part of this blowoff variable *K* is still a Damköhler number.

As noted by Glassman [17], all these theories and mechanisms lead to essentially the same mathematical form of correlation. These correlations generally involve relating the blowoff limits to a ratio of a residence time (or a flow time) and chemical kinetic time, $\tau_{res} / \tau_{chem,}$ which is Damköhler number. It is possible that the recirculation regions that stabilize many high intensity flames, which may have flamelet properties at most other

points along the flame, have distributed reactor-like properties; hence, the success in WSR models in correlating blowout behavior.

Although a general mathematical equation, $Da=C$, is derived for WSR blowoff mechanism, due to different physical models used, the ways to calculate residence time and chemical time are different. The residence time is generally scaled as L/U_{ref}, where L and U_{ref} denote a characteristic length scale (e.g., a recirculation zone length) and velocity scale, respectively. The easiest way to scale L is taking the diameter of the flame holder or the combustor. For a WSR model, the size of the virtual reactor is more important than the actual combustor size, so it is more reasonable to scale the characteristic length scale with the length of the recirculation zone, which is used for most of the WSR model. This recirculation length is generally a function of combustor size, Reynolds number, and swirl number, $L_{re}=f(L_{combustor}, Re, S)$. Due to the turbulent features of the flow, integral length scale and Taylor macro scale are also used to scale the characteristic length scale in some models [25].

Note that U_{ref} need not directly scale with approach flow velocity, U_u, due to the acceleration of the burned gas [23]. A burned gas velocity scale is given by $U_b=(T_b/T_u)U_u$, then $U_{ref}=f(U_u, T_b/T_u)$. The azimuthal velocity component, U_θ, was used by Hoffman as the reference velocity, $U_{ref}=U_\theta$ in blowoff correlations [28].

The characteristic chemical time is scaled by equation (11) for most of the WSR model, and sometimes with the involvement of Pr. Alternative methods of estimating a global chemical time, such as ignition delay time and blowoff time of a WSR, are also possible, but generally lead to results qualitatively similar to equation (11) [31].

Significantly less attention has been given to correlating premixed flame blowout limits assuming flamelet-like combustion properties, where the stabilization mechanism is related to front propagation, rather than reactor extinction. In this case, a flame would blow off when the turbulent flame speed is everywhere less than the flow velocity, $S_T<U_{ref}$, where S_T denotes the turbulent flame speed. If this propagation mechanism is controlling, then blowoff limits should scale with the parameter:

$$L_2 = \frac{S_T}{U_{ref}} \qquad (31)$$

This blowout model was proposed by Lewis and Von Elbe [32], who explained blowout as a function of velocity gradients in the boundary and flame speed. This model was expanded by Wohl [33], who described that critical condition of lean blowoff as the velocity gradient at the wall equals to the ratio of flame speed to the blowoff distance.

$$g_{crit} \cong \frac{S_L}{X_{bl}} \quad (32)$$

where g_{crit} indicates the critical speed gradient, and X_{bl} represents blowoff distance, whose value highly depends on geometry and pressure. It should be pointed out that, although a flame speed the key parameter of their correlations, the velocity gradient or stretch rate, $\frac{m/s}{m} = 1/s$, is the controlling parameter.

Krevelen and Chermin [34] followed the basic idea of Lewis and Von Elbe, and used a modified velocity gradient to correlate lean blowoff in a Bunsen burner. Different binary fuels, hydrogen and hydrocarbon, were tested and proved that the critical condition of lean blowoff is a function of velocity gradient.

This model also has been used to correlate the lean blowoff limits of a flame stabilized by sudden expansion [35]. The recirculation zone generated by the sudden expansion exchanges heat and radicals with free stream in the shear layers. Driscoll and Rasmussen showed a reasonable correlation based the concept that the propagation speed of the flame in the shear layer is matched to the velocity of the local flow.

Turbulent flame speed, S_T, may be more reasonable than laminar flame speed, S_L, in the blowoff correlation. However, modeling and measuring the turbulent flame speed is another complex problem as well as the blowoff correlation. In particular, evaluating the turbulent flame speed introduces additional complications for mixtures with widely varying compositions. Correlations of the turbulent flame speed of the form: $S_T = S_L : f(u', \text{geometry})$, where u' denotes turbulent intensity, have been used successfully in many prior studies across limited fuel ranges. However, recent studies across broader ranges of fuels clearly indicate the limitations of the above correlation; other fuel properties are also very important. For example, **Figure 3** is reproduced from Kido *et al.*[36] and plots the dependence of the turbulent flame speed for a variety of H_2, CH_4, and C_3H_8 mixtures. These mixtures were carefully chosen to have identical laminar flame speeds, as indicated by the S_T curves converging at $u'=0$. Interestingly, however, the curves widely diverge as u' increases from zero. In particular, note the substantially higher turbulent flame speed of the H07-15N mixture, which is a hydrogen blend, relative to the methane fuels (MO7-15N, M09-15N, MO98-15N).

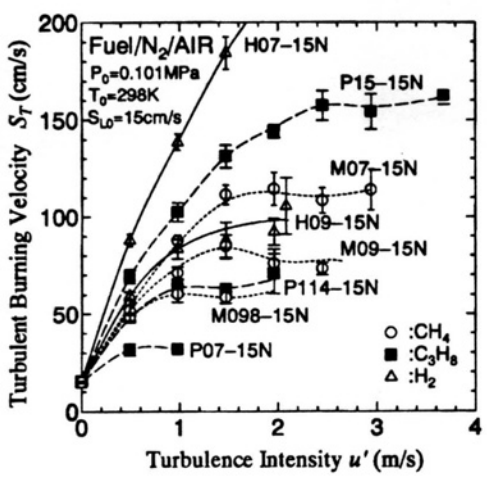

Mixture	Molar Fraction Fuel	O_2	N_2	ϕ	S_{L0} (cm/s)
H07-15N	H_2	0.71	7.14	0.7	15.26
H09-15N	H_2	0.56	6.94	0.9	15.88
M07-15N	CH_4	2.86	11.17	0.7	15.10
M09-15N	CH_4	2.22	10.82	0.9	14.91
M098-15N	CH_4	2.04	10.51	0.98	14.84
P07-15N	C_3H_8	7.14	29.05	0.7	14.94
P114-15N	C_3H_8	4.39	23.82	1.14	15.34
P15-15N	C_3H_8	3.33	13.70	1.5	14.99

Figure 3: Dependence of turbulent flame speed upon turbulence intensity for several fuel blends with the same laminar flame speed (reproduced from Kido *et al.* [36]).

This substantial increase in the turbulent flame speed of the hydrogen mixture is likely due to thermal-diffusive instabilities of lean hydrogen mixtures; that is, these mixtures are unstable even in the absence of turbulence, resulting in the spontaneous wrinkling of the premixed flame[37]. This conclusion is supported by related studies that compare the turbulent flame speeds of thermo-diffusively stable/unstable mixtures with the same laminar flame speeds (e.g., by comparing rich and lean methane mixtures) that also show that the unstable mixtures have higher flame speeds[38].

These instabilities can be related to the stretch sensitivity of the flame speed. Recall that the flame speed of a stretched flame is given as [38]:

$$\frac{S_L}{S_{L,0}} = 1 - MaKa \qquad (33)$$

where $S_{L,0}$, Ma, and Ka, denote the unstretched laminar flame speed, $Ma=L/\delta$ (Markstein number), and $Ka=\tau_{chem}/\tau_k$ (Karlovitz number), respectively. L, δ and τ_k denote Markstein length, flame thickness, and Kolmogorov time scale. Thermo-diffusively unstable flames have negative Markstein numbers, which cause bulges in the flame to grow. Ma has positive and negative values when $Le > 1$ and $Le < 1$, respectively.

It should be emphasized that Peclet number correlation proposed by Putnam and Jensen [24] is also based on the physical mechanism of a competition between flame speed and flow speed. However, the final mathematic blowoff correlation leads to a Damköhler number. This also proves that Damköhler number model and flame propagation model are mathematically inter-correlated.

Most of the blowoff research work discussed above focused on correlating blowoff limits of a given fuel over varying geometry, pressure, or flow velocity. Some studies considered a range of fuels [28, 29], which are discussed below.

1.3.2 Effects of Fuel Compositions on Blowoff Limit

The effects of fuel composition of $CH_4/H_2/CO$ mixtures on blowoff limit have been extensively studied recently. For example, it is found that H_2 addition has significant effects and extends the blowoff limit of CH_4 or other hydrocarbon flames. Several studies have been initiated relatively recently to investigate the characteristics of premixed, hydrogen-enriched fuels [39,40,41].

Griebel *et al.* [42] studied blowoff limits in a premixed combustor for pressure up to 14 bars, flow speed up to 80 m/s, and preheat temperatures up to 773 K for H_2/CH_4 flames. The fuel composition varied in from 0 to 20% H_2 in volume. The results clearly show that addition of H_2 can significantly extend the lean blowoff limit. The lean blowoff fuel/air ratio is lowered approximately 10% for 20% H_2 addition. In addition, the extension of the lean blowoff limit linearly varies with the percentage of hydrogen. Griebel *et al.* [42] attributed a higher OH radial concentration as the reason, which leads to a higher global reaction rate and a higher flame speed.

In a series of papers [40,41,43], Schefer, Wicksall, and Agrawal measured the lean blowoff limits of H_2/CH_4 flames in a lean premixed swirl stabilized combustor with room temperature and pressure reactants. Instead of equivalence ratio, adiabatic flame temperature, whose value highly depends on the overall equivalence ratio, was used to represent the blowoff limit. A similar result, that the adiabatic flame temperature at blowoff is decreased by adding H_2 into methane, was found for mixtures with up to 40% H_2 by volume. The importance of the chain branching reaction, $H+O_2 \Leftrightarrow OH+O$, in hydrogen enriched hydrocarbon flames was emphasized with respect to extinction. Schefer *et al.* [43] suggested that higher OH radical concentration promotes the overall reaction rate, as well as to reduce CO emissions by completing CO oxidation to CO_2 via the OH radical.

Yoshimura *et al.* [44] measured the blowoff limit of methane with up to 50% H_2 addition by volume. The authors found that hydrogen addition not only extends the blowoff limits, but also improves the CO and NOx emission. Volumetric 50% H_2 addition into methane allows the combustor to operate 200K cooler before lean blowoff.

Although not explicitly mentioned by the authors, a linear correlation was found between percentage of hydrogen and adiabatic flame temperature at blowoff.

The research works discussed above considered a higher radical, especially OH, concentration due to H_2 addition as the key factor. The early breakdown of H_2 has been suggested as a key mechanism for enhanced CO and CH_4 mixtures [45].

Several recent studies have focused on H_2 enriched flames [40, 41] and shown that small addition of H_2 enhances the mixture's resistance to extinction. Compared with flame temperature, flammability limit, and flame speed, extinction strain rate is suggested to have a major effect on lean blowoff [46]. For example, fundamental studies in opposed flow burner geometries show that the extinction strain rate of methane flames is doubled with the addition of 10% H_2 [47,48].

1.3.3 Flame Dynamics near Lean Blowoff

Understanding the processes of how the flame approaches blowoff is the key to give a rational blowoff correlation. It has been proved that lean blowoff is not an abrupt process. Before the lean blowoff, the flame tends to oscillate between extinction and reignition phases.

Nicholson and Field [49] observed large scale pulsations in a bluff body flame as it was approaching lean blowoff. At the same time, it was also reported that the main flame detached and reattached to the flame holder repeatedly before extinguishing completely

Hertzberg *et al.* [50] also observed this kind of oscillation, and claimed that blowout was a result of increased ignition times, longer re-circulation zones and local extinction resulting from high instantaneous strain rates.

Hedman *et al.* [.51] investigated blowoff in a swirl stabilized combustor using OH PLIF. They observed intense flame oscillations and temporary loss of flame near the lean blowoff. CFD studies by Norton [52] in micro-burners also observe periodic oscillations near extinction. High heat loss and the presence of large transverse and axial velocity gradients were believed to be the reasons.

This dynamic blowoff process has been also been found in several flame types at Georgia Tech: pilot flames, bluff body flames, and swirling flame [10, 11, 12, 13]. For swirling flames, Muruganadam [53] proposed that the extinction/reignition oscillation is driven by the changing of vortex breakdown modes. He also observed that the number of extinction/reignition events per unit time monotonically grows as blowoff is approached. These observations have formed the basis of an active control system that detects blowoff precursors and applies closed loop active control to prevent its occurrence [53].

1.3.4 Flame Stretch and Extinction Stretch Rate

For non-equil-diffusive stretched flames, there are two diffusive effects, Lewis number effect and preferential diffusion effect [16]. Both of these two effects are very important for H_2/CO/CH_4 mixtures, since Lewis number and preferential diffusion ratio vary in a significantly wide range, which will be detailed in the next chapter.

Extensive literatures focused on laminar flame speed or flame temperatures under stretch. Counterflows, stagnation wall, and spherical propagating flame models have been used in most of the studies [54, 55, 56, 57]. It is known that, for non-equil-diffusive flames, such as most syngas flames, stretched flames show that the flame response

exhibits opposite behavior when the stretch changes from positive to negative, and when the mixture's effective Lewis number is greater or less than unity.

In a symmetric steady state counterflows flames, Law *et al.* measured the positive extinction strain rate for methane and propane flames at 100 Kpa and 300 K. A similar setup was also used in simulation work by Chung [58], Smooke [59], Stahl and Warnatz [60], and Kee *et al.*[61] and the results are similar.

Compared with positive stretch rates, significantly less research work was done on negative extinction stretch rates. Echekki and Mungal [62] and Wagner and Ferguson [63] measured the negative stretch rate due to curvature in the absence of flow strain rate, in a slot burner and a cylindrical burner, respectively. The extinction phenomenon did not happen with negative stretch rates up to 6000 1/s. Bradley simulated the spherical flames with a negative stretch rate, and extinction did not happen at negative stretch rate of 500 1/s for a methane flame at equivalence ratio of 0.55.

Negative stretch rate due to strain in the absence of curvature was measured indirectly. In a counterflows setup, a series of flame speeds under positive stretch rates was measured, and then the line between stretch rate and flame speed was extrapolated to the negative stretch side, finding the zero flame speed point, which is defined as the negative extinction strain rate [56]. The negative extinction stretch rates determined in such a way shows a quenching might arise in converging flow. However, the author is not aware of any experimental work reproducing these negative extinction stretch rates.

Several recent studies have focused on H_2 enriched flames [40, 41] and shown that a small addition of H_2 enhances the mixture's resistance to stretch extinction. For example,

fundamental studies in opposed flow burner geometries show that the extinction strain rate of methane flames is doubled with the addition of 10% H_2.[48]

For turbulent flames, the significance of aerodynamic straining of the flame sheet in the shear layer near the attachment point was apparently first discussed by Karlovitz *et al.* [64]. They noted that holes appeared in the side of the flame as flow velocity increased, apparently due to local extinction. Similar observations of such holes in flames near blowoff have been reported by Nair and Lieuwen [65] and Khosla and Smith [66].

There is an extensive literature available that has quantified flame strain statistics for turbulent flames, e.g., see Im and Chen [67,68] or Driscoll [69,70]. However, relatively few studies have focused on strain rate characterization in the vicinity of the attachment point of the flame.

1.4 Overview of Present Work

The overall objective of this research is to improve understanding of lean blowoff in low emissions, fuel flexible gas turbines, and also to improve the development of modeling and predicting tools needed to design fuel flexible combustion systems. It is essential to first understand lean blowoff of a simplified gas turbine combustor, swirl-stabilized premix flame system, and to develop the blowoff correlation and subsequent data analysis that would later be progressively applied to more complex fuel flexible gas turbine combustors. Since H_2, CO, and CH_4 are the main fuels of syngas, this research work only focus on the mixtures of these three fuels.

The outline of this thesis is as follows. Chapter 2 details the experimental setups. Chapter 3 describes the properties of syngas mixtures, and the approaches used to generate these fuels or flames parameters. The main results of this thesis are divided

between chapter 4－6, which consist of three efforts which delve into flame stabilization with increasing levels of quantitatively details. First, chapter 4, lean blowoff limits of H_2/CO/CH_4 mixtures were measured under different approach flow speeds, reactant temperatures, and combustion pressures. Correlations based upon both flow and mixture properties were then developed. Second, chapter 5, the blowoff phenomenology was systematically characterized as a function of the fuel compositions. The dynamic blowoff process was studied by chemiluminescence measurements, high speed imaging, and flow field measurements. Third, chapter 6 presents quantitative studies of the flow field in the vicinity of the attachment point of near blowoff flames. Finally, Chapter 7 presents the conclusions of this research and recommendations for future work.

CHAPTER 2

EXPERIMENTAL FACILITY, INSTRUMENTATION, AND DIAGNOSTICS

These experimental investigations were performed in the gas turbine simulators at Georgia Institute of Technology. Two combustors were used for this research work

2.1 High Pressure Gas Turbine Simulator

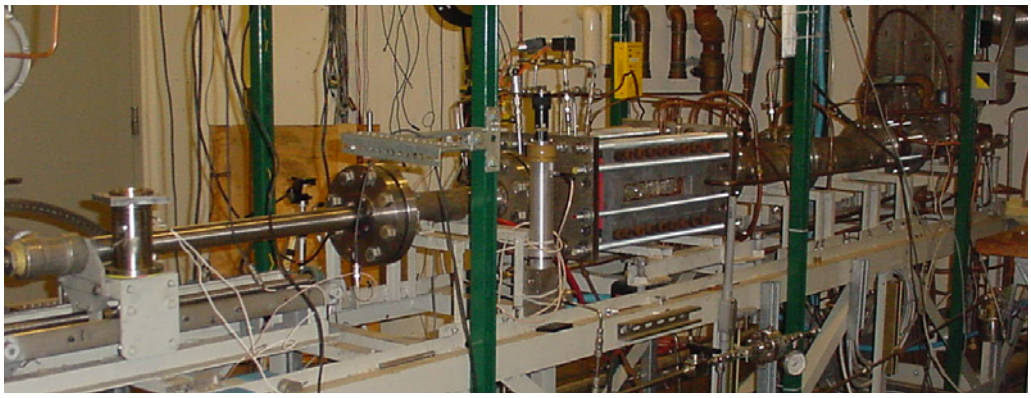

Figure 4: Photograph of lean, premixed combustor facility

The measurements for syngas blowoff limits were obtained in a lean, premixed gas turbine combustor simulator, shown in **Figure 4,** which has also been previously described in Ref. [71]. The facility consists of inlet/premixer, combustor, and exhaust sections. High-pressure natural gas and air are supplied from building facilities. The air can be preheated up to 700 K. The hydrogen and carbon monoxide are supplied from bottles. The air and fuel flow rates are measured with a critical orifice and mass flow

controllers (MFC's), respectively. Both the orifice and MFC's were calibrated using the specific gas with which they were to meter. This is necessary for H_2 in particular, as manufacturer supplied corrections that relate the flow of some other gas to the H_2 flow rate were found to be very inaccurate. The resultant uncertainty in the flow rate measurements is 2% of full scale. In order to ensure that acoustic oscillations did not affect the fuel/air mixing processes, the fuel and air are mixed upstream of a second choke point. Thus, the equivalence ratio of the reactive mixture entering the flame is constant. The temperature of the reactants was measured with a thermocouple located just upstream of the swirler.

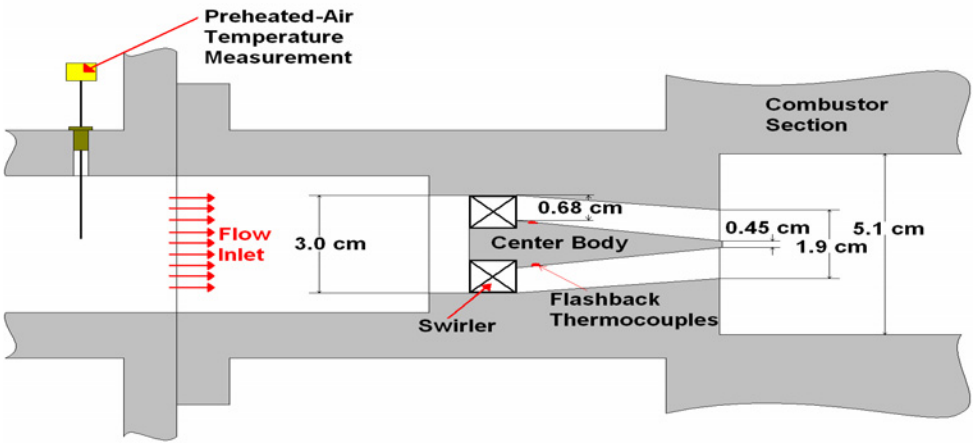

Figure 5: Cross section of premixer assembly

The fuel-air mixture entered the circular 4.75 cm diameter, 60 cm long inlet section and passed through a swirler prior to entering the combustor, see **Figure 5**. The premixer outer body slightly constricts along the axial flow direction. However, the overall flow area remains constant at 10.8 cm^2, as the center body diameter also decreases

in the axial flow direction. These tests were performed with a single 12 vane, 35^{o} swirler. Moreover, a thermocouple is imbedded in the centerbody for flashback detection.

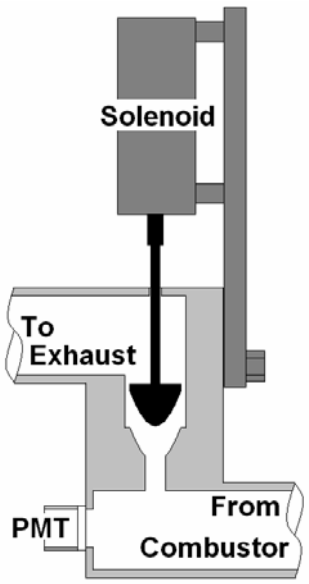

Figure 6: Back-pressure controller

The premixer terminates into the 5x5 cm square combustor. The square part of the combustor is 51 cm long and optically accessible. It then transitions into a circular 7.6 cm diameter, 195 cm long exhaust section. The exhaust sections are water cooled. The flow leaves the setup through an exhaust nozzle with an adjustable bypass valve. This adjustable bypass valve is controlled by LabVIEW in order to maintain the combustor pressure at some prescribed value.

In order to ensure that the pressure in the combustor was held at a (approximately) constant pressure, a back-pressure controller was used. This controller used a pressure transducer located just upstream of the swirler and center body and proportions a plunger valve in the exhaust section to maintain desired combustion pressure. This plunger was

controlled by a computer through LabVIEW. Figure 6 is a cross-sectional view of the exhaust and shows how the plunger valve controls the back pressure of the combustor.

2.2 Optically Accessible Combustor

In the study of near blowoff dynamics, we duplicated an experimental rig developed at Sandia National Laboratories [72] to capture chemiluminescence and visualize the flame front and flow field. This was done in order to have a similar test facility to facilitate comparisons of data and simulations. This gas turbine simulator is an atmospheric pressure, premixed, swirling stabilized dump combustor. The combustor is shown in **Figure 7**.

The facility consists of a swirler/nozzle, combustor, and exhaust sections. Premixed gas, consisting of H_2/CH_4 mixtures and air flows through a swirler housed swirler/nozzle section. The nozzle is an annular tube with inner diameter of 28mm. The center body has an outer diameter of 19 mm. The overall flow area remains constant at 3.0 cm^2 inside the nozzle. Tests were performed with a six-vane, 45^o swirler, which is located in the annulus between the centerbody and nozzle wall, see **Figure 7**. The theoretical swirl number, which is 0.85, is calculated by [73],

$$S = \frac{2}{3}\left[\frac{1-(d_h/d)^3}{1-(d_h/d)^2}\right]\tan\theta \quad (34)$$

where d_h and d are the diameters of centerbody and swirler, respectively, and θ is the swirler vane angle. The fuel is injected 150 cm upstream of the combustor to achieve a premixed condition. The combustor consists of a 305 mm (12 inches) long quartz tube, which permits the detection of ultraviolet (UV) radiation and imaging. The quartz tube has an inner diameter of 115 mm and rests in a circular groove in a base plate. An adapter slides in four standing bars, sitting on the top of the quartz tube, and the exhaust nozzle is connected to the adapter. In chapter 5, the exhaust nozzle has a 127mm with the area ratio 0.44, and a chimney section which is 102mm long with inner diameter of 51mm. In chapter 6, the exhaust nozzle has a 152 mm with the area ratio 0.44.

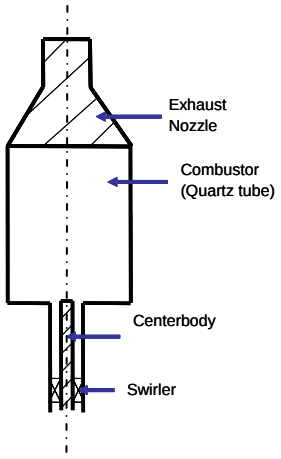

Figure 7: Schematic of the combustor facility

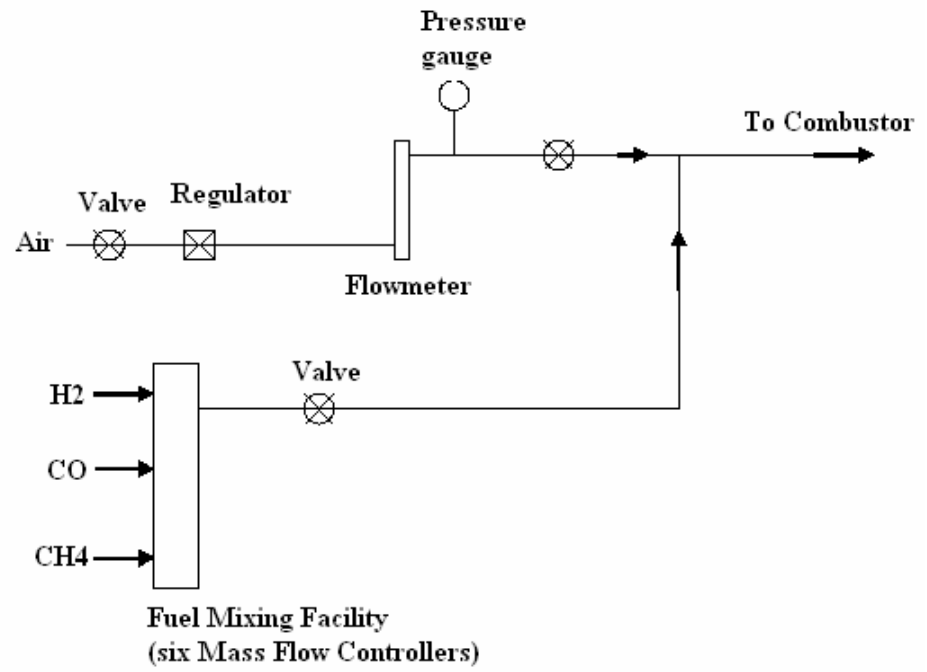

Figure 8: Schematic diagram of the flow control system

Figure 8 shows the schematic diagram of the flow control system. High-pressure natural gas and air are supplied from building facilities. The hydrogen is supplied from bottles. The air and fuel flow rates are measured with a flowmeter and mass flow controllers (MFC's), respectively. The same fuel mixing facility in the previous section was used to generate the syngas mixtures (H_2/CO/CH_4). Both the flowmeter and MFC's were calibrated using the specific gas with which they were to meter. The maximum resultant uncertainty in the flow rate measurements is 5% of full scale, and in blowoff equivalence ratios is 0.01-0.02 for most of the cases. The largest uncertainty in ϕ of 0.03 occurs with pure CH_4. The air is choked before the mixing section, and the premixed air/fuel is choked again inside the inlet tube of the combustor (not shown) upstream of

the swirler to minimize the impact of perturbations in the combustor influencing the fuel/air mixing process.

2.3 High Speed Visualizations and OH Chemiluminescence

High speed visualizations of the flame were obtained with an Ultracam3, Gen III intensified camera at 1000 frames/sec and 512 x 512 resolution. The photocathode is sensitive to light in the 400-900 nm spectral region and is, thus, unfortunately insensitive to the UV light that constitutes the primary chemiluminescence emission for high H_2 flames. As such, this variation of camera sensitivity should be kept in mind when comparing the images with varying H_2 levels in the images below.

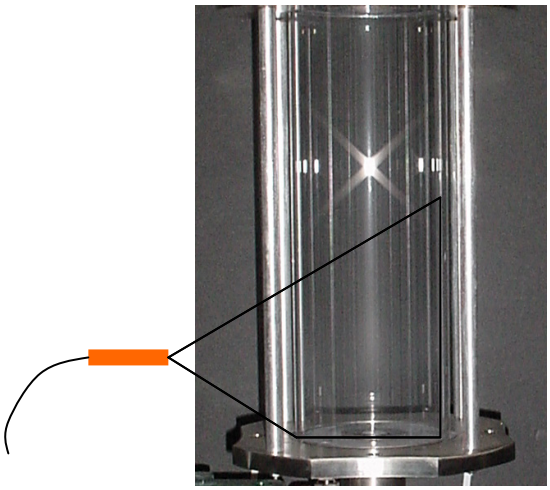

Figure 9: Location of the optical probe

In addition, UV radiation from the high H_2 flames was monitored with an optical fiber bundle (NA=0.44), with the head located 46 mm above the dump plate of the combustor and 171 mm radially from the combustor centerline, see **Figure 9.** This

volume was placed such that light is collected from the low one third of the combustor, in order to image the IRZ (inner recirculation zone). The light passes through an interference filter centered at 308 nm and with a full-width-half-maximum (FWHM) of 10 nm, which corresponds to the primary spectral region of OH* emission. This radiation was detected by a miniature, metal package PMT (Hamamatsu H5784-04). This PMT has a built-in amplifier (bandwidth of 20 kHz) to convert the current to voltage and operates from a 12 VDC source.

The signal output from the sensors was low pass filtered by a Krohn-Hite Model 3362 digital Butterworth filters and then fed into a National Instruments A/D board. The sampling frequency was 2 kHz. The low pass filter frequency (for anti-aliasing) was set at half the sampling frequency, 1 kHz.

2.4 PIV System

The velocity field in the combustor was measured using Particle Image Velocimetry (PIV) as explained by Raffel *et al.* [74]. The system consists of a dual head Nd:YAG laser, a high resolution CCD camera, a mechanical shutter and a centralized timing generator orchestrating the activation of each component. In addition a cyclone seeder built in-house was used to supply anhydrous aluminum oxide (Al_2O_3) with an average particle size of 3μm.

Each laser head delivered a 120 mJ/pulse beam at a wavelength of 532 nm. The beams passed though sheet forming optics, consisting of a convex spherical (f = 1 m) and a convex cylindrical lens (f = 25.4 mm), resulting in a 500 μm thick light sheet at the center of the combustor. The CCD camera captured the images of the illuminated

particles at a resolution of 1600 x 1200 pixels in frame straddling mode. This allowed for the duration between the laser shots to be at the desired level of 10 μs. In addition the camera was also fitted with a 532 nm laser line filter with a FWHM of 3 nm to restrict any background noise.

The images were processed using the DaVis 7.0 software package, provided by LaVision Inc. This software uses an adaptive algorithm to obtain the velocity field. The grid size was 32 pixels x 32 pixels with a 50% overlap.

CHAPTER 3

PROPERTIES OF H_2/CO/CH_4 MIXTURES

This chapter describes the approaches used to generate fuel and flame parameters, and the properties of H_2/CO/CH_4 mixtures used in the following chapters. As discussed in the first chapter, H_2/CO mixtures are generated upon the gasification/partial oxidization of the fuels, such as coal. In addition, syngas fueled plants sometimes co-fire with a certain fraction of natural gas, which is mainly composed of CH_4. So properties of H_2/CO/CH_4 mixtures are studied in this chapter.

3.1 Analysis Approach

The mixture equivalence ratio is given by:

$$\phi = \frac{(Y_{Air}/Y_{Fuel})_{Stoic}}{Y_{Air}/Y_{Fuel}} \qquad (35)$$

where Y_i is the mass of the indicated specie.

Adiabatic flame temperatures were calculated for a given mixture using standard methods. Based on the assumption that the absolute enthalpy of the reactants at the initial state, say 300K and 1 atm, equals the absolute enthalpy of the products at the final state, which is the adiabatic flame temperature. Laminar flame speeds were calculated with the PREMIX application in CHEMKIN, using the GRI3.0 mechanism. While this mechanism was primarily optimized for methane/air mixtures, good comparisons

between its results and measurements have been obtained for a range of H_2/CO mixtures as well [75].

Chemical time associated with laminar flame propagation was estimated by:

$$\tau_{chem} = \frac{\alpha}{S_L^{\,2}} = \frac{\lambda}{\rho C_p}\frac{1}{S_L^{\,2}} \quad (36)$$

where α indicates thermal diffusivity. The thermal conductivity of the reactive mixture, λ, was determined using transport properties from TRAN in CHEMKIN and the equation [76]:

$$\lambda = \frac{1}{2}\left(\sum_{k=1}^{K} X_k \lambda_k + \frac{1}{\sum_{k=1}^{K} X_k / \lambda_k}\right) \quad (37)$$

Specific heat, C_p, is determined by a polynomial fits:

$$C_p = R(a_1 + a_2 T + a_3 T^2 + a_4 T^3 + a_5 T^4) \quad (38)$$

where the polynomial coefficients, a_i, are collected from TRAN in CHEMKIN.

Diffusivity coefficients of a given species, *k*, in the mixture, *m*, were determined from:

$$D_{km} = \frac{\sum_{j\neq k}^{K} X_j W_j}{\overline{W}\sum_{j\neq k}^{K} X_j / D_{jk}} \quad (39)$$

These diffusivity coefficients, combined with the mixture thermal conductivity were used to determine the Lewis number of the *k*-th specie:

$$Le_k = \frac{\lambda}{\rho C_P D_{km}} \qquad (40)$$

Since the above Lewis number is defined for a given species, not the mixture, a mixture averaged Lewis number was also determined using the relation:

$$Le_{mix} = \frac{\lambda}{\rho C_p \sum_{k=fuel} A_k D_{km}} \qquad (41)$$

where A_k is the percentage of heat release due to fuel k relative to that of the entire mixture. It should be emphasized that definition of the appropriate mixture averaged Lewis number is not trivial – analytical expressions derived using one-step kinetics and asympototics show that Le_{mix} is not only a function of the Lewis number of the respective species, but also Zeldovich number[77].

Blowoff residence time, $\tau_{blowoff}$, is calculated with the AURORA in CHEMKIN. Start with a large value, the residence time of a well stirred reactor is reduced until flame blows off. This critical value is the blowoff residence time, which can be used as an alternative chemical time scale.

3.2 Fuel and Flame Parameters

In order to obtain the basic understanding of the properties of $CO/H_2/CH_4$ mixtures, a number of results showing the interdependence of these quantities are included below.

Consider first the density of $CO/H_2/CH_4$. **Figure 10** illustrates the dependence of the fuel and fuel/air density at an equivalence ratio of 0.6 upon fuel composition. The fuel composition by volume is given by the location within the triangle, where the three vertices denote pure CO, H_2 or CH_4. For fuel density (left of **Figure 10**), high CO mixtures have the highest density, around 15 times that of high H_2 mixtures. This density variation simply represents the molecular weight of these fuels. However, for lean fuel/air mixtures, the density variation is far less than, (right of **Figure 10**), the density difference of above.

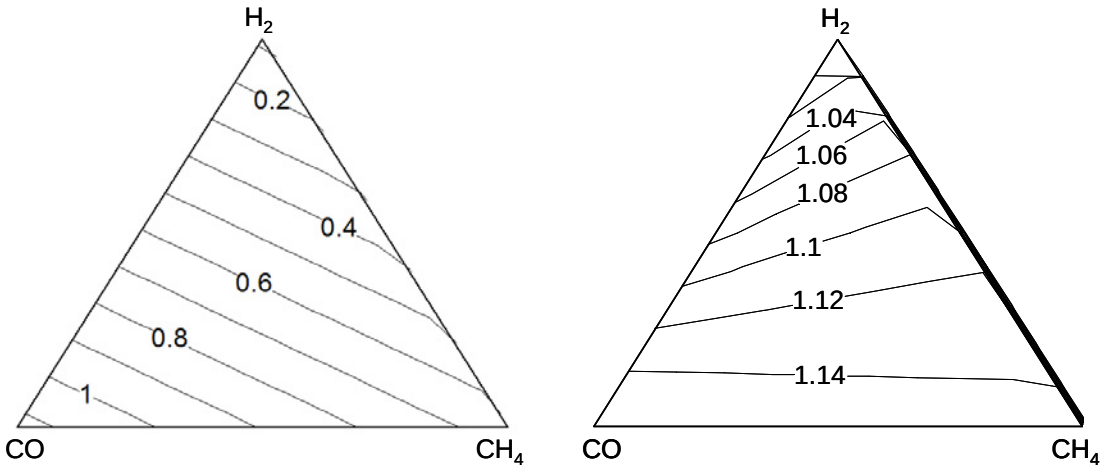

Figure 10 : Density (kg/m^3) of $H_2/CO/CH_4$ mixtures (left) and density (kg/m^3) of ($H_2/CO/CH_4$)/Air mixtures (right) at equivalence ratio of 0.6 with 300K and 1 atm

Figure 11 shows the dependence of the heating value upon fuel composition. For LHV per mole, methane has a higher heating value (>800 kJ/mole), while H_2 and CO mixtures have a much smaller heating value (<300 kJ/mole). However, since hydrogen has a small molecular weight, high hydrogen mixtures have the highest heating value

based on mass, while CO mixtures have the smallest values. So for a given power level, the volumetric or mass fuel flow varies by a factor of about 2.5 and 8, respectively.

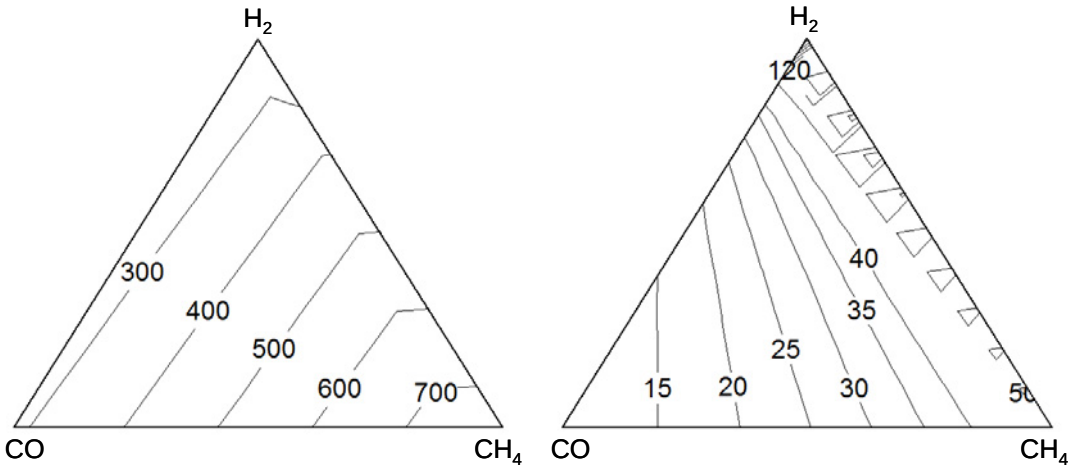

Figure 11: Dependence of lower heating value (kJ/mole) based on volume (left), and lower heating value (kJ/g) based on mass (right), upon fuel composition.

Next consider the flame speed, S_L. Figure 12 illustrates the dependence of the flame speed upon fuel composition at two fixed adiabatic flame temperatures, 1500 and 2000 K. At each point within the triangle, the mixture equivalence ratio is adjusted such that the mixture has the given flame temperature. As expected, the high H_2 mixtures have the highest flame speeds. Note also the slightly higher flame speeds of the high CH_4 mixtures relative to those of CO mixtures.

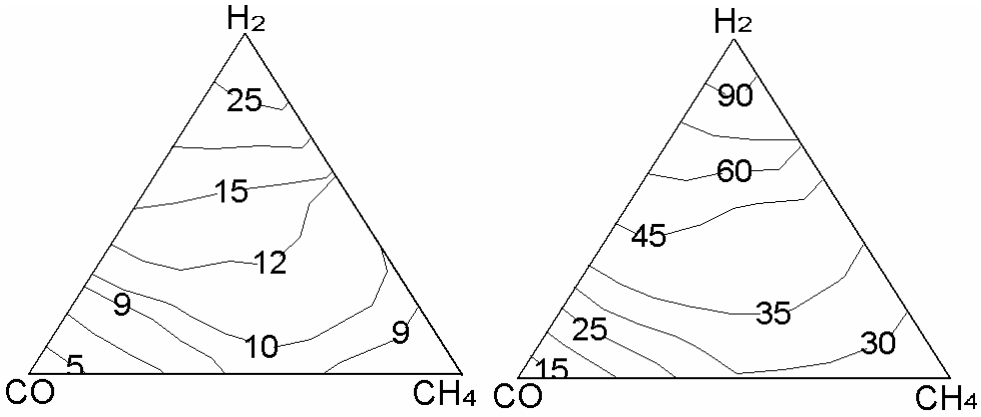

Figure 12: Dependence of flame speed (cm/s) upon fuel composition at fixed 1500 K (left) and 2000 K (right) adiabatic flame temperatures with 300K reactants temperature.

An alternative way to view these results is to plot adiabatic flame temperature at a fixed flame speed. This is done in Figure 13 for $S_{L,o}$=10 and 20 cm/s. Note the progression in flame temperatures from CO and H_2 mixtures being the highest and lowest, respectively.

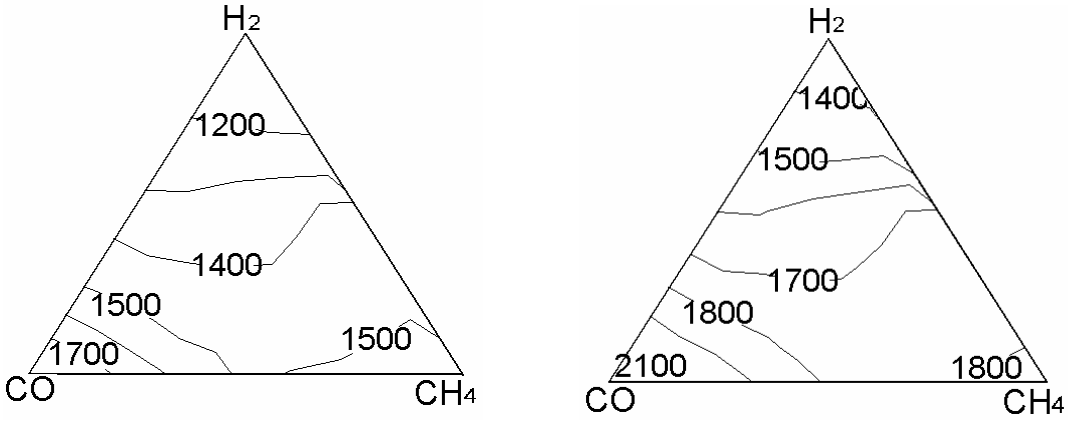

Figure 13: Dependence of adiabatic flame temperature (K) upon fuel composition at fixed laminar flame speed 10 cm/s (left) and 20 cm/s (right) with 300K reactants temperature.

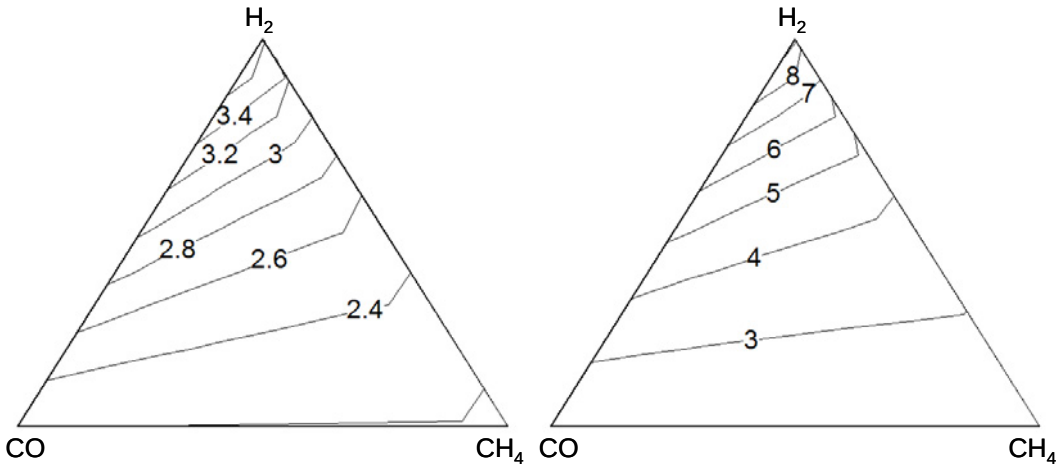

Figure 14: Left: dependence of thermal diffusivity (1.0E5*m^2/s) upon fuel composition at 300K; Right: dependence of mass diffusivity of fuel (1.0E5*m^2/s) upon fuel composition at 300K;

Figure 14 shows the dependence of thermal diffusivity and mass diffusivity of (H_2/CO/CH_4)/air mixtures upon fuel composition at an equivalence ratio of 0.6, 300K and 1 atm. Mass diffusivity of the deficient reactant here is defined as the diffusivity of fuel (H_2/CO/CH_4) in air. Note the high diffusive hydrogen mixtures in both plots, and that the variation in mass diffusivity is larger than thermal diffusivity.

Figure 15 plots the dependence of the mixture weighted Lewis number, Le_{mix}, see eqn (41), upon fuel composition at a fixed flame temperature of 2000 K(left) and fixed equivalence ratio of 0.6 (right). For all the mixtures at 2000K, as above, note that the mixture equivalence ratio is varying – it is the flame temperature that stays fixed. The figure shows that this Lewis number ranges from a low of 0.4 in the high H_2 mixtures to a high of slightly above one in the high CO mixtures. For all the mixtures at equivalence

ratio of 0.6, the plot shows a very similar trend of Lewis number, although the equivalence ratio is constant and much lower than left of Figure 15.

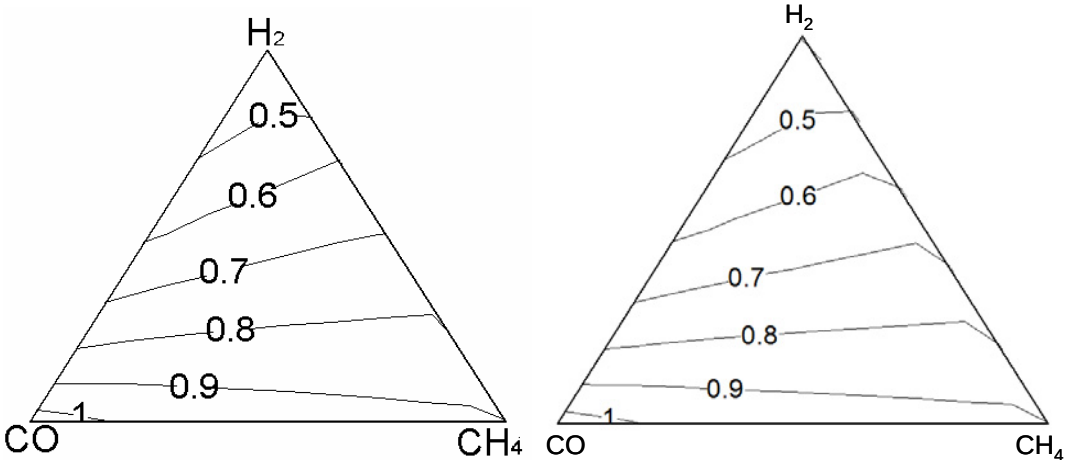

Figure 15: Dependence of mixture weighted Lewis number, Le_{mix}, upon fuel composition at fixed adiabatic flame temperature of 2000 K (left), and at equivalence ratio of 0.6 (right), with 300K reactants temperature.

Figure 16 plots the dependence of the chemical time, $\alpha / S_L^{\,2}$, upon fuel composition at a fixed flame temperature 1500K (left), and constant equivalence ratio of 0.6 (right). Note the order of magnitude variation in chemical time from the fast H_2 mixtures to the slow CO mixtures.

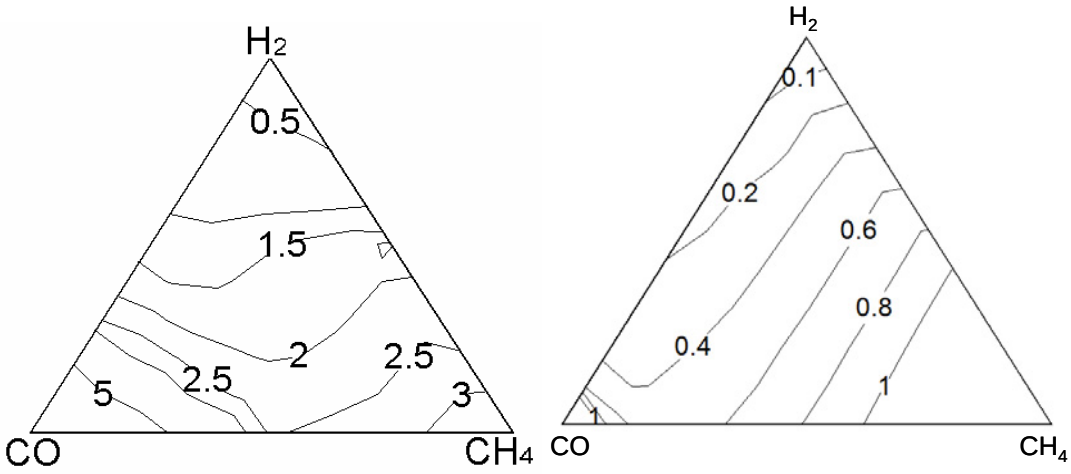

Figure 16: Dependence of chemical time (ms) upon fuel composition at fixed adiabatic flame temperature of 1500 K (left) and equivalence ratio of 0.6 (right).

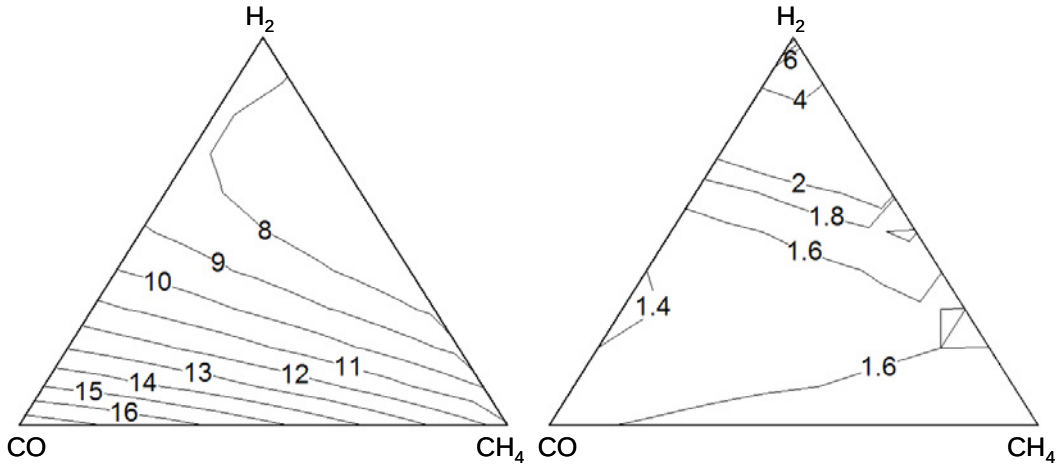

Figure 17: Left: dependence of dynamic viscosity (1.0E3*g/m/s) upon fuel composition; Right: dependence of kinematic viscosity (1.0E5*m^2/s) upon fuel composition;

Viscosities of H_2/CO/CH_4 are plotted in **Figure 17**. Dynamic viscosity ranges from a low of 9 in the high H_2 mixtures to a high of 18 in the high CO mixtures. However, kinematic viscosity shows an opposite trend, high hydrogen mixtures have the high values, while high CO mixtures shows low kinematic viscosities.

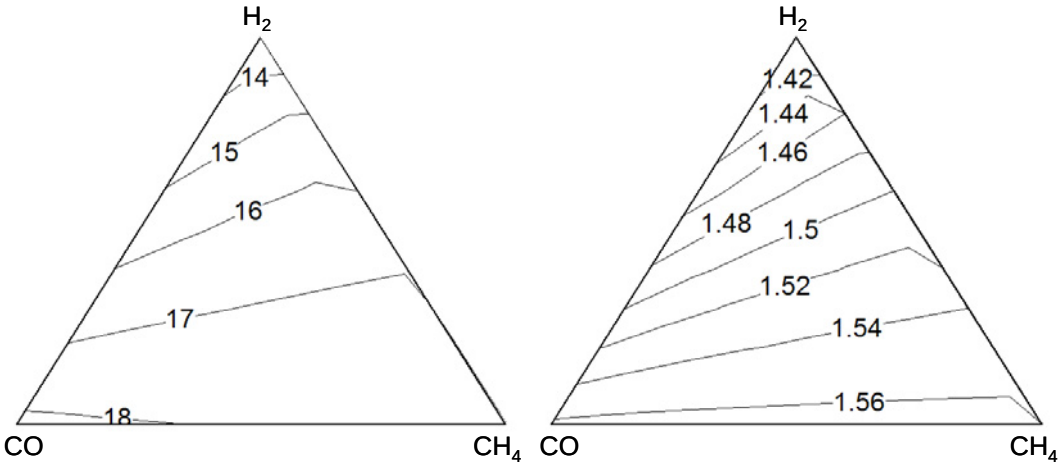

Figure 18: Left: dependence of dynamic viscosity (1.0E3*g/m/s) upon fuel composition at an equivalence ratio of 0.6; Right: dependence of kinematic viscosity (1.0E5*m^2/s) upon fuel composition at an equivalence ratio of 0.6

Viscosities of (H_2/CO/CH_4)/air mixtures at an equivalence ratio of 0.6 are plotted in Figure 18. It shows that the viscosities of fuel/air mixture are very similar for all the mixtures, especially the kinematic viscosity, ν. Reynolds number is defined as

$$\mathrm{Re} = \frac{U_{ref} l_{ref}}{\nu} \quad (42)$$

So with the same approach flow speed, and geometries of combustor, it is clear that Reynolds numbers for different mixtures are also very similar.

Kido and co-workers [78] have emphasized the significance of the relative mass diffusion rates of fuel and oxidizer, D_{fuel}/D_{ox}, over the Lewis number. However, there is nearly a one-to-one correspondence between these two dimensionless parameters for the mixtures considered here, as shown in Figure 19. This figure plots the dependence of D_{fuel}/D_{ox} upon Le_{mix} for a range of H_2/CO/ CH_4 mixtures. As such, in this research, we only consider Le_{mix}, realizing that it is nearly equivalent to mass diffusion ratios. D_{fuel} is

defined as heat-release weighted fuel diffusivity in the air, $D_{fuel} = \sum_{k=fuel} A_k D_{k-Air}$, and D_{ox} is defined as oxygen diffusivity in the fuel and nitrogen.

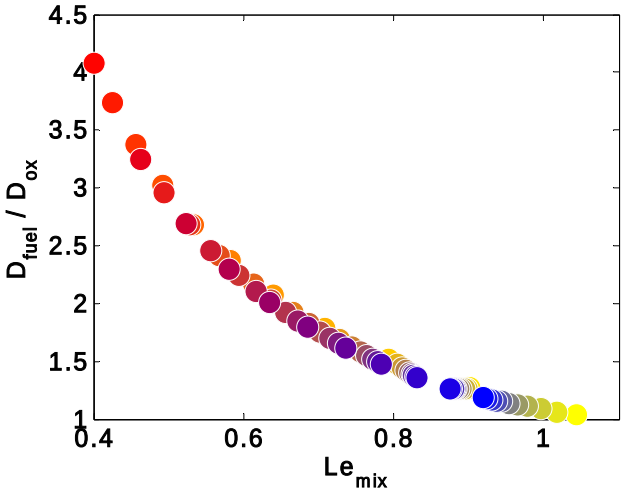

Figure 19: Dependence of D_{fuel}/ D_{ox} upon mixture Lewis number.

CHAPTER 4

CORRELATION OF BLOWOFF LIMITS

This section presents lean blowoff results obtained in the gas turbine combustor simulator. Eight sets of data were taken over a wide range of $H_2/CO/CH_4$ fuel composition under different experimental conditions, which are listed in Table 2.

Table 2: Lists of experimental conditions

	Descriptions	Reactant Temperature (K)	Combustion Pressure (atm)
1	Constant nozzle exit flow velocity of 59 m/s	300	1.7
2	Constant nozzle exit velocity of 39 m/s	300	1.7
3	Constant nozzle exit flow velocity of 59 m/s	458	4.4
4	Constant nozzle exit flow velocity of 39 m/s	458	4.4
5	Constant hot products flow velocity of 10 m/s	300	1.7
6	Constant hot products flow velocity of 17 m/s	300	1.7
7	Nozzle exit flow velocity of 36-39 m/s with constant air mass flow rate	300	1.7
8	Nozzle exit flow velocity of 57-60 m/s constant air mass flow rate	300	1.7

The most comprehensive and complete fuel mixtures were varied in data sets 1, 2, 3, and 4, which are the focuses of the correlation study of this chapter. For these four sets

of tests, lean blowoff results obtained at two constant nozzle exit velocities: 59 and 39 m/s. This corresponds to combustor velocities (cold flow) of 6.0 and 4.0 m/s. Tests were performed at two pressure/temperature conditions: combustor pressure of 1.7 atm and 300 K reactants, and combustor pressure of 4.4 atm and 460 K reactants. The mean equivalence ratios ranged from roughly 0.15 to 0.60.

In order to facilitate presentation of results, these graphs represent the mixture composition of H_2/CO/CH_4 by the colors. Primary colors at the three vertices are used to represent each fuel constituent, where red, yellow, and blue denote H_2, CO, and CH_4, respectively. This is illustrated in **Figure 20**.

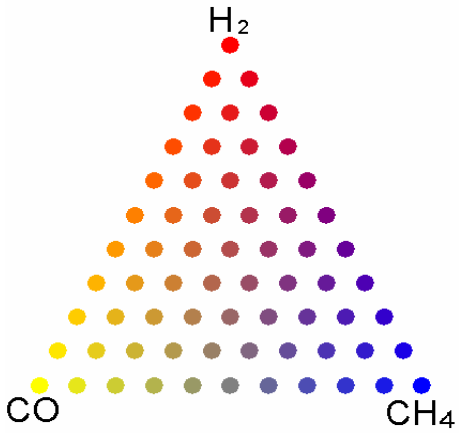

Figure 20: Primary color mixing scheme used to denote fuel blend composition

The basic test plan is to operate at uniformly spaced fuel compositions in H_2/CO/CH_4 space, such as is depicted in the figure above. Obtaining these data was complicated by the need to keep the approach flow velocity, combustor pressure, and mixture temperature constant across the range of fuel compositions. As such, approaching blow off limits with a certain fuel composition required simultaneously

adjusting the air and three fuel flow rates in order to keep constant approach flow velocity. In addition, due to variations in mixture burned gas temperature, maintaining a constant combustor pressure required simultaneous adjustment of the back pressure valve.

However, applying a uniform definition of blowoff is complicated by the fact that the manner in which the flame blew off varied with composition. In many cases, the blowoff event occurred abruptly with a small change in fuel composition, although sometimes proceeded by slight liftoff of the flame from the burner. Defining the blowoff point was unambiguous in these instances; moreover, the point of blowoff and flame liftoff was nearly identical. This was the case for mixtures with mixtures with less than approximately 50% H_2 by volume. However, for high H_2 mixtures, the blowoff and liftoff events were quite distinct. Usually, the flame became visibly weaker, lifted off from the holder, and moved progressively downstream with decreases in equivalence ratio before blowing off for good. As such, blowoff is defined as the point where the flame is no longer visible in the 10.2 cm long optically accessible section of the combustor. Undoubtedly, this variation of liftoff/blowoff characteristics with fuel composition is responsible for some of the scatter in the experimental data. This point should be kept in mind when comparing 0-50% H_2 and 50-100% H_2 containing fuels, see **Figure 21**.

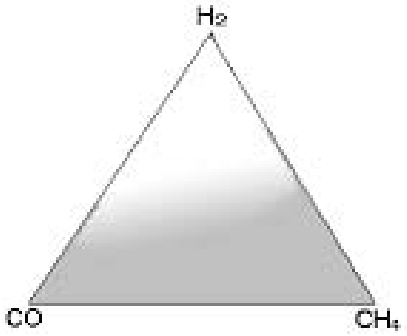

Figure 21: Composition map describing regions where sharply defined blowoff event occurs (gray) and blowoff preceded by significant flame liftoff (white)

These blowout limits were correlated with a variety of parameters. As noted in previous chapters, the presence of H_2 has a strong impact on blowout limits of either H_2/CH_4 or H_2/CO flames. **Figure 22**, which plots the dependence of the blowoff equivalence ratio upon the mole fraction of H_2 in the fuel, shows that H_2 also strongly affects the lean blowout limits of syngas mixtures ($H_2/CO/CH_4$), in spite of the complicated coupling chemical mechanisms among these species. It shows the well known result that, in general, mixtures can be stabilized with lower equivalence ratios as the H_2 concentration increases. However, note that the addition of small amounts of H_2 has small impacts upon blowoff limits and that the sensitivity of the blowoff equivalence ratio to H_2 level variations remains essentially constant across the entire range of H_2 levels. In other words, no discontinuous or abrupt change in blowoff equivalence ratio was observed with small amounts of H_2 addition.

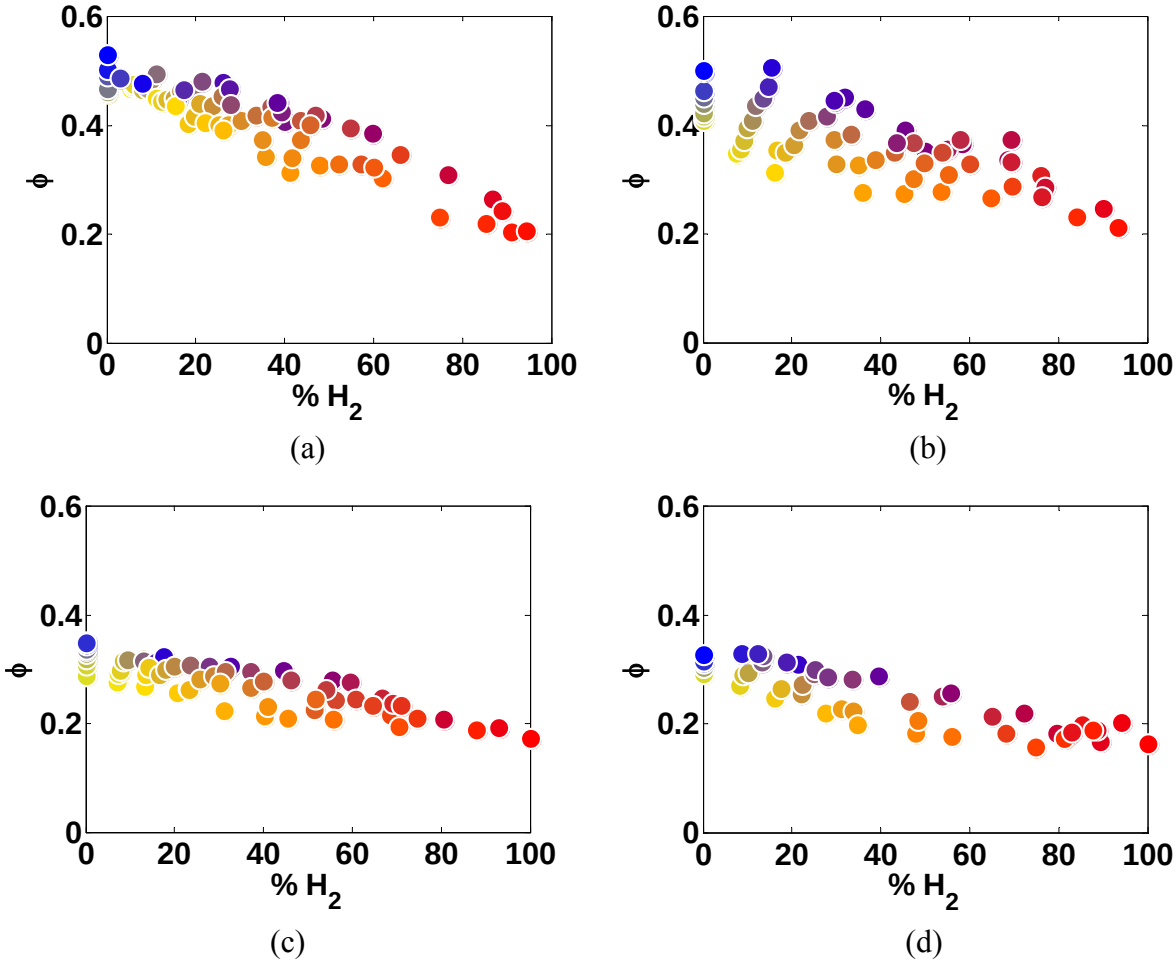

Figure 22: Dependence of LBO equivalence ratio upon H_2 mole fraction at premixer flow velocities of 59 m/s at 300K reactants temperature and 1.7 atmospheres combustor pressure (a), of 39 m/s at 300K and 1.7 atmospheres (b), of 59 m/s at 458K and 4.4 atmospheres (c), of 39 m/s at 458K and 4.4 atmospheres (d).

Besides at constant premixer flow speed, blowoff limits were also obtained at constant air mass flow rate (Figure 23), and constant burned combustor flow speed (Figure 24).

In Figure 23, all the data points were obtained by fixing the air mass flow rate at 49.9 g/s (nozzle exit flow speed of 36-39 m/s)or 74.8 g/s(nozzle exit flow speed of 57-60 m/s), and decreasing the fuel mass flow rate until lean blowoff occurred. In Figure 24, all the tests were performed under a constant burned flow speed inside the combustor, which is estimated as $\frac{T_{ad}}{T_{reactants}} U_{reactants}$.

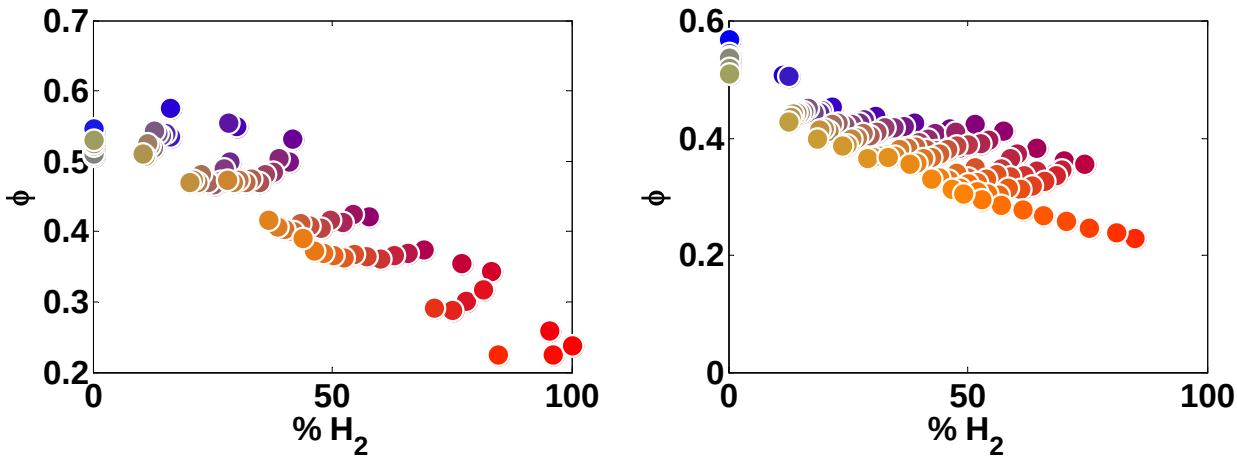

Figure 23: Dependence of LBO equivalence ratio upon H_2 mole fraction at constant air mass flow rate of 49.9g/s (left), of 74.8 g/s (right) at 300K reactants temperature and 1.7 atmospheres combustor pressure.

At one specific H_2 mole fraction, data scatters in a narrow band due to different ratios of CO and CH_4. In general, CO/CH_4 mixtures blow off at lower equivalence ratios as the CO/CH_4 ratio increases, although CO flame has a smaller flame speed and a large chemical time scale. For example, Figure 25 shows the dependence of LBO equivalence ratio of CO/CH_4 mixtures upon CO fraction in cases with no hydrogen addition, which demonstrates this point. **Figure 21** indicates that CO/H_2 flames are easier to blowout in a manner similar to H_2 flame than CH_4/H_2 flames. One possible reason is that H_2 supplies

the OH radical pool, which plays a key role in CO oxidation, by the faster chain-branching reactions. Another possible reason is that CO has a higher adiabatic flame temperature which accelerates the overall reaction rate. For example, at equivalence ratio of 0.6, adiabatic flame temperature of 50%-50% CO/H_2 mixtures is about 1900K, which is much higher than the flame temperature of 50%-50% CH_4/H_2, which is only 1700K. This point can be seen in **Figure 26**.

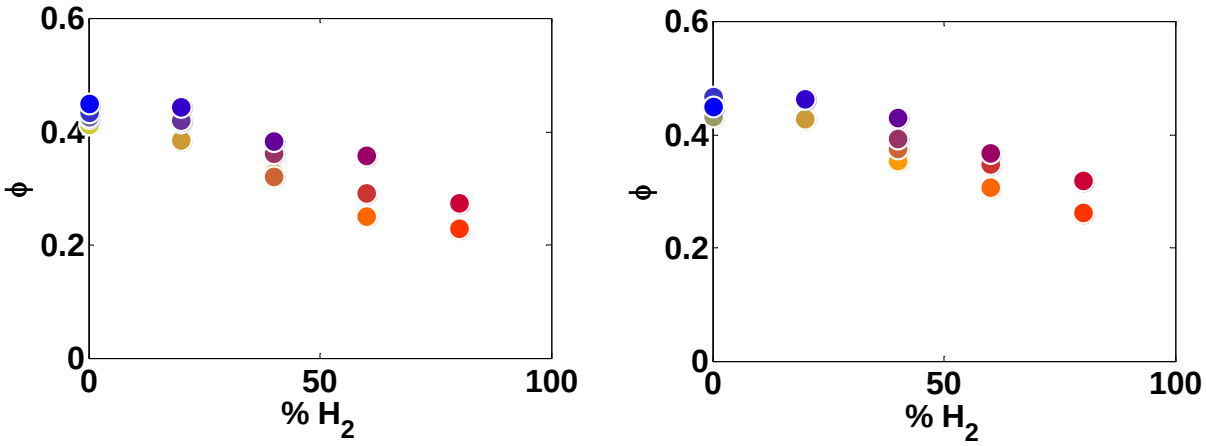

Figure 24: Dependence of LBO equivalence ratio upon H_2 mole fraction at burned combustor flow velocities of 10 m/s at 300K reactants temperature and 1.7 atmospheres combustor pressure (left), of 17 m/s at 300K and 1.7 atmospheres (right),

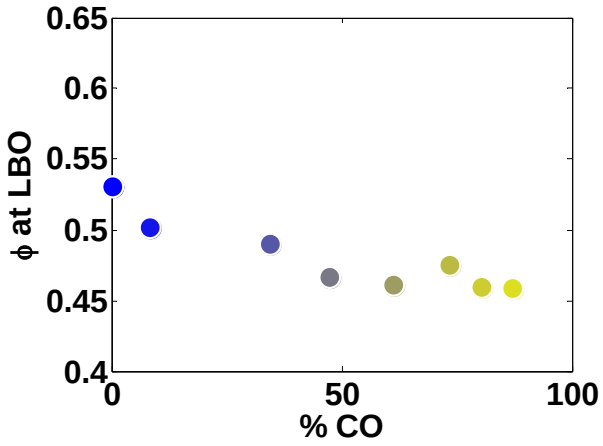

Figure 25: Dependence of LBO equivalence ratio of CO/CH4 mixtures upon CO mole fraction at premixer flow velocities of 59 m/s at 300K reactants temperature and 1.7 atmospheres combustor pressure

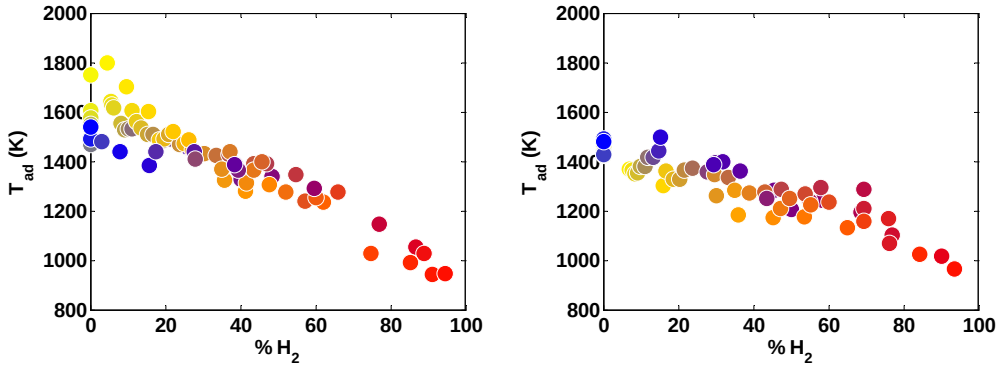

Figure 26: Dependence of adiabatic flame temperature at LBO upon percentage of H_2; 59 m/s (Left) 39 m/s (right), both at 1.7 atmospheres

Next, consider the dependence of adiabatic flame temperature at lean blowout upon the mole fraction of H_2. As shown in **Figure 26**, the data sets as a whole correlate well with these parameters. There is a nice trend between the percentage of H_2 and adiabatic flame temperature at lean blowout. That is, flames which have higher percentage of H_2 could stabilize at a lower adiabatic flame temperature. This

phenomenon was explained by the chemical kinetics in some research works [40, 41, 42, 43]. It was said that higher radial concentration due to hydrogen breakdown plays an important role in H_2 enhanced flames.

Another possible reason for this trend could be the high diffusivity of hydrogen. It is well known that hydrogen has a much higher mass diffusivity than other fuels, as described in previous chapter. When the flame is highly stretched, the local flame properties are significantly changed from the averaged properties, such as equivalence ratio, or flame speed. For lean hydrogen mixtures, the local equivalence ratio is higher than the averaged value, so that the flame can sustain itself at a lower averaged equivalence ratio or flame temperature.

At one specific H_2 fraction, CO mixtures have a higher temperature level (more obvious at low H_2 mole fractions in Figure 26 (a)). It is also noticeable that the adiabatic flame temperature is more sensitive to the percentage of H_2 for the higher flow speed case due to the overall higher stretch rate it has.

Similarly good correlations between the laminar flame speed, Lewis number, and a number of other combustion parameters at blowoff upon H_2 level were observed, such as (b) of **Figure 27** , and (b) of **Figure 29**. This brings us to an important point that must be recognized in extracting an understanding of the blowoff physics from these correlations. First, blowoff limits are clearly a strong function of H_2 levels. Second, many other parameters, such as diffusivities, flame temperature, etc. are also strong functions of H_2 level. ***As such, it is important to not draw conclusions about blowoff physics only because one can correlate results with parameters that are simply functions of the H_2 percentage.*** For example, a very nice correlation between T_{ad} vs. *Le*

at blowout exists, because both of them are functions of percentage of H_2. In other words, regardless of whether the mixture *Le* is a physically meaningful parameter, a good correlation will still be observed. In some sense, this is analogous to correlating T_{ad} vs $2*T_{ad}$ at blowoff – obviously, a perfect correlation is observed, regardless of whether this is a physically significant parameter.

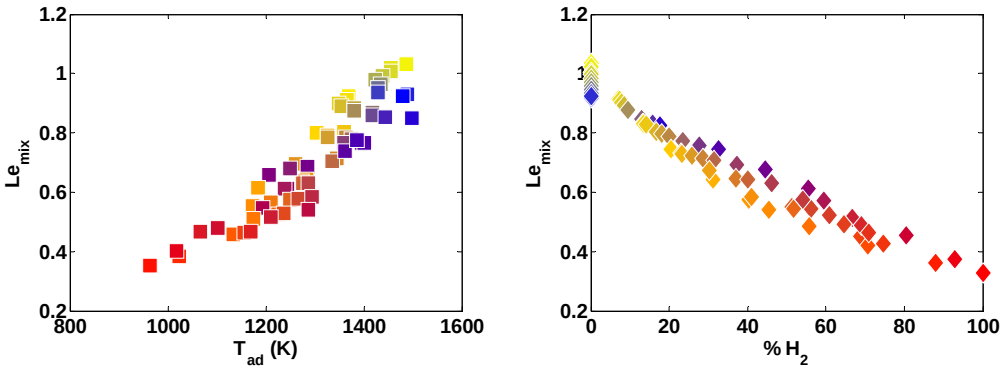

(a) (b)

Figure 27: Dependence of Lewis number (a) upon adiabatic flame temperature at LBO at 39 m/s and 1.7 atm (b) upon percentage of H_2 at 59 m/s and 4.4 atm

For example, Lewis number of the mixture, Le_{mix}, is a key parameter for the flame instability or flame propagation for stretched flame or turbulent flame, so using Le_{mix} to correlate the lean blowout data is reasonable and meaningful. Now, consider correlating these blowout results with Lewis numbers, Le_{mix}, see Figure 27 (a). The correlation is quite good in all instances, although only one result is shown. However, in light of the comments in the last paragraphs of this section, some care must be taken in placing too much emphasis on this point, as the Lewis number is very closely related to the H_2 percentage, Figure 27 (b). A nearly linear relation exists between Le_{mix} and percentage of

H_2. This is because the diffusivity of H_2 is much larger than that of CO or CH_4, so the percentage of H_2 dominates Le_{mix}.

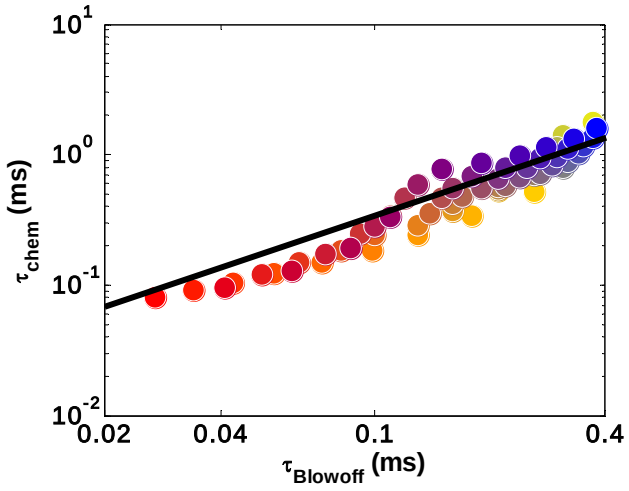

Figure 28: Relationship between chemical time calculated by α/S_L^2 and blowout residence time for H_2/CO/CH_4 mixtures at ϕ=0.6. Results obtained using AURORA and PREMIX in CHEMKIN with GRI 3.0 mechanism

Laminar flame time scale, approximated as $\tau_{chem} = \alpha/S_L^2$, was discussed in chapter 3. However, at some high H_2 lean mixtures where stable flames were observed, flame speed calculations did not converge, thus making τ_{chem} estimates impossible. For this reason, blowoff residence time, $\tau_{Blowoff}$, was used here to scale chemical time. Figure 28 compares the blowoff residence time, $\tau_{blowoff}$, of a well stirred reactor model to the chemical time from α/S_L^2 for several H_2/CO/CH_4 mixtures. The two time scales are closely related, with a best fit given by $\tau_{chem}=3.4*\tau_{blowoff}$ (denoted by the solid black line) except for cases with greater than 95% CO (not shown). In this work, $\tau_{blowoff}$ was used in estimating chemical times, for the pragmatic reason that they are much simpler and easier

to calculate for lean flames. The results in Figure 28 were calculated using CHEMKIN with GRI 3.0 mechanism. Another mechanism, C1 mechanism, was also used to determine the relation between τ_{chem} and $\tau_{Blowoff}$. Although the absolute values of these two time scales are slight different, the general relation between them is similar.

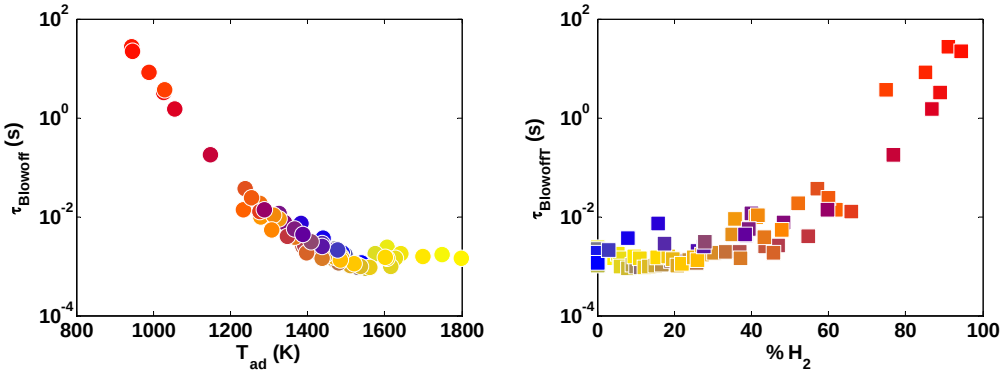

(a) (b)

Figure 29: Dependence of blowoff residence time (a) upon adiabatic flame temperature at LBO, 59 m/s (b) upon percentage of H_2 at 39 m/s, both at 1.7 atm

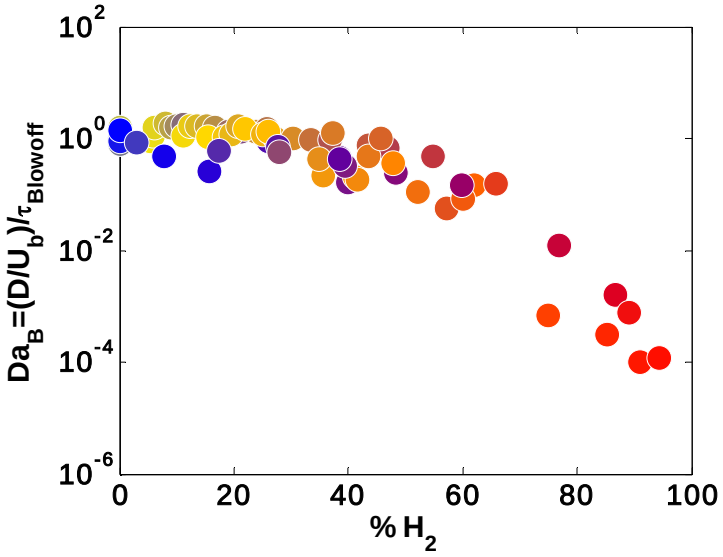

Figure 30: Damköhler numbers of mixtures at constant premixer flow speed of 59 m/s at 300K reactants temperature and 1.7 atm combustor pressure.

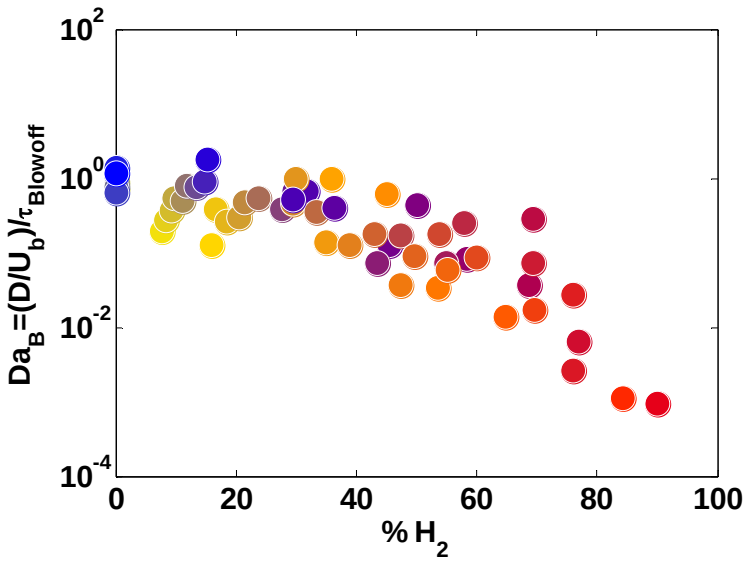

Figure 31: Damköhler numbers of mixtures at constant premixer flow speed of 39 m/s at 300K reactants temperature and 1.7 atm combustor pressure.

As shown in Figure 29 (a), it is noticeable that there are two parts of the correlation between flame temperature and blowoff time. One region is $T_{ad} > 1300K$, $\tau_{Blowoff}$ changes slowly with T_{ad}, and the other is $T_{ad} < 1300K$, where $\tau_{Blowoff}$ changes greatly with T_{ad}. These two parts are associated with the time scale shown in Figure 29 (b), 0-50% H_2 and 50-100% H_2. Considering the different definitions of blowout for these two parts in the previous section, it is necessary to analyze these data separately.

Damköhler (*Da*) number correlations were found to correlate the data over all flow velocities, pressures and temperatures for all mixtures with H_2 levels below 50%, as shown in **Figure 30** and **Figure 31**. In these plots, the reference length scale, *D*, was the combustor width, 5.1 cm. In this study, since the same combustor geometry and same premixer flow speed were used for each set of data, all the length scales, such as integral length scale, length of recirculation zone, thickness of the shear layer, and geometry of the combustor, are all inter-correlated. So several physically plausible length scales can

be used in this Damköhler number correlation with similar resulting trends (although the values of *Da* will be different). Damköhler numbers were evaluated using both the unburned flow speed, Da_U, and burned flow speed, Da_B, as reference velocity scales. Utilizing the burned gas speed resulted in slightly better ability to correlate the data, as reflected in slightly lower errors (about 10 %) in predicted blowoff equivalence ratio, $\delta\phi_{rms}$ (described below), and so is used for these results. **Figure 30** shows that blowout occurs at a nearly constant *Da* for these composition values (although **Figure 30** was plotted in *logarithm* scale, $\tau_{Blowoff}$ is an exponential function of equivalence ratio). At the same time, **Figure 30** also shows that a constant *Da* correlation is inadequate for describing blowout limits of higher H_2 level mixtures. It is possible that this is simply a reflection of the fact that the blowout process changes with H_2 levels and that our "blowoff definition" is not the most physically meaningful, see discussion of **Figure 21**. For example, perhaps identifying the point where the flame first lifted off the flame holder would have been more useful.

A second possibility for this change in blowoff *Da* value shown in **Figure 30** and **Figure 31** may be due to preferential diffusion effects, a consideration that has also been used to scale changes in turbulent flame speed of mixtures whose constituents have significant variations in diffusivity. One approach for incorporating these effects is to note that the local equivalence ratio changes along the wrinkled flame, being both higher and lower than the average at different spatial locations. Kido and co-workers [36] suggested correlating mixture turbulent flame speeds by utilizing mixture properties at an adjusted equivalence ratio, ϕ_{adj}; i.e., not at the average equivalence ratio, ϕ_{ave}, but the

average value plus some $\Delta\phi$. As such, mixture properties are correlated at $\phi_{adj}=\phi_{ave}+\Delta\phi$. They suggest the following relation for $\Delta\phi$, based upon empirical fits of their data:

$$\Delta\phi = C * \ln(D_F / D_{OX}) \qquad (43)$$

where D_F and D_{OX} denote the mass diffusivity of fuel and oxygen, respectively, and C is an empirical constant whose value they suggest as 0.3. **Figure 32** shows the dependence of ϕ_{adj} upon ϕ_{ave}. $\Delta\phi$ is also a function of percentage of H_2, and high H_2 mixtures have a higher equivalence ratio increase.

It was found that utilizing a value of C close to 0.1 gives a nearly constant blowoff Damköhler number for all of our data sets, **Figure 33** and **Figure 34**. This plot shows that blowoff occurs at a nearly constant value of local Damköhler number, where the $\tau_{Blowoff}$ is estimated at the equivalence ratio $\phi_{adj}=\phi_{ave}+\Delta\phi$. In this case of **Figure 34**, the best value for C=0.07 and the average value over all the test points of $\overline{Da_B}$, at blowoff is 0.2.

Table 3 summarizes the results from the other two tests by presenting the best fit value for C for each individual data set and the corresponding $\overline{Da_B}$ value. It can be seen that $\overline{Da_B}$ does vary somewhat with each data set, but is always an O(1) quantity.

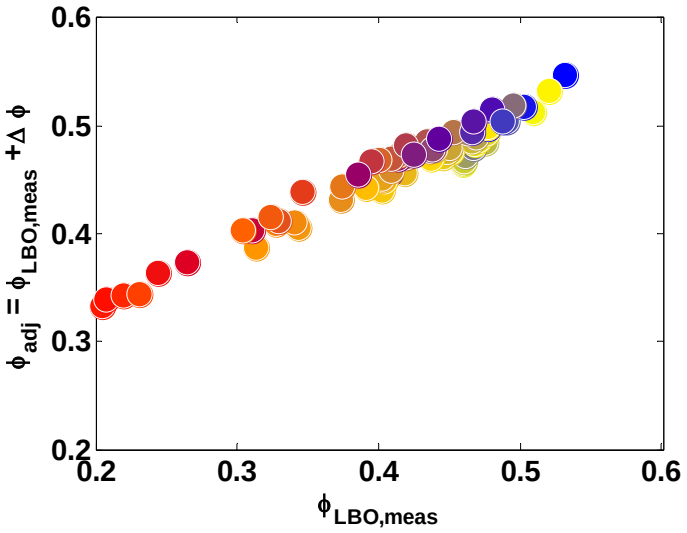

Figure 32: ϕ_{adj} of mixtures at constant premixer flow speed of 59 m/s at 300K reactants temperature and 1.7 atm combustor pressure.

In order to quantify the scatter in the correlations shown in the table and the capability for actually inverting the above procedure to be used as a blowoff prediction methodology, the following procedure was employed. Assume that the equivalence ratio at blowoff is now the unknown and must be predicted, $\phi_{LBO,pred}$. Assume also that the Damköhler number at blowoff is known and equal to the value $\overline{Da_B}$ compiled in the table. Then the following implicit equation for $\phi_{LBO,pred}$ is solved for each fuel composition:

$$\overline{Da_B} = \frac{d}{U_b \tau_{Blowoff} (\phi_{LBO,pred} + C \ln(D_F / D_{ox}))} \qquad (44)$$

This procedure is repeated for each fuel composition. In general, $\phi_{LBO,meas}$ and $\phi_{LBO,pred}$ are not identical, and so the root mean square (rms) of their difference over all the data points is referred to as $\delta\phi_{rms}$ in the table As can be seen, assuming a constant Damköhler number at blowoff results in a capability for predicting the equivalence ratio value to within about 0.02 - 0.04.

Table 3: Summary of optimum model constants for correlating blowoff data and resulting scatter in fitted data.

Test group	Best Fit *C* Value		
	C	$\overline{Da_B}$ at ϕ_{adj}	$\delta\phi_{rms}$
T=300 K P=1.7 atm U_0=59 m/s	0.1	2.1	0.04
T=300 K P=1.7 atm U_0=39 m/s	0.08	1.1	0.03
T=458 K P=4.4 atm U_0=59 m/s	0.07	0.2	0.02

Due to the exponential dependence of $\tau_{Blowoff}$ upon equivalence ratio, varying the precise value of $\overline{Da_B}$ or C does not substantially impact the errors in $\phi_{LBO,pred}$. For example, in the first case above, assuming blowoff occurs at constant values of *Da*=1.0 or 3, instead of the best fit value of 2.1, results in $\delta\phi_{rms}$ =0.045 and 0.043, respectively.

Moreover, both T_{in}=300K, *P*= 1.7 atm data sets can be reasonably collapsed with a single $\Delta\phi$ equation or *C* value. To illustrate, **Figure 35** compares the predicted and actual blowoff equivalence ratios for all low temperature data taken in this study, assuming *C*=0.1 and $\overline{Da_B}$=1.7. It can be seen that the error in $\phi_{LBO,pred}$ is generally less than 0.05, and $\delta\phi_{rms}$ = 0.045. Moreover, the highest errors are encountered with the very high CO mixtures, which may simply be a manifestation of the sensitivity of high CO mixtures to ambient humidity levels and other factors influencing H levels. If the P=4.4 atm, T=460 K data set were also plotted, they would also cluster along a line, but with a systematic difference from the grouping in this graph., In other words, the optimum model constants (particularly the C value) vary with operating conditions.

There are a variety of reasons that the remaining scatter could be present, such as inherent noise in the blowoff equivalence ratio. In addition, other more subtle factors, such as reference length and reference flow velocity could easily change somewhat with approach flow velocity.

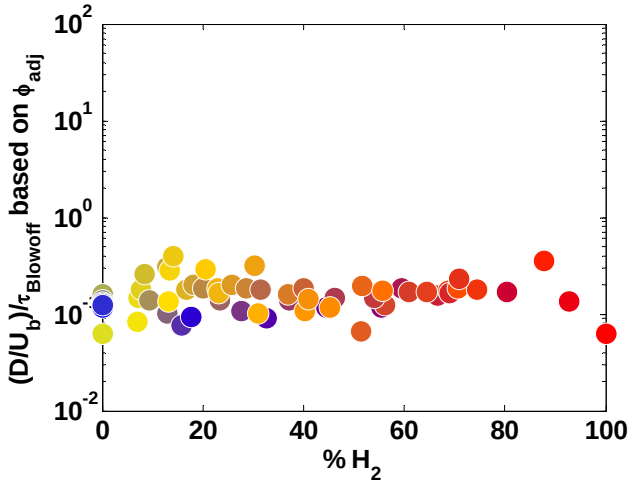

Figure 33: Damköhler numbers of mixtures based on local equivalence ratio at premixer flow velocities of 59 m/s at 458K reactants temperature and 4.4 atm combustor pressure.

It should be emphasized that the *C* value in the $\Delta\phi$ calculation was chosen *empirically* to give the best fit. Although the *Da* mechanism, considering preferential diffusion effects, could correlate and predict the lean blowout limits very well, the real physical meaning behind these correlations are uncertain. Moreover, it should be emphasized that the latter $\Delta\phi$ correction may not necessarily reflect underlying physics, but simply be another manifestation of the fact that the blowoff limits are a strong

function of H_2 levels (note that $\Delta\phi$ is closely correlated with the percentage of H_2, see **Figure 32**.

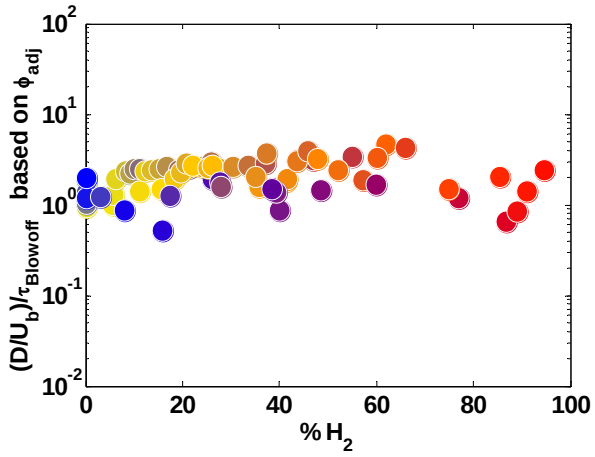

Figure 34: Damköhler numbers of mixtures based on local equivalence ratio at premixer flow velocities of 59 m/s at 300K reactants temperature and 1.7 atm combustor pressure.

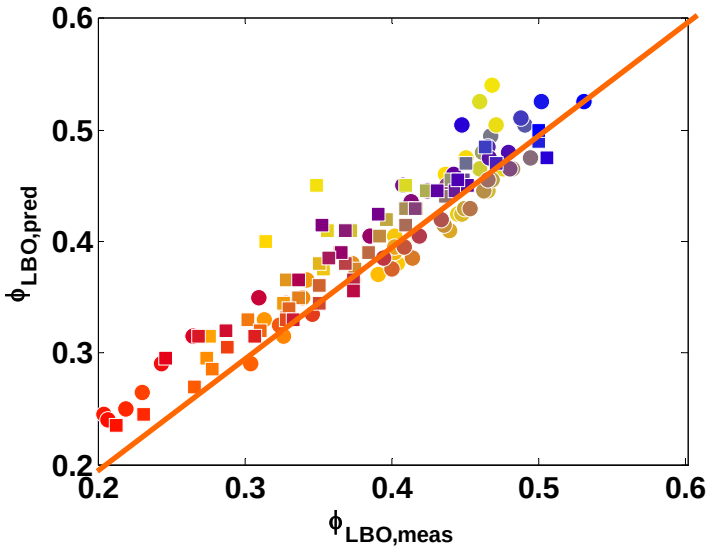

Figure 35: Comparison of predicted and measured blowoff equivalence ratio for all T=300 K, p = 1.7 atm data. Circle:U_0= 59 m/s, Square: U_0= 39 m/s.

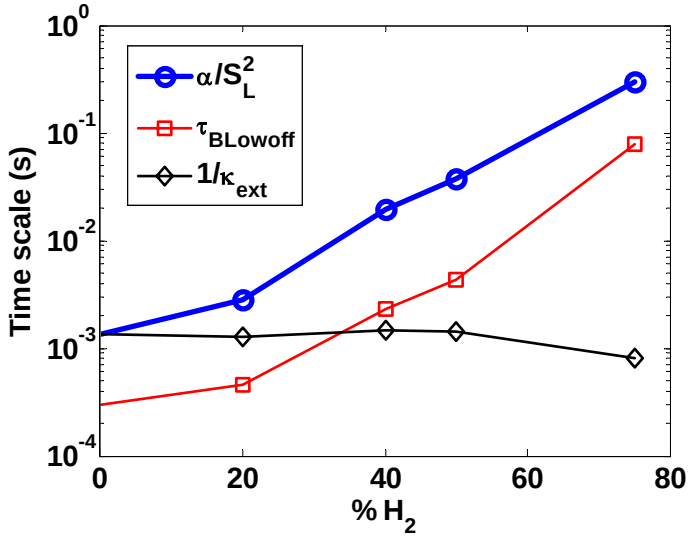

Figure 36: Comparison of three chemical time scales for unsteady H_2/CH_4 flames. The detailed equivalence ratios are shown as the red points in Figure 58.

The *Da* correlation in **Figure 31** and **Figure 32** can also be improved by using the reciprocal of extinction strain rate as the chemical time scale. Extinction strain rates for $H_2/CO/CH_4$ mixtures are not available, but the results for H_2/CH_4 mixtures from chapter 6 show the basic trend. **Figure 36** shows three chemical time scales for H_2/CH_4 mixtures at the unsteady/stable boundary. (The details for these test conditions are discussed in chapter 6 and indicated as the red points in **Figure 58**.) It shows that, as discussed above, α/S_L^2 and $\tau_{Blowoff}$ are closely related, and both of them significantly increases with the hydrogen level in fuels. However, all these mixtures cross the unsteady/stable boundary at a nearly constant extinction strain rate (κ_{ext}). This result suggests that Damköhler number based on extinction strain rate will also be nearly a constant for H_2/CH_4 mixtures at the unsteady/stable limit. For highly strained flames, such as a swirling flame, the

fundamental flame properties are greatly affected by the flame strain. However, either PREMIX or AURORA from CHEMKIN does not include the strain effects. Diffusion effect to flame stability is also emphasized by these results. The Da based on blowoff residence time can not correlate the data, see **Figure 30**. However, Da with diffusion effects correlates the limits very well. In addition, the extinction strain rate, calculated with the diffusion effects, also models the limits well. This suggests that diffusion phenomenon is important to blowoff.

CHAPTER 5

FLAME DYNAMICS NEAR BLOWOFF

In the previous section, it was noted that the phenomenology of blowoff changed markedly with H_2 levels in the fuel, see discussion of chapter 4. For lower H_2 mixtures (~<50% H_2 by volume), the blowoff event occurred abruptly and was precipitated by a small reduction in fuel/air ratio (although sometimes preceded by slight liftoff of the flame from the burner). However, for high H_2 mixtures, the flame liftoff and blowoff events were quite distinct. Furthermore, as the mixture approached blowoff, the flame becoming visibly weaker, lifted off from the holder and moved progressively downstream. Finally, it was noted that the definition of blowoff at these very high H_2 levels was somewhat arbitrary and very much a function of the definition of "blowoff".

The objective of this chapter was to follow up on these observations and systematically characterize the blowoff phenomenology as a function of the H_2 levels in the fuel. This work was accomplished through high speed visualizations of the flame emission and velocity field measurements.

However, it should be emphasized that blowoff phenomenology is very strongly affected by boundary conditions, such as the geometry of the combustor and inlet flow conditions. In another words, blowoff phenomenology is geometry dependent and is a function of boundary conditions, such as the degree of constriction of the exhaust nozzle. The results in this chapter were obtained under same boundary conditions. Given that the variable influencing these dynamics is H_2 level, only CH_4/H_2 mixtures were considered in this study.

5.1 OH* Chemiluminescence

The extinction/reignition events of methane flames has been studied and characterized in burners using different stabilization mechanisms, pilot, bluff body, and swirling flow [10, 11, 12, 13]. In the swirling flame, it has been showed that the swirling flame tends to oscillate between extinction and reignition phases, and the number of extinction/reignition events per unit time monotonically grows as blowoff is approached. The characteristics of extinction/reignition events for H_2/CH4 were studied by OH chemiluminescence measurements.

Figure 37 shows the OH chemiluminescence signal from an optical probe which was focused at the inner recirculation zone, see chapter 2 for details of experimental setup. Because the level of chemiluminescence signal is proportional to the rate of heat release, which is varying with equivalence ratio, the OH signal is normalized by its mean value. Following Muruganandam's method [53], local extinction is defined to begin at the point where the intensity of the signal drops lower than some threshold, and end when the signal goes above this threshold. However, sometimes during a local extinction the signal oscillates above and below the threshold. As such, a second threshold was defined a little higher than the first threshold to make sure that this is only counted as one event. For this example, 0.3 and 0.5 were used as the first and second thresholds for local extinction. Data in **Figure 37** was collected for the CH_4/Air flame near blowoff. It can be seen that unsteady events are characterized by an almost complete loss of chemiluminescence signal quickly followed by a strong signal spike. This corresponds to a local extinction of the flame followed by a strong reignition of the flame. The local extinction events are circled in this plot. These distinctive extinction and reignite span a

period from O(1s) to O(0.001s), without any obvious periodicity or frequency prior to lean blowout. **Figure 38** shows the power spectral density of the signal for ϕ / ϕ_{LBO} of 1.3, 1.1, and 1.01. There is no qualitative change in the spectrum as LBO limit is approached. For example, there are no coherent, periodic oscillations occurring near the blowout limit. The only obvious peak is at 250 Hz, which is related to the natural frequency of the combustor.

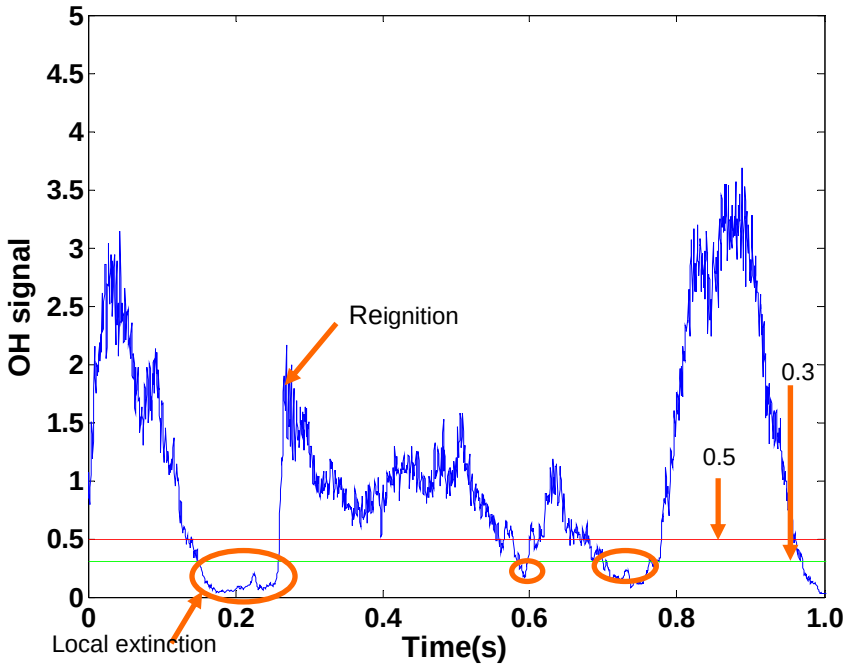

Figure 37: Time series data of OH signal of extinction-reignition events

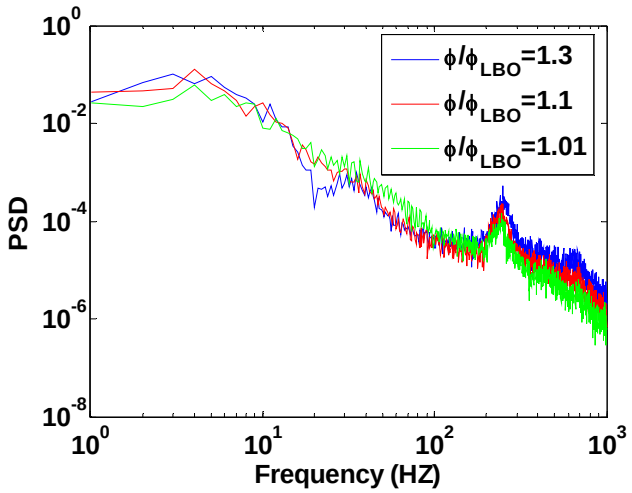

Figure 38: Power spectral density (PSD) of OH signal for CH_4 flames at different equivalence ratios

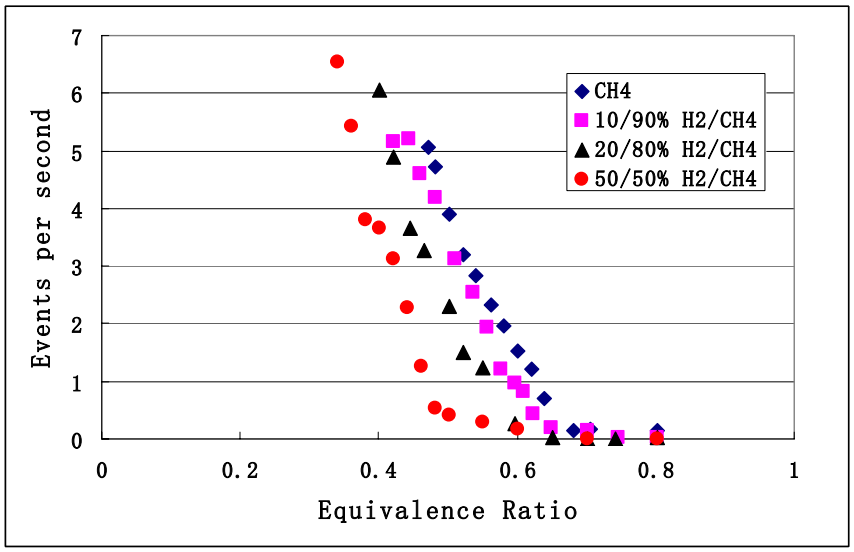

Figure 39: Dependence of events numbers upon equivalence ratio for different fuels

As the LBO limit is approached, more of these events occur in a given time period and thus the time between two such events decreases. **Figure 39** shows the dependence of the number of events per second on the equivalence ratio for five H_2/CH_4 mixtures.

The data shows that flames can be stabilized at lower equivalence ratios with increasing H_2 percentage. When the flame is approaching the lean blowout, the number of events increased greatly, indicating that the flame undergoes extinction events more frequently and undergoes a longer time in the extinction phase. As a consequence, the flame has a shorter and shorter time to reignite and sustain itself.

5.2 High Speed Images

This section describes the dynamics of near blowoff flames by high speed images. Tests were performed at room temperature, atmosphere pressure, and constant nozzle exit velocity of 29m/s.

A qualitative stability diagram of H_2/CH_4 mixtures is shown in **Figure 40**. The regimes are differentiated by visual observation. For a given fuel composition, as we move vertically down the chart by reducing fuel/air ratio, at some point a certain level of "enhanced unsteadiness" becomes evident, indicated by the upper dashed line. For low levels of H_2, further reductions in fuel/air ratio cause blowoff, indicated by the lower solid line. At higher levels of H_2, an additional flow regime, associated with a columnar flame zone is also present. This columnar region will be discussed later in this chapter. The four solid blue circle points represents the four cases studied in detail by high speed imaging. Note that there is a monotonic reduction in blowoff equivalence ratio with increasing H_2 levels, consistent with prior discussion.

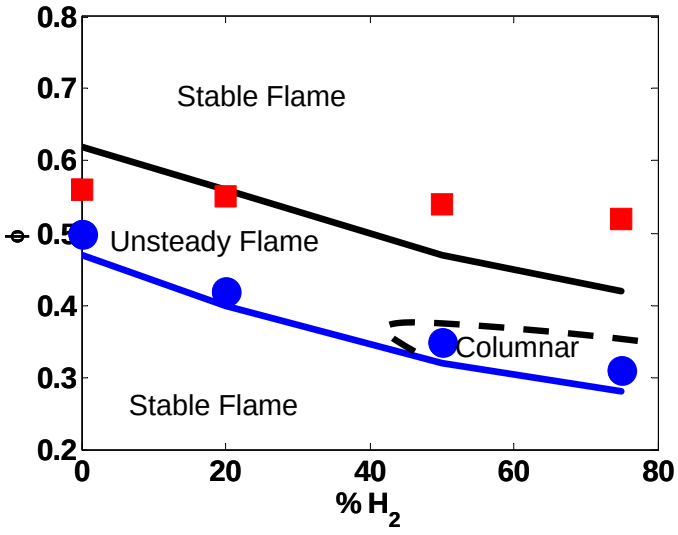

Figure 40: Diagram of flame stability with different H_2 addition levels.

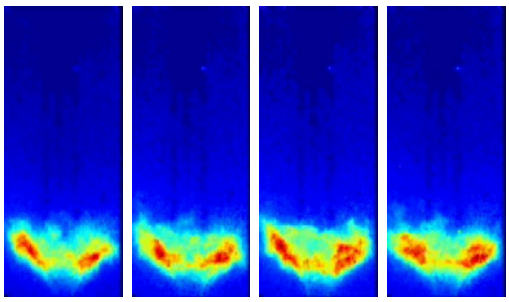

Figure 41: Consecutive images of stable CH_4/Air flame (ϕ =0.7; images separation =10ms)

To provide a baseline, a set of stable flame images are provided in **Figure 41**, which shows chemiluminescence gray scale image (intensity based coloring code) at an equivalence ratio of 0.7. The definition of equivalence ratio is based on the overall fuel mixture. It should be noted that these colorized images are difficult to interpret if viewed

in grayscale. The boundary of the images corresponds to the combustor walls. A compact V shaped flame[1] stabilizes slightly downstream of the nozzle exit. There are minimal reactions at the two corners between the combustor wall and the dump plate, where the flow is recirculating (referred to here as the Corner Recirculation Zone, CRZ).

A typical extinction/reignition process for a natural gas flame near blowoff is shown in **Figure 42**, at an equivalence ratio of 0.5. Moving from (a) to (g), the flame gradually weakens in intensity, particularly about half way up the image in the axial direction. In addition, it lengthens axially, reverting from a more compact region in (a) to an axially distributed region in (d) and (e). In images (f) and (g), the axially distributed flame appears to split into two sections, with hardly any radiation evident from the center. This region reignites in images (h)-(j) which leads to a more axially uniform, but axially compact intensity distribution in (k) and (l), similar to the image in (a). Although not obvious in these images except for (i), the "reconnection" of these two axial regimes appears to occur through a helical tube. This process outlined above repeats itself more and more frequently as the flame approaches blow out.

Also evident in these figures are the dynamics of the flame zones near the premixer exit. In (a), no flame is visible in the corner recirculation zone (CRZ) or at the nozzle exit. Moving to (b) and (c), the flame intensities decreases, but combustion is present in the CRZ. These CRZ flames extinguish in (d) and (e), but are sometimes replaced by a sporadically appearing flame that goes almost to the nozzle exit in (d), (f) and several other images. The movement of the flame toward this very high velocity

[1] This V-shape is not obvious from these images due to the integration of light intensity over the line of sight, but very obvious from direct visualizations.

region suggests axial translation of the inner recirculation zone (IRZ), associated with the vortex breakdown bubble.

Measurements of OH chemiluminescence signal collected by an optical fiber directed at the IRZ also show the flame intensity oscillations. During the phase at which the flame intensity is decreasing, it is possible that unburned fuel is entering the combustor, mixing with the burned hot products and active radicals. At some point a well-stirred reactor-like region is present which combusts and supplies a 'spark' to reignite the whole flame.

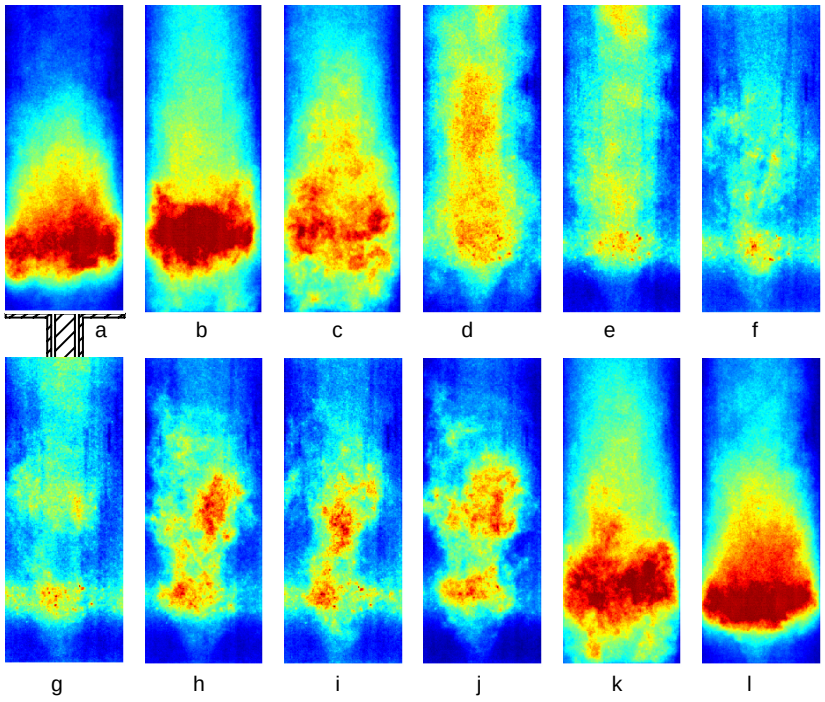

Figure 42: **Consecutive images of CH_4/Air flame under near blowoff conditions (ϕ =0.5; images separation ≈10ms)**

The extinction/reignition process is not periodic, but appears randomly with the average spacing between successive events decreasing as blowout is approached.

Although not shown, measurements of OH chemiluminescence signal shows that the period of this extinction/reignition process varies between 10 – 200 ms for the case in **Figure 42**. Furthermore, each extinction/reignition event does not necessarily follow the identical sequence shown in **Figure 42**. For example, the flame can just move up and down axially, as in **Figure 42** (a-c).

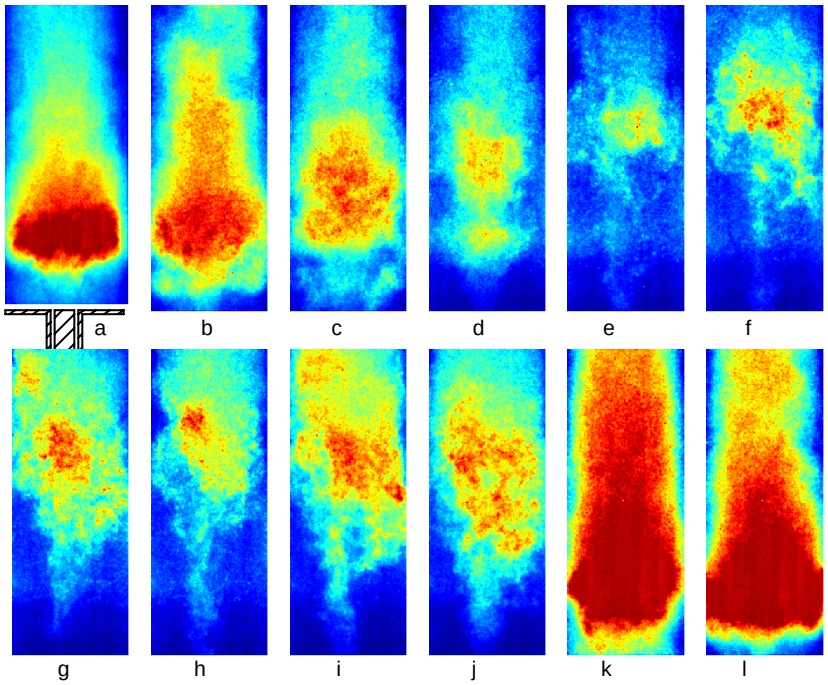

Figure 43: Consecutive images of 80%CH_4 --20% H_2 flame under near blowoff conditions (ϕ =0.42; images separation ≈10ms)

Next, consider the effects of H_2 addition to the CH_4 flame. **Figure 43** shows images for an 80%CH_4 -20%H_2 flame at ϕ=0.42. Many of the processes in **Figure 43** and **Figure 42** are very similar but there are some differences. Comparing the lowest intensity levels for CH_4 flame (f in **Figure 42**) and 20%H_2 addition flame **(**e in **Figure 43),** shows that the lower flame region is of lower intensity (c-d) or in some cases

essentially gone (g-i), except for a helical tube that extends downward. Apparently, the strong reignition event in (k) and (l) is precipitated by flame propagation down this tube.

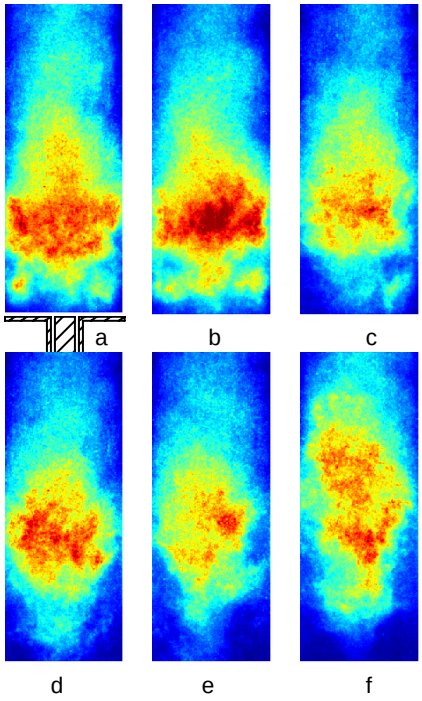

Figure 44: Consecutive images of 80%CH_4 --20% H_2 flame under near blowoff conditions (ϕ =0.42; images separation =2ms)

Although the details are not fully understood, there are some interesting dynamics associated with flame stabilization in the IRZ and CRZ. We hypothesize that the CRZ is normally full of recirculating hot products, with minimal combustion there. As the flame moves downstream, it is anchored by the IRZ (see f-j). However, the CRZ is presumably also now filling with unburned reactants. This region extinguishes and reignites occasionally (see b, c, k), often times with different dynamics than that of the rest of the flame. This reignition can be prompted by flame flashback through the central core region or along the combustor wall by a fluctuation of temperature [79] or just the local

turbulent vortex motion [80]. Once reignited, the flame in the CRZ supplies heat and active radicals to the V-flame, helping it reattach to the centerbody or stabilize as a lifted V-flame, see **Figure 44** (a, b). However, by doing so, it "starves" itself of reactants, extinguishes, and then becomes a region of recirculating hot products, such as shown in the sequence of **Figure 44** (a-d). Note also that because the CRZ is located between the combustor wall and the cold dump plate, the heat loss rate is very high, so that the flame in the CRZ may quench easily. Once the CRZ flame is gone, the V-flame loses some of its "pilot" and moves back downstream axially.

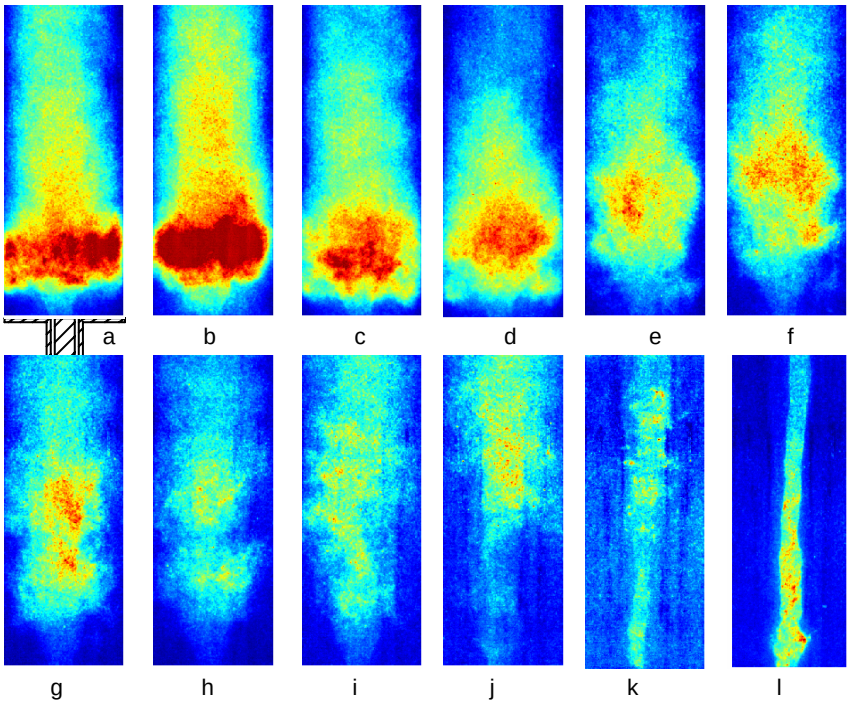

Figure 45: Consecutive images of 50%CH_4 --50% H_2 flame under near blowoff conditions (ϕ =0.35; images separation ≈10ms)

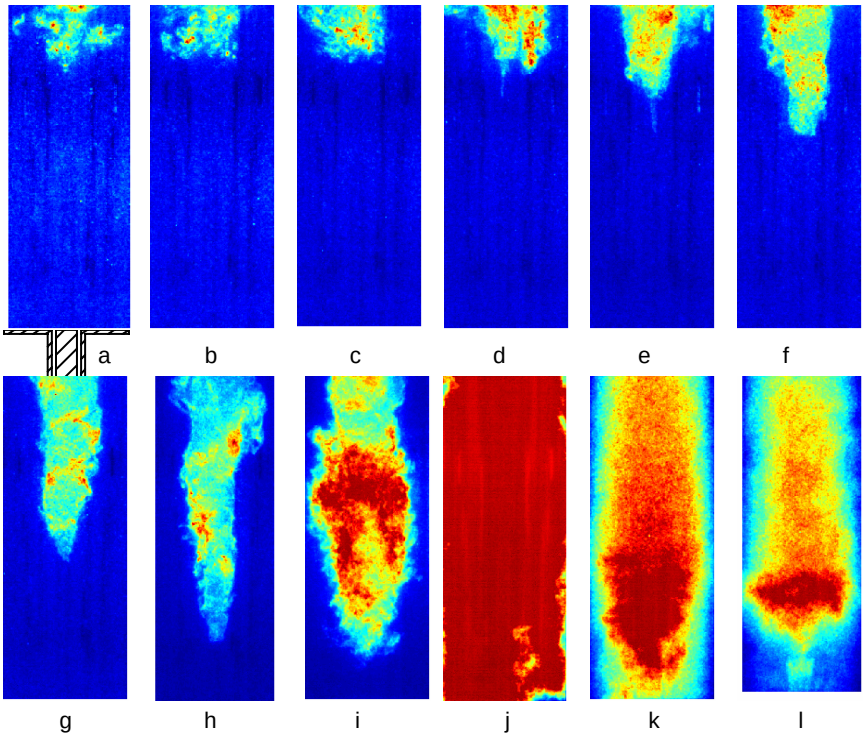

Figure 46: Consecutive images of 50%CH_4 --50% H_2 flame under near blowoff conditions (ϕ =0.35; images separation ≈10ms)

Figure 45, Figure 46 and Figure 47 for a 50%CH_4 -50% H_2 flame at equivalence ratio of 0.35. Starting with **Figure 45** (a) to (j), the flame intensity weakens gradually and the majority of the radiation intensity moves downstream. A flame is still evident within the helical tube (flame propagation is outward, the center is filled with hot products – evident from the seed density in PIV images), which through either reignition or propagation downward, propagates back to the nozzle exit. However, in some cases, the flame is not present in this helical tube and is almost completely blown out, before abruptly propagating back upstream, see **Figure 46.** Flame propagation outward from this columnar tube plays an important role in the re-ignition event, as is particularly evident in **Figure 47,** images (a-g)**.** The flame spreads out and fills the whole combustor, image

(e)—(h). However, the fuel/air ratio is apparently too low for the flame to remain stabilized in the entire combustor and the flame reverts back to tornado then columnar shape, image (j)—(l).

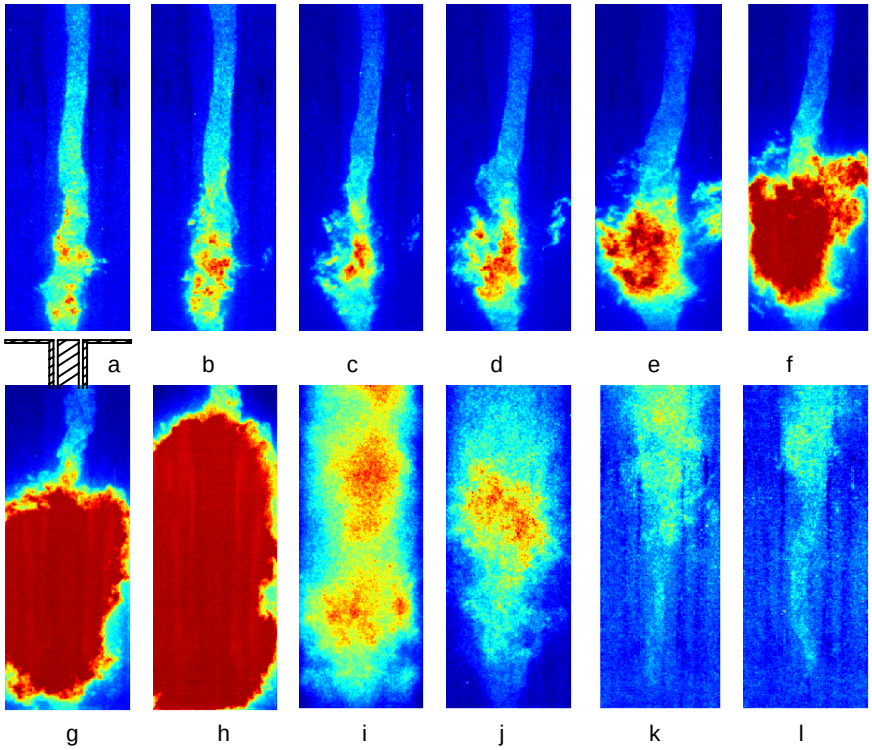

Figure 47: Consecutive images of 50%CH_4 --50% H_2 flame under near blowoff conditions (ϕ =0.35; images separation ≈10ms)

Further increases in the hydrogen content cause this columnar flame to more and more prominently dominate the flow physics. In fact, at very high H_2 levels, the flow prior to blowoff becomes much less unsteady than in the previously shown images, and consists simply of a nearly steady columnar flame (clearly, most of the reactants are exiting the combustor unburned in this situation), see **Figure 48**.

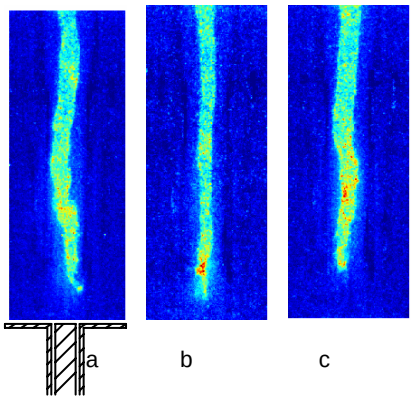

Figure 48: Consecutive images of 25%CH_4 --75% H_2 flame under near blowoff conditions (ϕ =0.31; images separation =10ms)

It is unclear what flow physics dominate the dynamics of this columnar tube. Near the nozzle exit, its size corresponds to that of the centerbody, so it is apparently associated with the shear layer and wake beyond the centerbody. However, if it were purely associated with the center body wake, it would not persist throughout the whole length of the combustor. Moreover, its presence appears sporadic, suggesting that this is a helical vortex associated with the swirling flow. The presence of this helical vortex must be altered by the local heat release rate (or gas expansion ratio) that causes its dynamics to vary with ratio of burned to unburned gas temperature.

5.3 PIV Measurements

High speed images show a variety of highly dynamic flame features, which vary substantially with the H_2 levels in the fuel. These features involve complex interactions between the inner recirculation zone (vortex breakdown bubble), outer recirculation zone of the rapid expansion, and flame extinction/reignition phenomenon. In addition, a

columnar flame shape was observed for high hydrogen flame. However, the relative role of fluid mechanics and kinetics in these dynamic features was unclear. Particle image velocimetry (PIV) measurements were performed to follow up on these observations and further characterize the flow field of these flames. The details of test conditions are shown in Table 4. Two groups of data were obtained with nozzle exit velocity of 29 m/s at room temperature and room pressure. The first group was taken at near blowoff conditions, see blue circle points in **Figure 40**, and the other group was obtained at constant adiabatic flame temperature of 1590K for four H_2/CH_4 mixtures, see red square points in **Figure 40**.

Table 4: Test conditions in PIV measurements

Fuel Composition (volumetric)		**Constant Temperature Test**		**Near Blowoff Tests**	
H_2	**CH_4**	**Φ**	**T_{ad} (K)**	**Φ**	**T_{ad} (K)**
0	100	0.56	1595	0.5	1480
20	80	0.55	1587	0.42	1329
50	50	0.54	1594	0.35	1201
75	25	0.52	1595	0.31	1141

Averaged Flow Field

In order to obtain a feel for the basic structure of the swirling flow with or without combustion, time averaged measurements of the cold flow and stable CH_4 flame are shown in **Figure 49** (b). Some velocity vectors were removed in areas with significant

number of spurious vectors at locations of window reflections. In addition, iso-vorticity lines are also indicated. The 2D vorticity was defined as,

$$\omega = \frac{\partial v}{\partial x} - \frac{\partial u}{\partial y} \qquad (1)$$

where x and y are the radial and axial coordinates, and u and v are the radial and axial velocities, respectively. For clarity, only high magnitude values, $|\omega|>4000\ s^{-1}$, are plotted. The uncertainty analysis is presented in appendix. In general, the velocity has maximum of 5% error, and vorticity has an uncertainty of $\pm$ 400 1/s.

The bottom boundary is the inlet plane of the combustor, and the centerline is the axis of the combustor. To compare the flow structures with and without combustions, half of each measurement volume is shown, with the nonreacting and reacting on the right and left sides, respectively. Each of the plots is the average of 128 images, sufficient for good convergence [82]. The inlet annulus is located between 10 and 14 mm radially.

In both the reacting and non-reacting flow situations, the same basic time averaged flow structure is observed, consisting of a corner recirculation zone (CRZ, due to the rapid expansion), inner recirculation zone (IRZ, due to the vortex breakdown bubble) and an annular jet. The annular jet flow is directed downstream and somewhat outward and separates the IRZ and CRZ. The IRZ and CRZ locations were quantified by the locus of points with zero vertical velocity. Note that the IRZ is merged with the small separation zone downstream of the centerbody [81]. These three flow regimes are separated by two layers of strong, oppositely signed shear, as can be seen from the overlaid vorticity iso-contours.

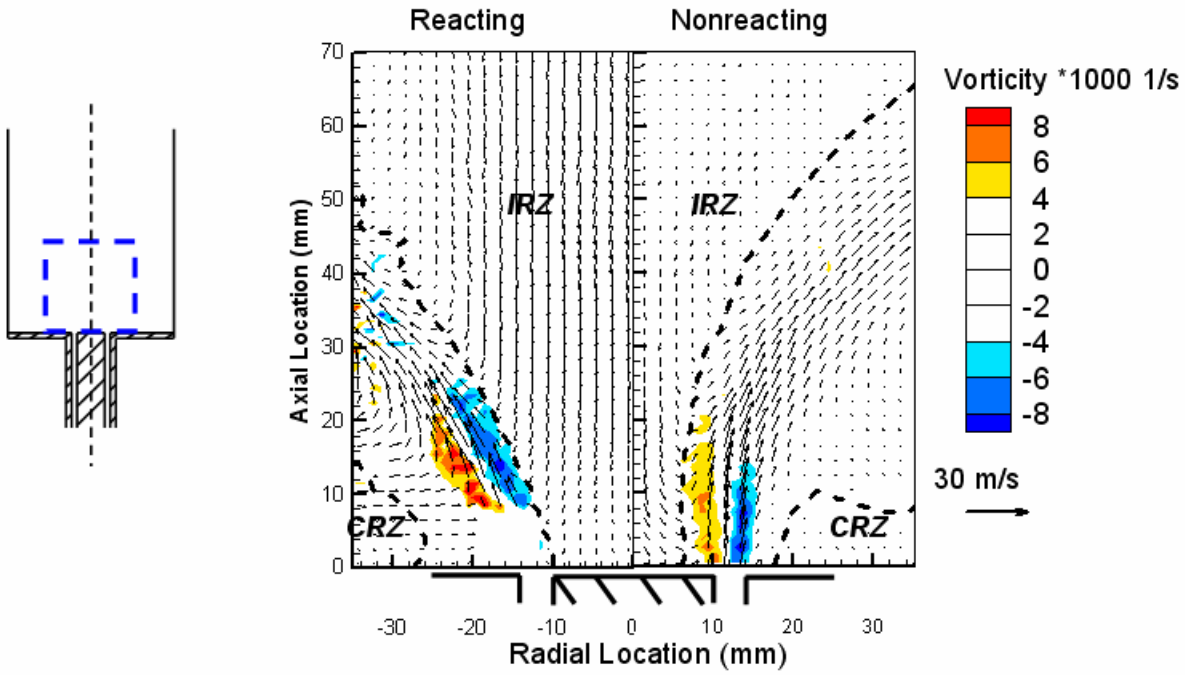

(a) (b)

Figure 49: PIV window arrangement (a) and averaged flow fields (b) of non-reacting flow (right) and reacting flow (stable methane flame, left)

Although these three basic flow features are common to the nonreacting and reacting flows, their quantitative characteristics/locations vary significantly. The recirculation zones have much stronger velocity fields in the reacting case, and the IRZ zone is much wider. Therefore, the two shear layers are stronger, as manifested by the larger vorticity magnitudes. In addition, the annular jet region is somewhat narrower in the reacting case. These observations are consistent with others in these types of flows [82].

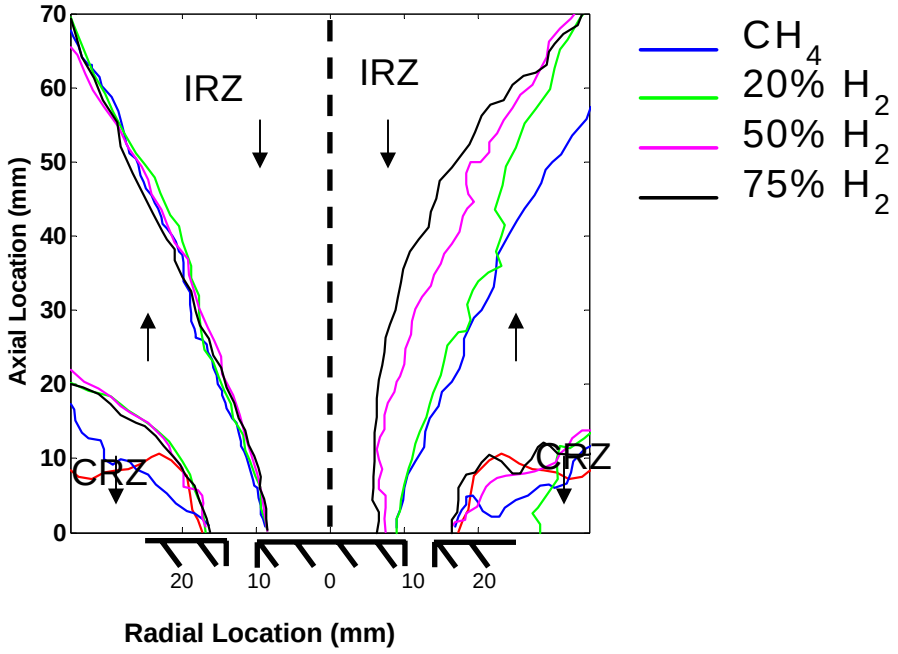

Figure 50: Contour lines of zero mean axial velocity for flames at the same adiabatic flame temperature (left half) and near blowoff (right half).

An important question relates to the relative roles of fluid mechanics and chemical kinetics in causing the above described variation in near blowoff phenomenology (high speed images). Fluid mechanics must certainly exert some role, as the average gas expansion ratio monotonically decreases as the H_2 levels increase, due to the lower flame temperatures these mixtures can sustain. In order to better understand the relative role of chemical kinetics and fluid mechanics in this system, a set of data were obtained where the relative H_2/CH_4 mole fractions were varied, but by adjusting the overall mixture stoichiometry such that the gas expansion ratio across the flame and adiabatic flame temperature (calculated) remained nearly constant at 1590K. Details of the

stoichiometries and test conditions are shown in the Table 4. Results illustrating the time averaged location of the IRZ and CRZ boundaries are shown in the left half of **Figure 50,** which plots these zero axial velocity for cold flow and different H_2/CH_4 flames. Each line was the averaged result of 128 images. Four cases are plotted corresponding to flames operated at nearly constant adiabatic flame temperature 1595 K (calculated), which correspond to equivalence ratio variations from 0.56 to 0.52. Note that all these flames are well removed from blowoff. A narrower average IRZ boundary would be found for the cold flow case (not shown), consistent with other observations [82].

These results show that all four reacting cases have essentially identical IRZ boundaries, regardless of the fuel H_2/CH_4 ratio. This result suggests that kinetic effects do not impact the average flow field structure– rather, that it is mainly determined by the thermal expansion due to the flame. For example, **Figure 49** and **Figure 50** show that all stable flames have a similar flow structure, which is distinctly different with the cold flow case. However, although the flow structure is mainly determined by thermal expansion, it is not totally controlled by the thermal expansion ratio. Another set of data were obtained where both the relative H_2/CH_4 mole fractions and adiabatic flame temperatures were varied (Test conditions were indicated by blue points in **Figure 58**). Because the flames with higher hydrogen levels become unsteady at lower fuel/air ratio's and flame temperatures, the thermal expansion ratio across the flame is different for the these flames. Although the flame temperatures are so different, 1250-1750K, the flow structures are also nearly identical. This result suggests that flow structure is not very sensitive to the thermal expansion ratio. The flame shows a strongly dynamic behavior when blowoff is approached, and for completeness we plot the corresponding flow

boundaries for the near blowoff cases in the right half of **Figure 50.** This figure shows that the size of the IRZ reduces as the percentage of H_2 increases, apparently corresponding to the dynamic behavior, which is a function of the hydrogen level. *As such, the fluid mechanic structure of the flow for the near blowoff flames considered in more detail below certainly varies with the fuel composition, and affected by both kinetic effects and fluid mechnics.*

Instantaneous Flow Field

A group of typical raw Mie scattering images are shown in **Figure 51.** As discussed in our previous section, a flame near blowoff tends to exhibit substantial dynamics, including apparent extinction-ignition behavior. Unfortunately, it is difficult to discern the reaction zone location during these events because of local "holes" in the flame sheet and a highly disorganized field of reactant/product interfaces – in cases where the flame sheet is largely continuous, its location can be easily determined by simultaneous analysis of the seed density and its gradient. The latter situation is the case at points where the flame is stabilized on the centerbody or downstream, such as shown in **Figure 51 (a).** However, the flame bounces between these two states for the majority of the time near blowoff (around 90% of the raw images for the low H_2 cases), and it is quite difficult to mark the reaction zone, see **Figure 51 (b,c,d)**. In such a phase, the flame surface has holes which cause the cold reactants to mix with the hot products. In the subsequent discussion, we focus on images where the flame front can be tracked along with the flow field. It should be recognized that this necessarily excludes the majority of images. It does, however, allow us to understand the two flame states that the

system is oscillating between, which are separated by rather chaotic periods of disorganized product/reactant interfaces.

Figure 52 shows four typical instantaneous velocity fields for a CH_4 flame at equivalence ratio of 0.5, which is near blowoff. The solid black line represents the flame front near the nozzle exit, which is determined from the steep gradient in seed density. This approach for discerning the flame position only works well in the near nozzle region, however, and it is more difficult to discern the flame edge farther downstream. As such, although the lines indicating the flame front stop at some downstream/radial location, the flame persists farther beyond it. Many of the basic flow features described above are still discernable from these images. The annular jet extends downstream and radially outward, whose edges are demarcated by the regions of high shear and vorticity. At the center of the combustor, a strong backflow indicates the IRZ, and the CRZ is evident in the two corners. However, a number of fine scale vortex flow features are observed in these images which are averaged out in the images shown above. In particular, the jet and shear layers are distorted greatly by the small vortices (same order of the radius of the centerbody). In two of the images (a) and (d), the flame is attached to the centerbody, similar to prior observations [82]. The flame is stabilized in this high shear region and extends radially outward along the high shear, inner edge of the annular jet. Higher vorticity levels are observed instantaneously than on average; e.g., the instantaneous vorticity in the shear layers is around 16,000 s^{-1}, while it is 8,000 s^{-1} in the averaged field, see **Figure 49**.

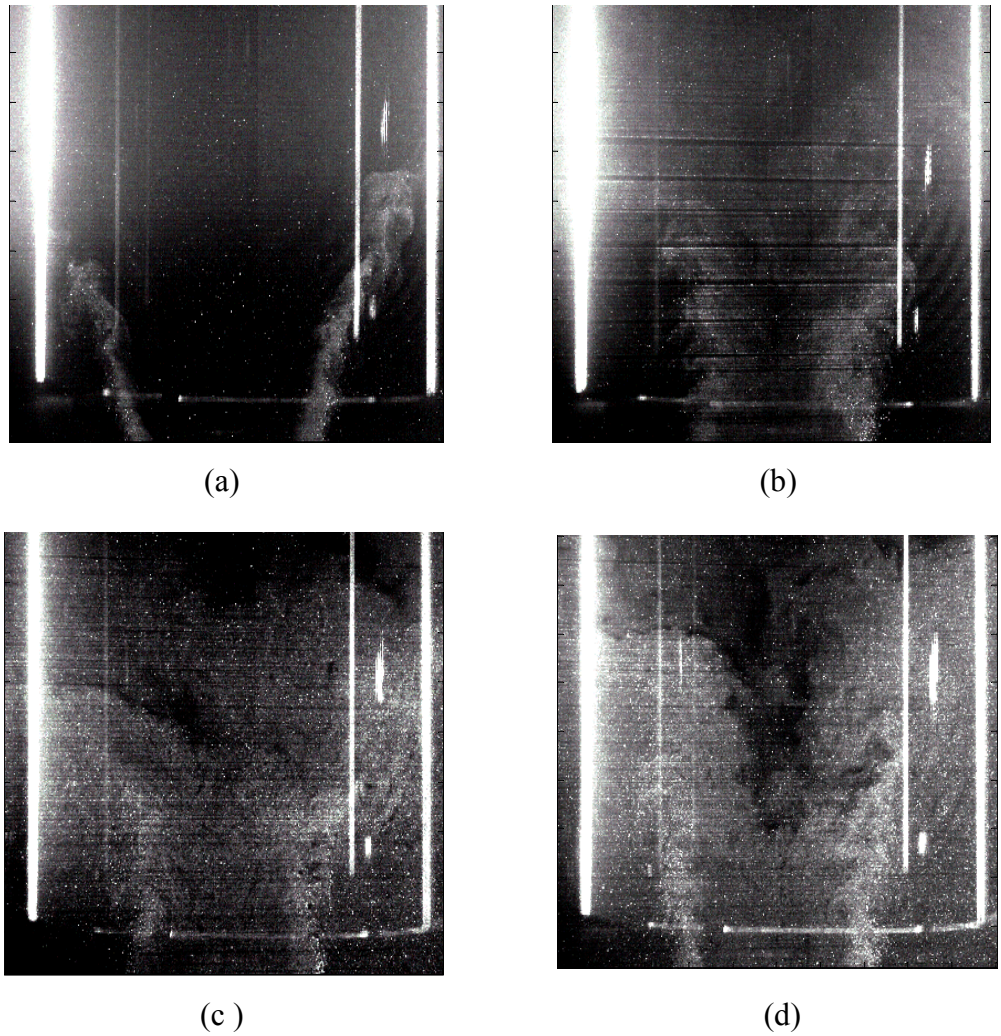

Figure 51: Typical raw PIV Mie scattering images for CH_4 flame near blowoff.

In two of the images, (b) and (c), the flame is not attached to the centerbody and is situated downstream. Presumably, it is kept from blowing off by the recirculating flow in the IRZ. The centerbody wake flow is substantially altered in these two cases, as a much longer wake is evident. In contrast, when the flame is attached to the centerbody, the strong thermal expansion induced flow across the flame renders this wake region nearly unrecognizable. The CRZ region has multiple fine vortices. For example a pair of vortices, which have opposite senses, occupy the corner region, see the right corner of

Figure 52 **(c).** The sense of the rotation of the bottom vortex is counter-clockwise, which is opposite with the direction of high speed jet. It shows that the instantaneous fine vortices have different or even opposite properties than the averaged main flow structure. The bottom of the flame is inside the IRZ, and extends radially outward. In both images, however, the flame is clearly located downstream and inside the inner shear layer. This suggests that this image is only a snapshot of a dynamic phenomenon where the whole flame is for a few instances being blown downstream. Unfortunately, the sampling rate of the PIV system is not high enough to capture multiple images of a single one of these events.

Notice also that the flame front is substantially more corrugated in these instances when it is located downstream, due to wrinkling from the fine scale vortices alluded to above. These vortices may be associated with a helical vortex tube that spirals downstream, see red circular arrows in **Figure** 52 (b, c). Interestingly, these same vortices are not evident in images (a) and (d), where the flame is attached to the centerbody, **Figure** 52 (a, d). This suggests a complete restructuring of the dynamic flow field due to thermal expansion effects and fundamentally different flow features when the flame is and is not attached to the centerbody.

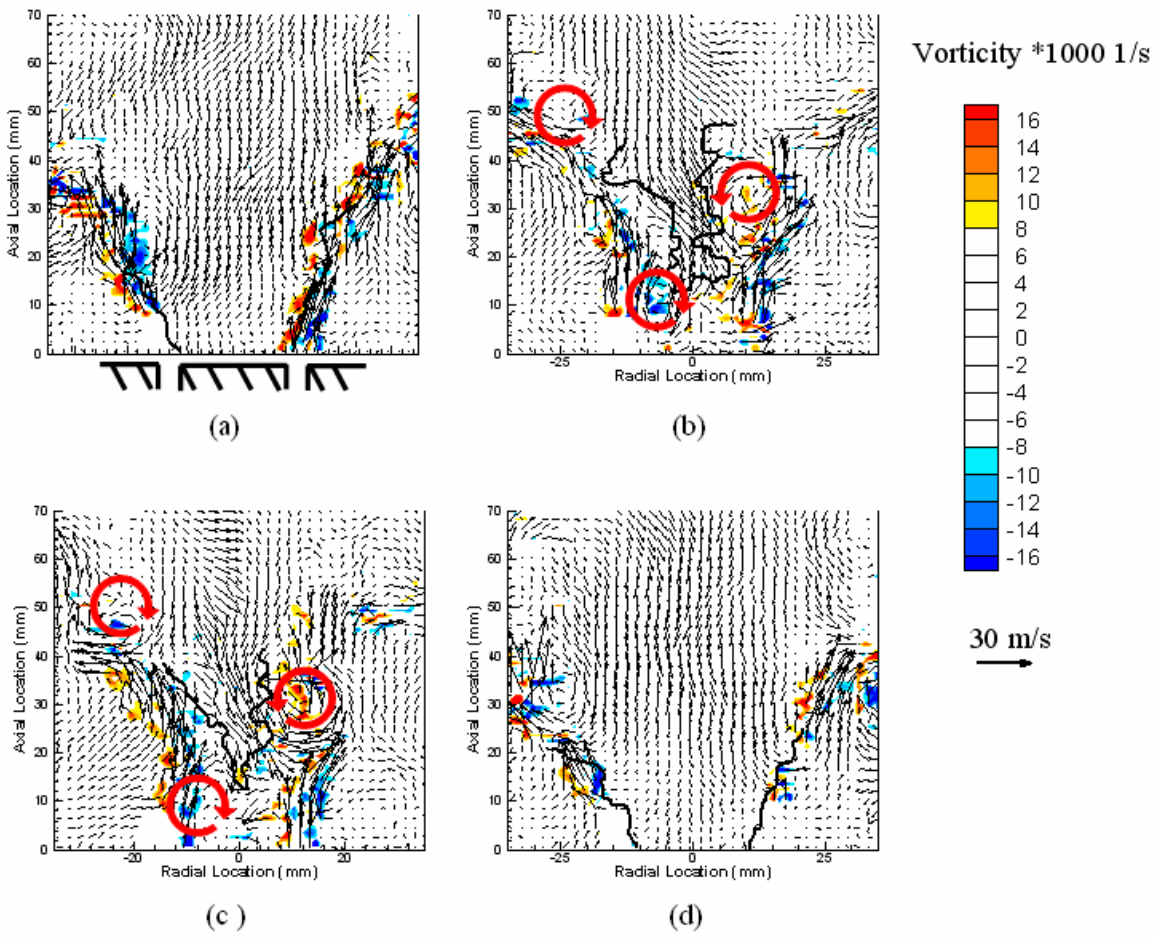

Figure 52: Instantaneous flow field and flame front for CH_4 flame near blowoff.

The previous section has consistently showed that near blowoff flames are quite unsteady and oscillate between "extinction" and "re-ignition" phases near blowoff. These images depict one of these unsteady phases, and show that, at least in this case, they are associated with an oscillation between two stabilization points, separated by local-extinction/reignition and product/reactant mixing. Presumably, the local strain rate at the flame attachment point becomes too high and the flame locally extinguishes, causing it to blow downstream. During this process, reactants can penetrate the wake

region, causing substantial product-reactant mixing and making the reaction zone region unintelligible.

Farther downstream, the two flame branches merge and, after some transient, the flow is again divided into regions of only high and low seed density – making it possible to determine flame location. This flame then moves back upstream. Notice that the velocity vectors in these cases are pointing upstream, showing that the flame is moving upstream. Interestingly, we have almost no images where the post flame velocity field is moving downstream. This shows that during these instances of downstream movement, substantial product-reactant mixing is present and the reaction location is not discernable. Figure 53 shows the four typical instantaneous velocity fields for a near blowoff flame, consisting of 50%CH_4 /50% H_2 at an equivalence ratio of 0.35. Note that this corresponds to a lower flame temperature than the pure methane result. A similar flow structure and dynamical sequence of events is observed in **Figure** 53 as in **Figure** 52. The flame is also stabilized in the inner shear layer, when the flame is attached to the centerbody, see **Figure** 53 **(a,d)** and by the recirculating flow when it is lifted off, see **Figure** 53 **(b,c).**

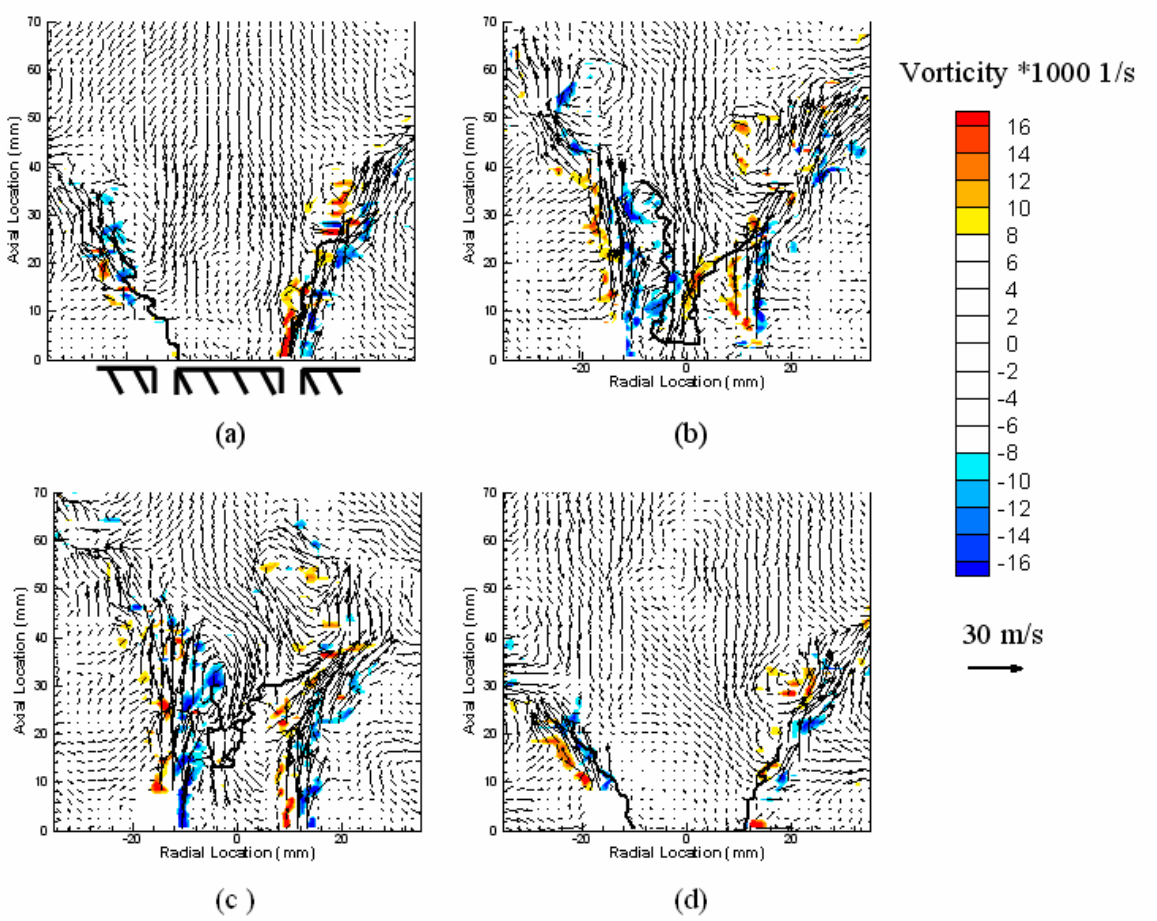

Figure 53: Instantaneous flow field and flame front for 50%CH_4 /50% H_2 flame near blowoff.

Higher hydrogen level flames near blowoff exhibit different dynamics because they never are stabilized on the inner centerbody shear layer, but only downstream. Furthermore, the flame exhibits a thin, columnar shape, evident in some cases in the 50%/50% case. Further increases in the hydrogen content cause this columnar flame to more and more prominently dominate the flow physics. In fact, at very high H_2 levels, the flow prior to blowoff becomes much less unstable, and consists simply of a nearly steady columnar flame (clearly, most of the reactants are exiting the combustor unburned in this situation). This is associated with a substantially higher percentage of the images

having clear seed density interfaces corresponding to the flame – roughly 50%. Although these images closely resemble those shown above in cases where the flame is downstream, this point should be kept in mind as the more typical, larger number of events are not shown. **Figure** 54 shows four typical results for 25%CH_4 /75% H_2 flame at an equivalence ratio of 0.31, which is close to the blowoff limit. A columnar flame is not obvious in this plot due to only a small part of the flame is plotted; however, it is very obvious from direct visualization. A columnar flame stabilized near the nozzle and extends to the exit of the combustor.

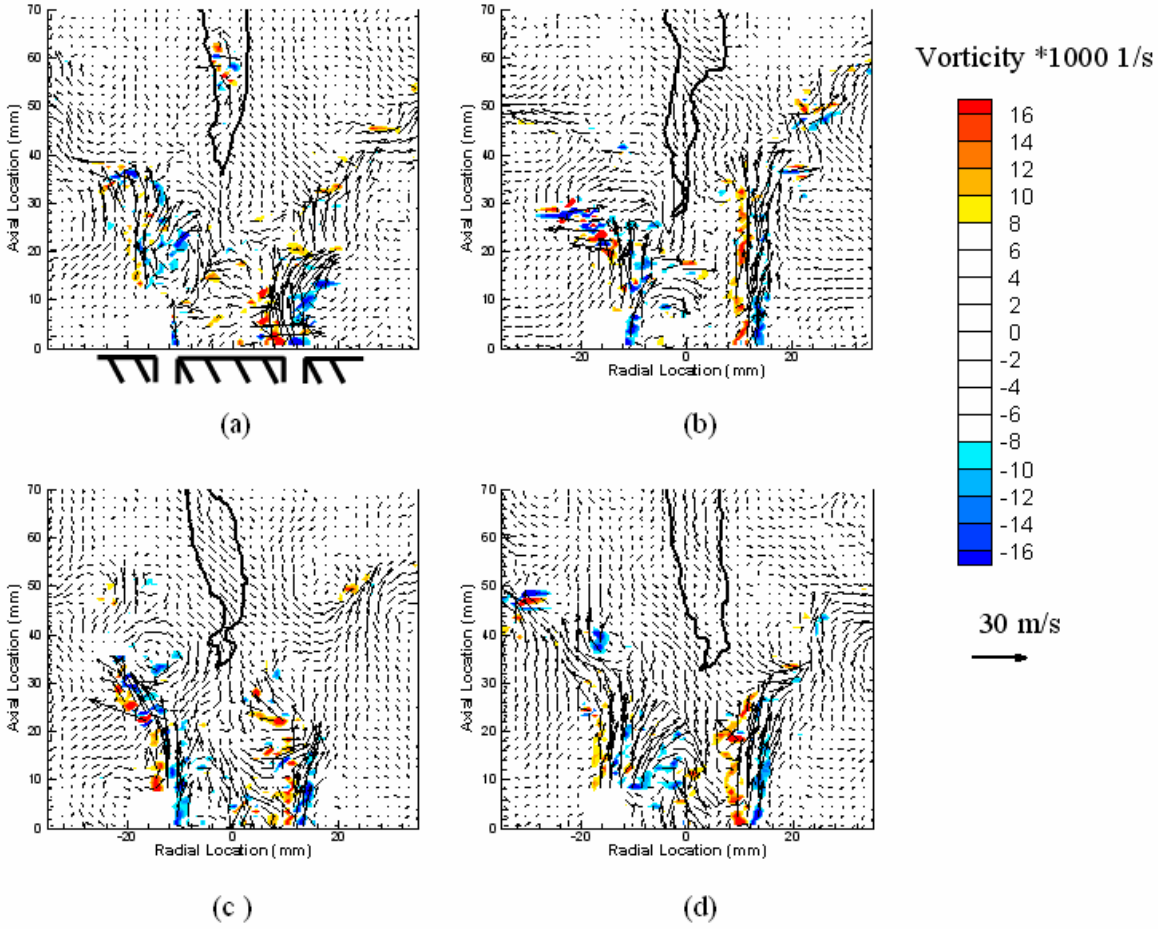

Figure 54: Instantaneous velocity field and flame front for 25%CH_4 /75% H_2 flame near blowoff.

This PIV image shows many of the same basic features as described in the earlier cases. There are some hot products between the bottom of the flame and the centerbody, which are determined by low seed density regions, see red circles in **Figure 55**. Normally, the hot products exist as small, unconnected wrinkled regions. Analysis of the seed density gradient suggests that these interfaces are not flame fronts.

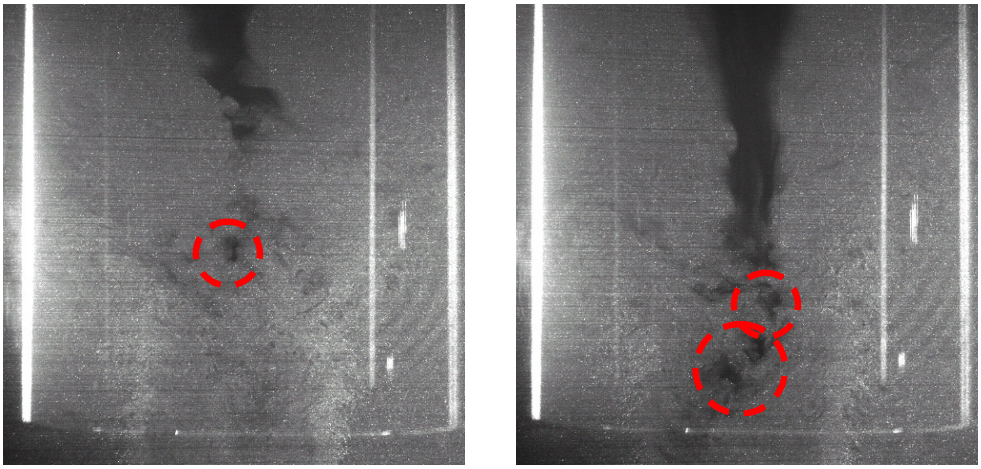

(a) (b)

Figure 55: Raw Mie scattering images in PIV measurements for 25%CH_4 /75% H_2 flame near blowoff.

5.4 Fluid Mechanics and Chemical Kinetics

An important question relates to the relative roles of fluid mechanics and chemical kinetics in causing the above described variation in near blowoff phenomenology. Fluid mechanics certainly exert some role as the gas expansion due to the flame changes the recirculation flow structure, see **Figure 49** and **Figure 50**. This gas expansion and corresponding flow velocity must cause some variations in the fluid mechanics of the flow.

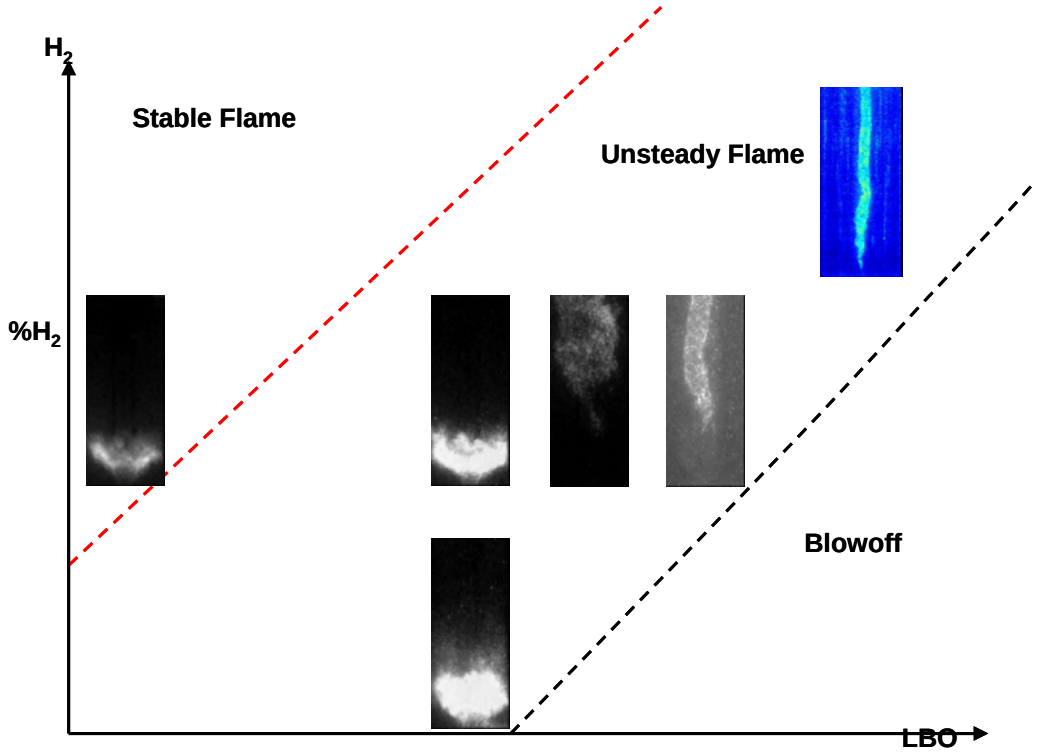

Figure 56: Diagram of flame dynamics near blowoff

Figure 56 summarizes these blowoff dynamics for different H_2/CH_4 mixtures. X-axis is related to equivalence ratio. For a given fuel composition, as we move horizontally from left to right the chart by reducing flame temperature (or fuel/air ratio), at some point a certain level of "enhanced unsteadiness" becomes evident, indicated by the dashed red line. Further reductions in flame temperature or equivalence ratio cause blowoff, indicated by the black line. Three rows of images are presented. The images of middle row are from 50%-50% H_2/CH_4 flames. The flame moves from stable flame into the 'unsteady' region as the flame temperature decreases. In this region, the flame experiences the processes described in **Figure 42**, **Figure 43**, and **Figure 47**, and finally blows off. For the bottom row, which is from pure methane, blows off at a higher flame

temperature, so it does not have the chance to go through dynamics described in **Figure 43** and **Figure 47**. At higher levels of H_2, an additional flame dynamics, associated with a columnar flame zone is also present. **Figure 56** shows that all the flames blow off in somewhat the same series of flame dynamics, such as **Figure 42**, **Figure 43**, **Figure 47**, and **Figure 48**, provided that their blowoff temperatures are low enough (obviously, methane flame does not in this study). However, the blowoff boundary (how far the flame can go) mainly depends on the chemical kinetics phenomenon.

The kinetics phenomenon controlling these blowoff boundaries are also functions of boundary conditions. For example, it is known that pure methane can also experience columnar flame shapes (referred to as tornado flame) [53]. For example, Muruganandam observed tornado flame shapes for swirling methane flames by changing the length of his combustor. However, it should be pointed out that at *the same boundary conditions*, the blowoff phenomenology is a function of the H_2 levels in the fuel.

Kinetics, particularly strain sensitivities, certainly exerts a role on the dynamic oscillation between the attached and unattached flames shown for the lower hydrogen level flames. These flames were never observed to persist downstream in the steady state, as was observed with higher hydrogen flames. In contrast, high H_2 flames under very near blowoff conditions are never observed to attach to the centerbody, suggesting that the local strain rate exceeds the extinction value. However, the flame can exist downstream. For example, many PIV images clearly show the flame interface right at the boundaries of high vorticity regions (this could also reflect the reduction in vorticity across the flame, however).

Local flame extinction, which finally leads to blowoff, is sensitive to strain induced by flame curvature and flow non-uniformity. It is well known that H_2 addition substantially increases the extinction strain rate of CH_4 flames. The situation is more complex when comparing near blowoff flames because the flame temperature and stoichiometry monotonically decreases with increasing H_2 levels.

CHAPTER 6

STRAIN CHARACTERISTICS NEAR THE FLAME ATTACHMENT POINT

This chapter presents flow field measurements obtained in the same swirl combustor as in Chapter 5, see **Figure 7**. Its objective is to obtain quantitative measurements of the flame characteristics under stable and unsteady flame conditions near the flame stabilization point. These data supplement the more qualitative data obtained in prior chapters by providing a detailed view of the flame processes.

Some review of the flame and flow structure is helpful. As shown in previous chapter, the basic flow structure consists of a corner recirculation zone (CRZ), which is a toroidal recirculating regime generated by the rapid expansion of the nozzle into the combustor, an inner recirculation zone (IRZ), due to vortex breakdown accompanying the swirling flow and a high velocity, annular fluid jet that divides these regions. The flame itself can be spatially distributed in four basic configurations, depending upon fuel/air ratio and flow velocities, see **Figure 57**. As shown, it can be stabilized in the shear region at the inner centerbody or outer centerbody or downstream by the vortex breakdown bubble.

The specific focus of this chapter is to present quantitative studies of the flow field in the vicinity of the attachment point, especially the processes influencing flame stabilization on the inner centerbody, shown in **Figure 57** (c) and (d), a very common mode of stabilization in practice. Because of the centerbody, there is a low velocity region in the separating shear layer where the flame can stabilize. However, it is known that shear introduces aerodynamic straining on the flame [16], which alters the local

temperature and burning rate [14]. If the flame strain rate is too large, the flame will locally extinguish and either blow out of the combustor completely, or stabilize at another location, such as transitioning from configuration (c) to (b) or from configuration (d) to (a). As such, characterization of the local strain rate magnitudes of the flame in the attachment point regions is needed in order to understand these factors influencing flame location.

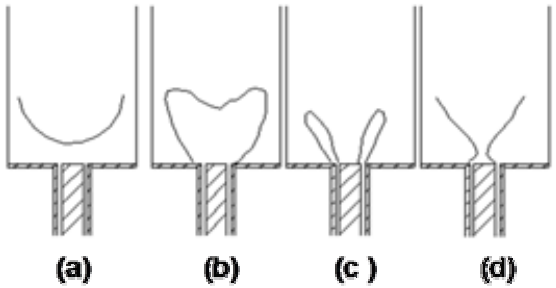

Figure 57: Basic flame structures in swirling flows

6.1 Test Conditions and Blowoff Limits

All the flow field measurements were obtained at a constant nozzle exit velocity of 33 m/s. Tests were performed at combustor pressure of 1.0 atm and 300 K reactants. The blowoff limit for this combustor under such conditions is indicated by the solid black line in **Figure 58**. However, the flame becomes unsteady and exhibits transient behaviors as described in chapter 5 before blowoff. The stable/unsteady boundary is indicated by the dashed blue line in **Figure 58**. This boundary was determined from the OH chemiluminescence measurements. An optical fiber was used to collect the chemiluminescence signal from the flame. Equivalence ratio was decreased in steps of

0.01 from a stable flame, and at each equivalence ratio, 30 seconds of OH chemiluminescence signal was taken and processed to determine the number of extinction/reignition events per second. This unsteady flame boundary is defined as the points where extinction/reignition events occur at least once per second. To understand the sensitivity of this boundary to equivalence ratio, see **Figure 39** in chapter 5. For unsteady flames, the near-attachment point region starts to become unsteady and exhibit local extinction events, manifested as "holes" in the flame sheet. PIV measurements points in this area are indicated by the square red points in **Figure 58**. Data were also taken in stable flame region, at stoichiometries close to, but sufficiently removed from the stable/unsteady boundary (circle blue points in **Figure 58**). The details of PIV test conditions are shown in **Table 5**. It was found that all these mixtures cross the unsteady/stable boundary at a nearly constant extinction strain rate, see Figure 59. Extinction strain rates were calculated by COSILAB 2.0 with GRI 3.0 mechanism. Figure 59 shows that the extinction strain rates for H_2/CH_4 flames are all around 800 1/s at the unsteady/stable boundary. A Damköhler number can be defined as

$$Da_{ext} = \frac{\kappa_{ext}}{U_{ref}/l_{ref}} \quad (45)$$

where κ_{ext} represents the extinction strain rate. Since all the tests were performed under same conditions, the U_{ref} and l_{ref} are probably similar for these different mixtures. This result suggests that the H_2/CH_4 mixtures cross the unsteady/stable limit at a nearly constant Damköhler number.

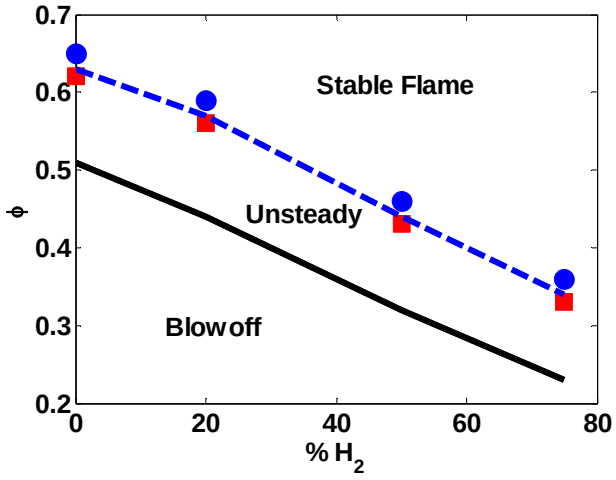

Figure 58: Dependence of blowoff limits upon percentage of Hydrogen. Stable flame test points indicated by blue circles, unsteady flame test points indicated by red squares.

Table 5: Test conditions in PIV measurements

Fuel Composition (volumetric)		**Stable Flame**		**Unsteady Flame**	
H_2	**CH_4**	***Φ***	***T_{ad}* (K)**	***Φ***	***T_{ad}* (K)**
0	100	0.65	1759	0.62	1705
20	80	0.59	1662	0.56	1606
50	50	0.46	1435	0.43	1373
75	25	0.36	1256	0.33	1188

Figure 58 shows that the lean blowoff occurs in at least two phases (or limits). The first is the stable/unsteady limit. The second was an actual blowoff event. The first limit was associated with flame strain level, which exceeds the extinction strain rate, leading to

local extinction or flame "holes". Flames are very unsteady after passing the first limit, and have a variety of highly dynamic flame features as shown in Chapter 5. Finally, the flame reaches the second limit, and blows off.

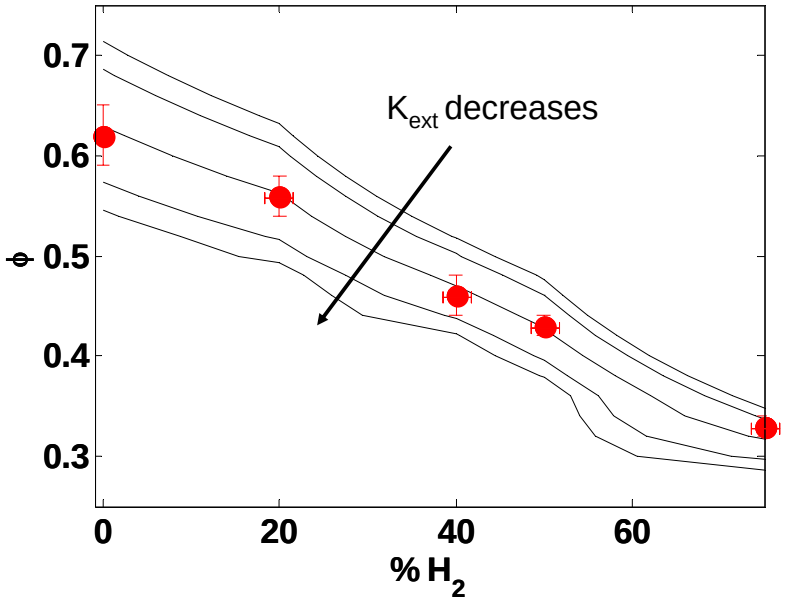

Figure 59: Dependence of κ_{ext} upon percentage of hydrogen and equivalence ratio. Contour lines are valued at 1400, 1200, 800, 400 and 200 1/s. The test points for unsteady flames are indicated by red circles. These contours were estimated by calculation of κ_{ext} at 0/100, 20/80, 40/60, 50/50, and 75/25% H_2/CH_4 mixtures with equivalence ratio steps of 0.02. (Note that the data points at 200 1/s were extrapolated from higher equivalence ratios)

Although the *Da* correlation in chapter 4 could correlate and predict the lean blowout limits (the second limit) very well, it probably does not include the physics associated with the actual blowoff process. The complex interactions between vortex breakdown, the rapid expansion, and flame extinction/reignition phenomenon, which are shown to be very important to lean blowoff in chapter 5, are not considered in the correlation at all. The *Da* correlation in chapter 4 probably just describes the first phase of blowoff, the

unsteady/stable boundary. **Figure 58** shows that these two limits are correlated: the lines represent these two limits are almost parallel with each other.

6.2 Flame Front and Flame Holes Detection

The locations of flame front and flame holes along the flame are critical for this work. So a short description of the method used to detect flame front and flame holes is given below.

Mie scattering diagnostics were used to visualize the thermal boundary (flame front) between product and reactants. As long as the flame is sufficiently removed from blowoff, the raw image has two regions of high and low particle density regions, which indicate the cold reactants and hot products, respectively, see Figure 60 (a). However, the raw image is often blurred by reflections, and particle density gradient along the boundary is not distinctly higher than other areas. A series of Matlab based filters were used to enhance the quality of these images. The raw PIV image is converted into binary image first, Figure 60 (b). The raw image is in gray scale, and each pixel has an intensity value in the range of 0-255. A threshold value 150 for the pixel intensity is used for this binary filter. Second, a two dimensional median filter was used to this image, see Figure 60 (c). In Matlab IPT (Image Processing Toolbox), median filter is designed to remove "salt and pepper" noise associated with PIV images, which contain many isolated spots. Last, the image was processed with a Laplacian filter, Figure 60 (d). Specifically, a 3 by

3 mask with the center value of -8 was defined as $\begin{bmatrix} 1,1,1 \\ 1,-8,1 \\ 1,1,1 \end{bmatrix}$. So $\nabla^2 f(x,y)$ in this filter is defined by

$$\nabla^2 f(x,y) = [f(x-1,y+1) + f(x-1,y) + f(x-1,y-1) + f(x,y+1) + f(x,y-1) + f(x+1,y+1) + f(x+1,y) + f(x+1,y-1)] - 8f(x,y) \quad (46)$$

Enhancement using the Laplacian filter is based on the equation

$$g(x,y) = f(x,y) + c[\nabla^2 f(x,y)] \quad (47)$$

where *f(x,y)* is the input image, *g(x,y)* is the enhanced image, and c is a function of the mask value. The Laplacian filter sharpens the image, so that the boundary between high and low density regions is much easier to be detected.

The image enhanced by these three filters (binary, median, Laplacian) can be processed with the standard function, *edge,* from IPT of Matlab for the flame fronts. In this code, a 10 by 10 Gaussian filter is defined, and a 40% of the maximum of gradient was used as the threshold to determine the boundary. Since particles are represented by those bright spots in images, the flame sheet or thermal boundary is extracted from the gradient of particle densities, see Figure 61.

Each pixel in those images is 0.03 by 0.03mm, which is the spatial resolution of the PIV camera. In the edge tracking algorithms, the largest filter is the Gaussian filter, which is 10 by 10 pixels (0.3 by 0.3 mm). It should be emphasized that all the features of the flame front less than the scale of 0.3 mm were removed.

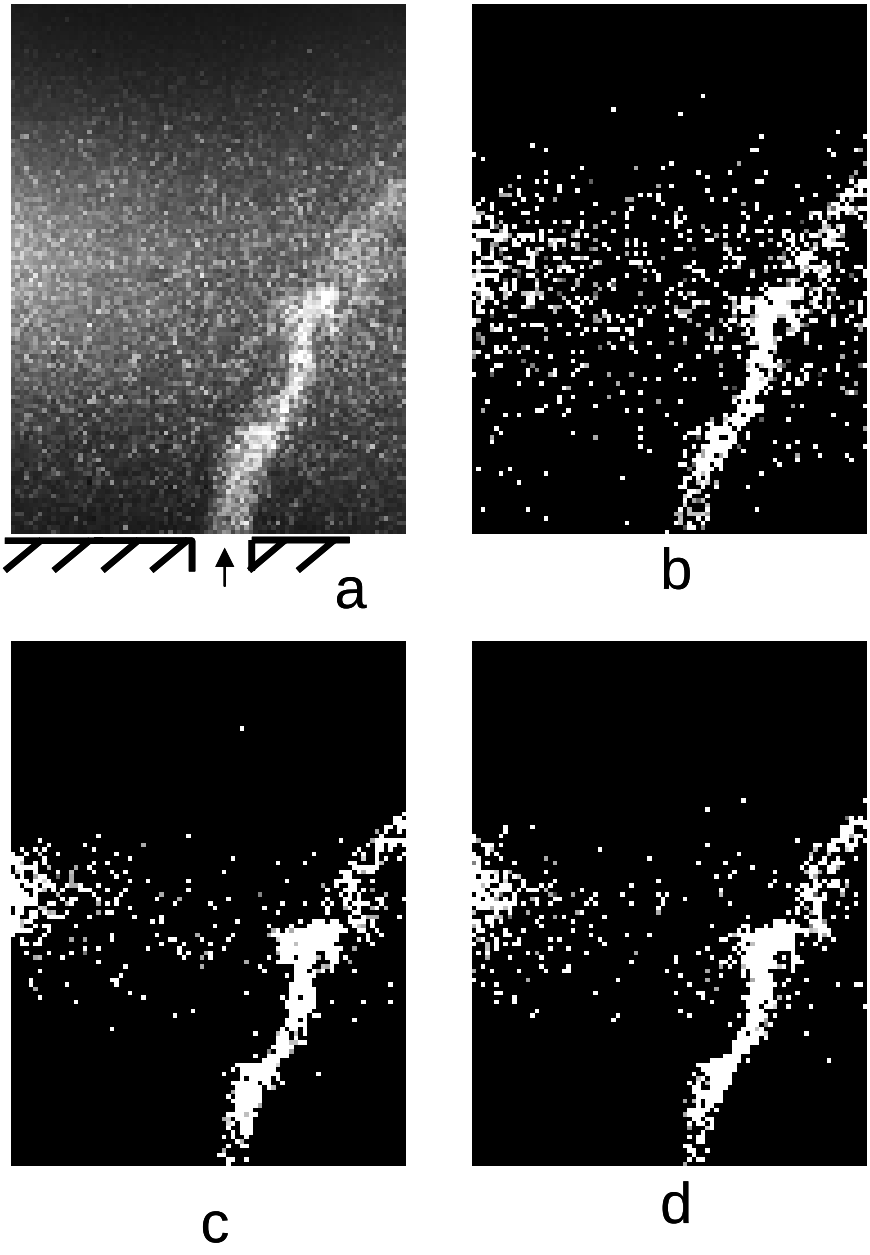

Figure 60: PIV image processing (a): Raw PIV image; (b): Results of binary filtering; (c): Results of median filtering; (d): Image enhanced using the Laplacian filter with -8 in the center

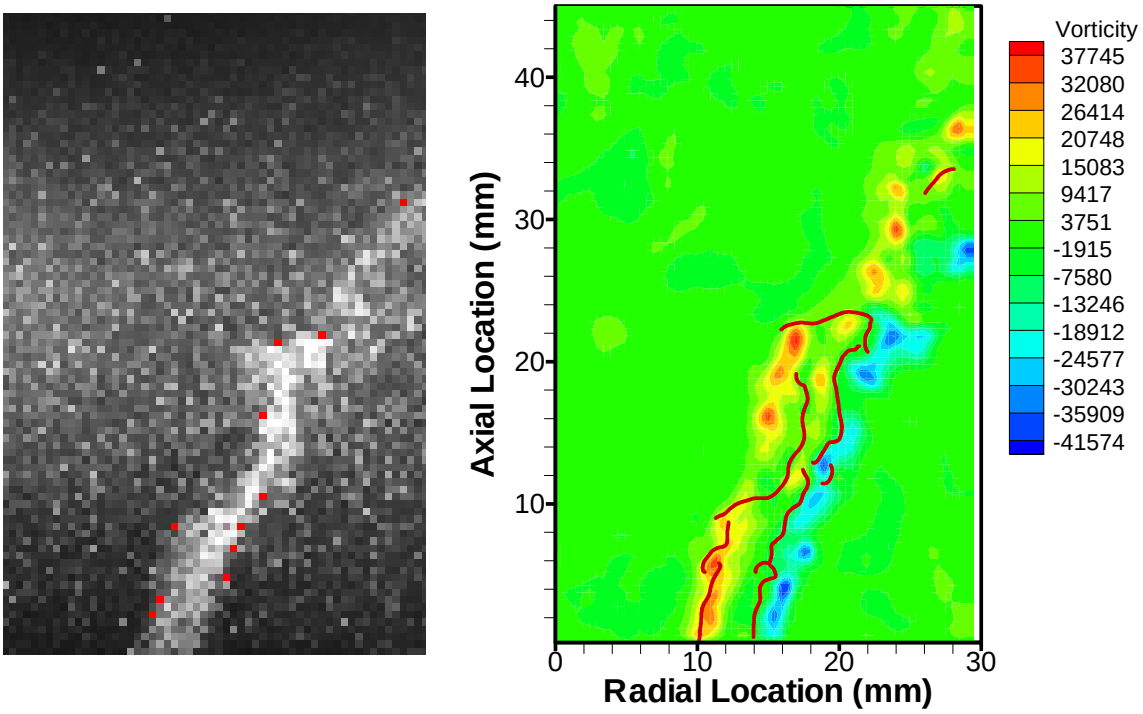

Figure 61: Flame front in raw PIV images (Left); Instantaneous iso-vorticity field and flame front (Right)

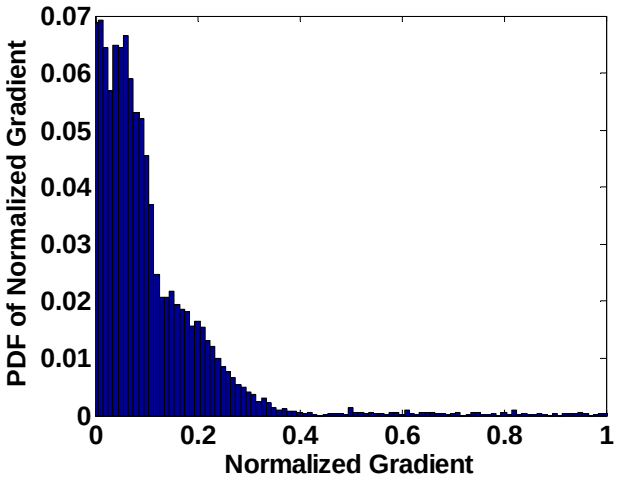

Figure 62: Probability density distribution of pixel intensity gradients of an image for a stable flame

The threshold level (40%) is selected by examining the probability density function (PDF) of the intensity gradients of a stable flame image. In this work, each image has 1600 by 1200 pixels. Intensity gradient is calculated at each pixel, and then normalized by the maximum gradient. A typical PDF of the normalized intensity gradients of an image (1600 by 1200 pixels) is shown in Figure 62. Since the particle density (pixel intensity here) changes greatly across the flame, pixels with high intensity gradients are connected as the flame front. Away from the flame front, either reactants area or products area, the intensity gradients are very small (0-35% of the maximum), see Figure 62. Obviously, the definition of flame front is sensitive to the gradient threshold. For example, if the threshold level is very high, say 90% of the maximum, there will be fewer pixels, which are considered to be the flame front. So in this work, based on the considerations of the gradient PDF, 40% of the maximum gradient was selected as the threshold for all the images, stable and unsteady flames.

For unsteady flames, the near-attachment point region starts to become unsteady and exhibit local extinction events, or "holes" in the flame sheet, see Figure 61. Those holes locations are defined as the downstream edge of the broken part where the gradient of particle densities falls below the threshold (40% of the maximum gradient).

It is clear that the flame holes greatly depend on the threshold used by the algorithm, see Figure 63. It shows the flame fronts under four different thresholds for an unsteady flame. With 40% threshold, Figure 63 (a), the flame attaches to the centerbody, and propagates downstream outwardly, and a couple of holes are presented along the flame. However, if the threshold used for holes detection changes, the size and numbers of flame holes also change. For example, 45% is used as the threshold in Figure 63 (b).

The flame front is broken near the centerbody, which is indicated by the blue circle. As the threshold is increased, see Figure 63 (c) and (d), the region of continuous flame front shrinks. In Figure 63 (c), two flame holes are getting larger and finally merge each other, see black circle. In Figure 63 (d), there is no flame front at all near the center body. However, for stable flames, if threshold level is less than 40%, flame holes never show on the flame fronts near the attachment points (axial location is less than 20 mm), see **Figure 67**.

For most of the flame, if the threshold is increased, the flame near the centerbody will be removed first, as shown in Figure 63. It indicates that the gradient of particle density near the centerbody is smaller than that of downstream flames. The discussion later in this chapter shows that the flame is compressed near the centerbody and stretched downstream, which results in a thick flame near the centerbody and a thin flame downstream. This may explain the systematic gradient change along the flame.

The mean flame front is determined by averaging multi instantaneous flame fronts at each axial location. However, for unsteady flames, which have holes along the flame fronts, the averaging method is slightly different. At each axial location, flames with holes at this axial location will not be counted. For example, Figure 64 shows the averaged flame front for an unsteady methane flame. A total of 30 instantaneous flame fronts were use. However, at each axial location, only those flame fronts which have uninterrupted flames at this axial location, were averaged for the mean flame front. In Figure 64, the mean flame is represented by the solid black line (only one flame branch which is attached to the centerbody, is shown). A third order polynomial curve fitting was performed to smooth the flame front.

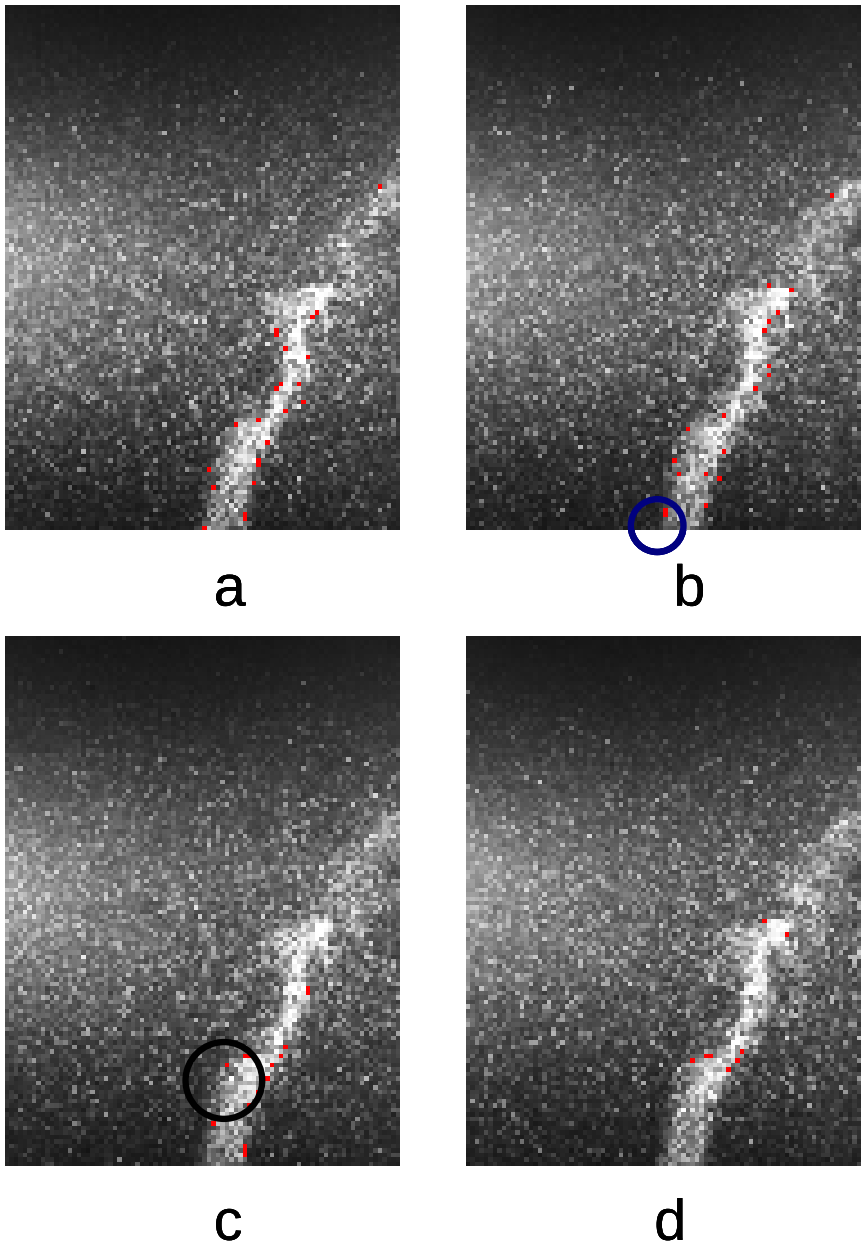

Figure 63: Flame fronts determined by *edge* with threshold of (a) 40%, (b) 45%, (c) 50% and (d) 60%

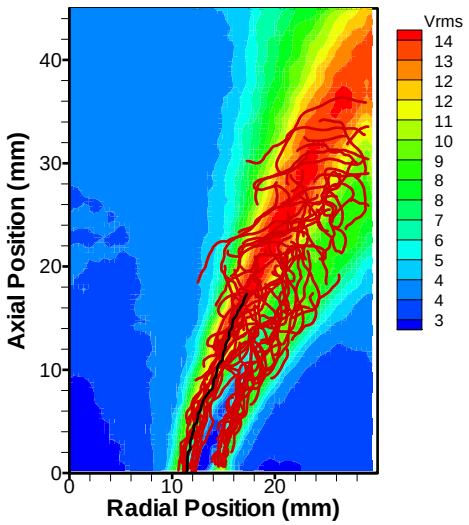

Figure 64: Averaged flame front (black line) and 30 instantaneous flame fronts for unsteady CH_4 flame on the top of the rms of the axial velocity

6.3 Stable Flames

Because quantitative analysis of flames under near blowoff conditions is very difficult with this Mie scattering based analysis approach, data were taken under conditions very close to, but removed from the unsteady region. These data points are indicated in **Figure 58**.

The key quantity of interest for these measurements is the flame stretch rate, which has two contributing terms, strain rate and curvature effects [15].

$$\kappa = \nabla_t \cdot \vec{u} + S_d(\nabla \cdot \vec{n}) = (\delta_{ij} - n_i n_j)\frac{\partial u_i}{\partial x_j} + S_d \frac{\partial n_i}{\partial x_j} = \kappa_s + \kappa_c \quad (48)$$

where $\vec{n}$ is the normal vector of the flame, pointing at the cold reactants and S_d is the local displacement flame speed. The curvature term is much smaller than strain term here, so only strain term is studied in this work.

Attention is focused on the strain rate just upstream of the flame where gas expansion is negligible and, thus, the flow is essentially incompressible (the flow Mach number at the nozzle exit is ~ 0.1). Then the strain term, κ_s, can be simplified as:

$$\kappa_s = \frac{\partial u_i}{\partial x_i} - n_i n_j \frac{\partial u_i}{\partial x_j} = -n_i n_j \frac{\partial u_i}{\partial x_j} \quad (49)$$

In cylindrical coordinate system, the strain rate can be expressed as;

$$\kappa_s = -n_r^2 \frac{\partial u}{\partial r} - n_z^2 \frac{\partial v}{\partial z} - n_r n_z \frac{\partial u}{\partial z} - n_r n_z \frac{\partial v}{\partial r} - \frac{n_\theta^2}{r}\frac{\partial w}{\partial \theta} - \frac{n_r n_\theta}{r}\frac{\partial u}{\partial \theta} - \frac{n_z n_\theta}{r}\frac{\partial v}{\partial \theta} - n_r n_\theta \frac{\partial w}{\partial r} - n_z n_\theta \frac{\partial w}{\partial z} \quad (50)$$

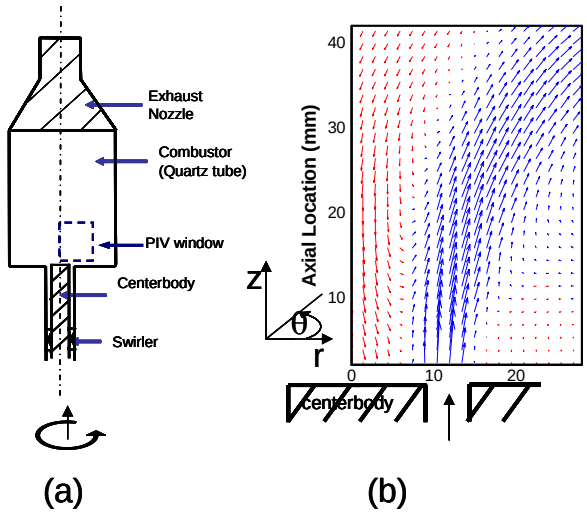

Figure 65: Schematic of PIV measurement window (a), and flow structures of averaged stable methane flame in a swirling combustor

Definitions of coordinate system in eqn.(50) are indicated in Figure 65(b), where *u*, *v*, and *w* indicate the velocities in *r*, *z*, and θ directions. Terms 1-4 in eqn.(50) are resolved by the PIV measurements and terms 5-9 are unresolved, being out of plane. However, these unresolved terms are small relative to the resolved, in plane terms in the *near field*

of the attachment point (but not in general) because the flame is stabilized in the shear layer of the cylindrical centerbody, whose azimuthal normal component, n_θ, is zero. The flame sheet closely conforms to this shape, as evidenced by visual observations in the centerbody near field. However, it must be emphasized that farther downstream, the flame sheet is certainly non axi-symmetric in an instantaneous sense.

In the averaged velocity field, the centerline of the high speed jet is determined by the maximum axial velocity point at each axial level, see Figure 66 (a). The centerline is smoothed by a third order curve fitting, see Figure 66 (b). A second (*t, n*) coordinate system was defined that is parallel (*t*) and orthogonal (*n*) to the streamline at the jet centerline of the average velocity field, which is indicated by the solid black line in Figure 66. The corresponding velocities are given by u_t and u_n and flame normal by n_t and n_n.

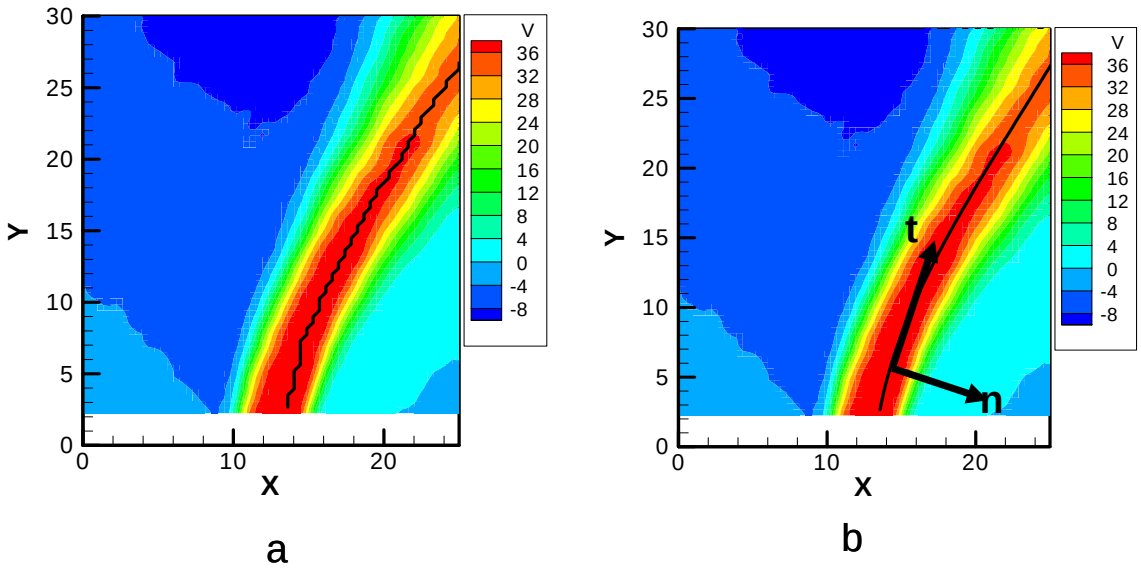

Figure 66: (a) Maximum of axial velocity at each axial location (solid black line) with averaged axial velocity field. ; (b) Smoothed centerline (solid black line) with averaged axial velocity field.

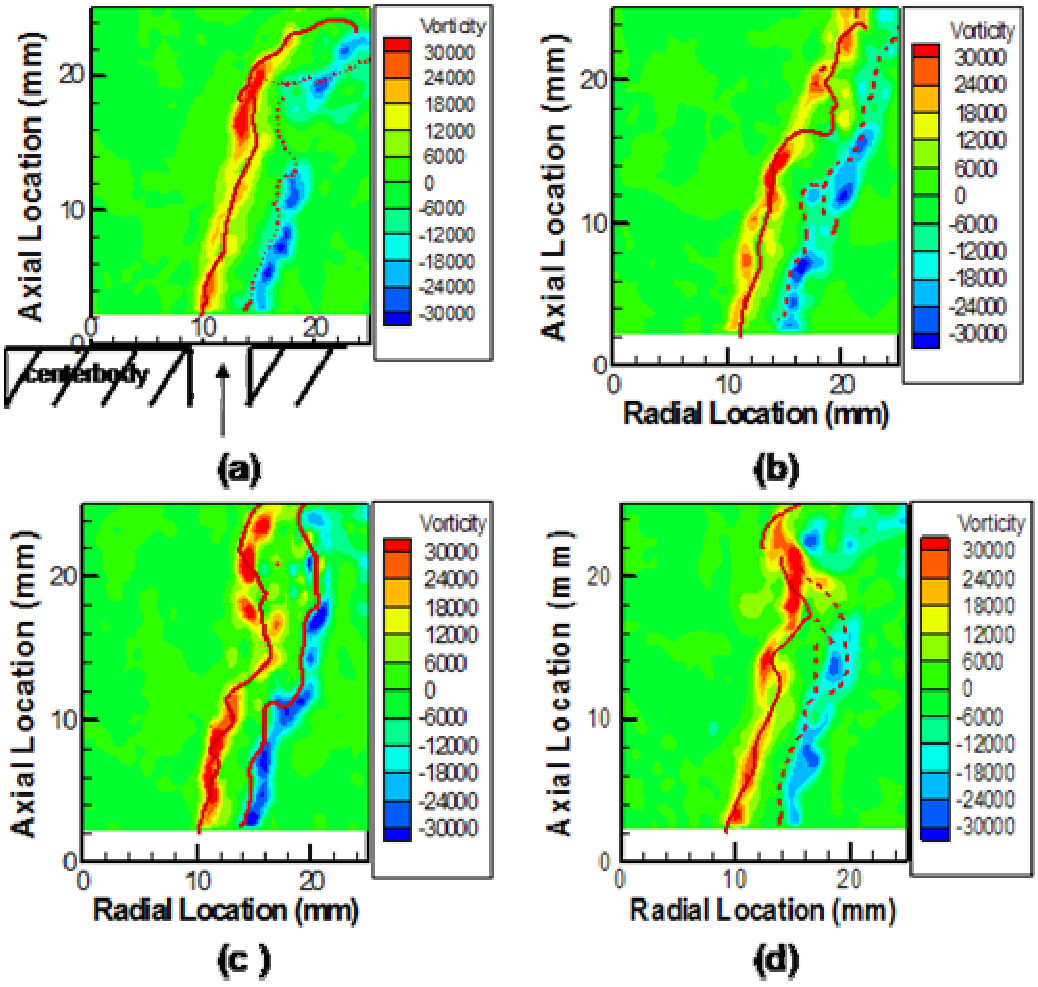

Figure 67: Instantaneous iso-vorticity field and flame location for (a) CH_4, (b) 20/80% H_2/CH_4, (c) 50/50% H_2/CH_4, 75/25% H_2/CH_4

Figure 67 shows four typical instantaneous flow field and flame position snapshots for different mixtures. In addition, the 2D vorticity component, $\omega = \frac{\partial v}{\partial r} - \frac{\partial u}{\partial z}$, and instantaneous flame front is shown. The inner and outer flame sheets are stabilized in the shear layers of the centerbody and rapid expansion, respectively. This study focuses on the inner flame sheet which rides along the periphery of the annular jet and is located in

the shear layer. Because of the very high nozzle velocity, the flame is oriented very nearly vertical in the immediate vicinity of the nozzle exit and bends outward farther downstream, as it follows the trajectory of the annular jet.

In many instances, the vorticity is concentrated into discrete blobs, apparently associated with the quasi-periodic rollup of the shear layer due to the Kelvin-Helmholtz instability. In some cases (e.g., **Figure 67** c), the entire flame and shear layer is undulating, possibly a manifestation of the instability of the annular jet column.

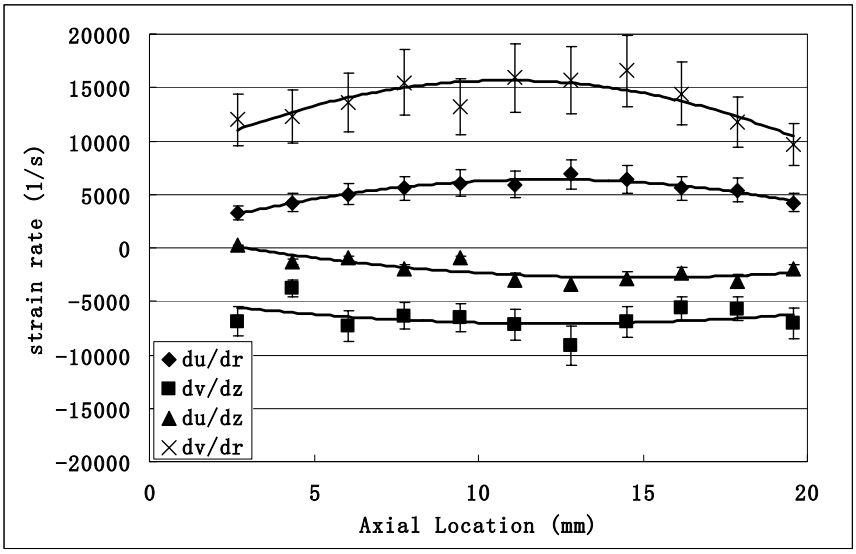

Figure 68: Velocity gradients for CH4 flame in cylindrical coordinate system

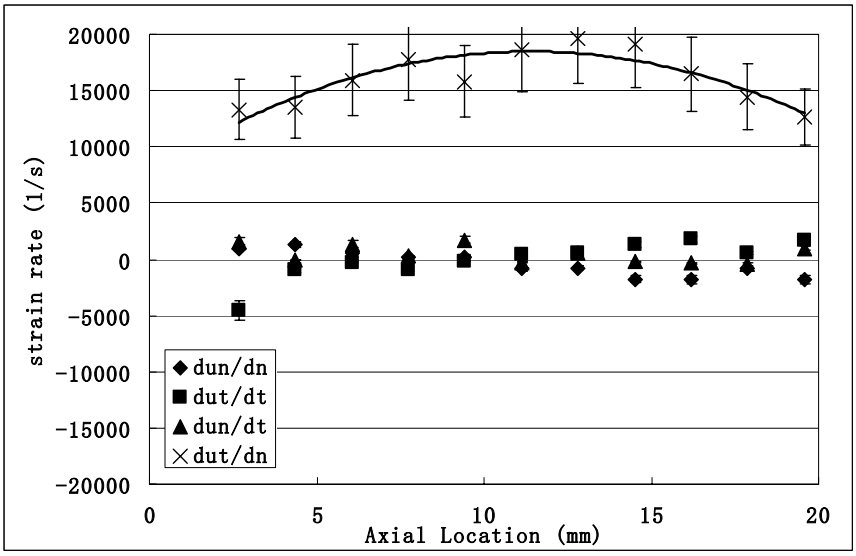

Figure 69: Velocity gradients for CH4 flame in rotated Cartesian coordinate system

Figure 68 shows the flow velocity gradients along the averaged flame front for the CH_4 flame. Over five hundred shots were taken for each condition, and averaged velocity field was used in calculations. The uncertainty analysis for velocity, velocity derivative, strain rate, and flame orientation is detailed in appendix. In general, velocity and velocity derivative uncertainty in this study is estimated to be on the order of 5% and 20%, and the uncertainty for strain rate 1100 1/s. The resultant uncertainty in the angular estimate is ± 3 degrees. Because of the rapid expansion and rapid divergence of the jet due to its swirl, there is a rapid axial deceleration of the high speed jet, $\partial v/\partial z << 0$. Correspondingly, there is a rapid increase in radial velocity of the jet in the radial direction, $\partial u/\partial r >> 0$. The sum of these two terms, $\frac{\partial u}{\partial r}$ and $\frac{\partial v}{\partial z}$, only has a small magnitude (~ 200 1/s), because the flow is incompressible and the time averaged flow is axi-symmetric; i.e. $\frac{\partial u}{\partial r}+\frac{\partial v}{\partial z}=-\frac{u}{r}$. Indeed, evaluation of this sum provides an

independent assessment of the errors in calculation of time averaged derivatives. This can be quantified by considering the ratio $|-\frac{u}{r}|/|\frac{\partial u}{\partial r}|$, which has average values of around 20 %. The largest flow velocity gradient term, $\partial v/\partial r$, primarily reflects the strong shearing in the flow. This term is larger than $\partial v/\partial z$ by a factor of three. Finally, the variation in radial velocity in axial direction, $\partial u/\partial z$, has the lowest magnitude, being smaller than the axial flow deceleration terms by a factor of two.

Because the flame and flow bends outward, it is difficult to distinguish between downstream changes in the flow field and simple changes in orientation of the annular jet. For this reason, Figure 69 plots the velocity derivatives in the rotated *n*-*t* system, see Figure 66(b). The points of maximum vertical velocity at each axial location went through a third order polynomial curve fitting to generate the high speed jet line. At each height, the new system is defined as perpendicular (*n*) to and tangential (*t*) to the high speed jet line. Strain rates are recalculated in this new coordinate system. From this it can be seen that, the relative roles of these terms change greatly. $\partial u_t/\partial n$, reflecting the strong shearing in the flow, still has the largest derivative value. $\partial u_t/\partial t$, presenting the deceleration, is much smaller than the shear term.

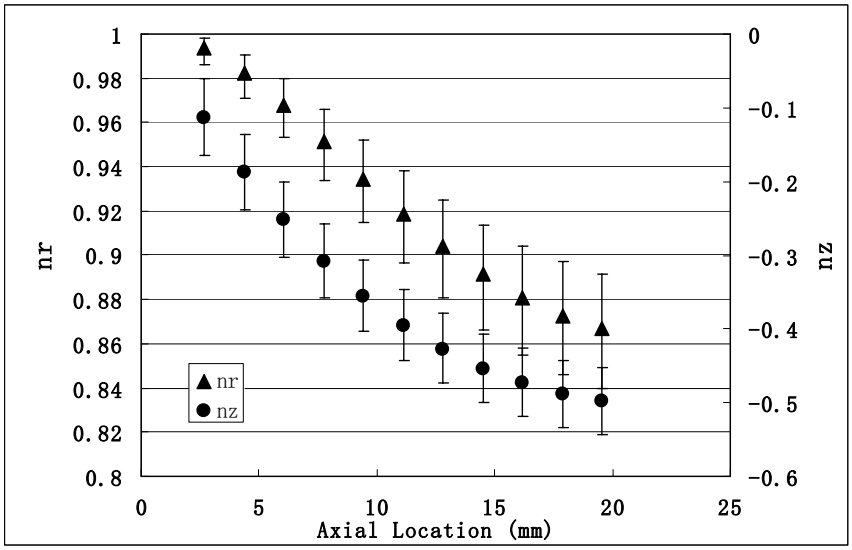

Figure 70: Components of normal vector along the CH_4 flame in cylindrical coordinate system

Having considered the trends in velocity derivatives, we next consider the flame orientation characteristics, n_r, n_z, n_n and n_t (Figure 70 and Figure 71). These orientation characteristics play a very important role in determining the overall flame strain rate and the key contributors to this strain rate. In general, the angle between flame front and dump plane decreases as the flame bends outward in downstream. Although flame angle almost changes 20 degrees from 2 mm to 20 mm axial location, n_r only changes around 10%. However, the magnitude of n_z changes greatly. Under the rotated coordinate system, which is attached to the jet flow, n_n almost equals to 1 along the whole flame, while n_t has a much smaller magnitude along the flame.

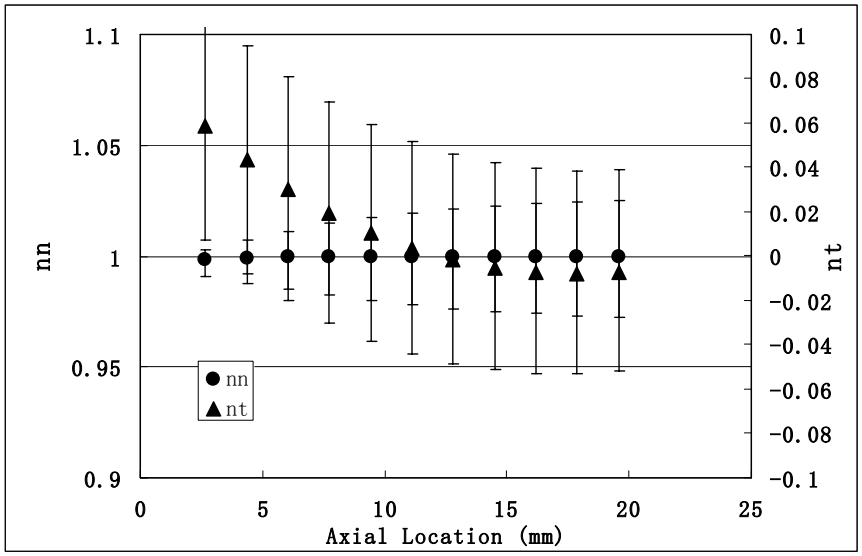

Figure 71: Components of normal vector along the CH_4 flame in rotated Cartesian coordinate system

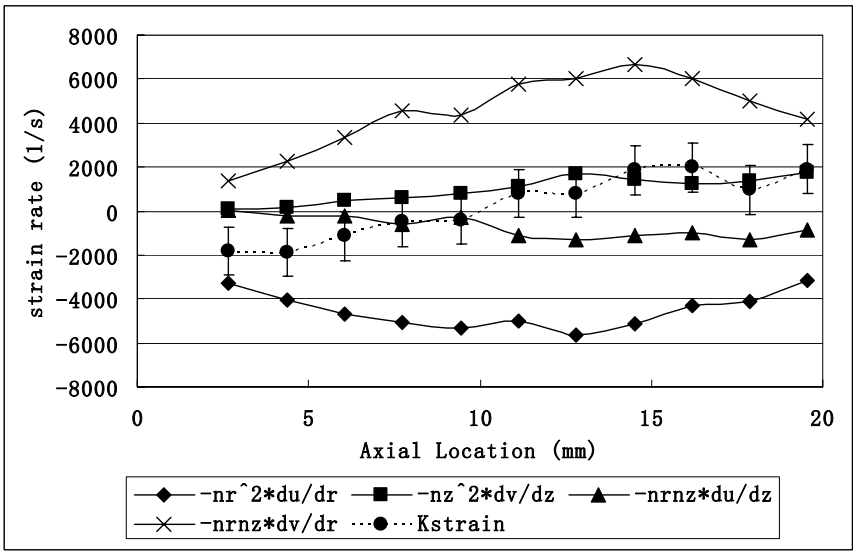

Figure 72: Four strain terms along the CH_4 flame in cylindrical coordinate system

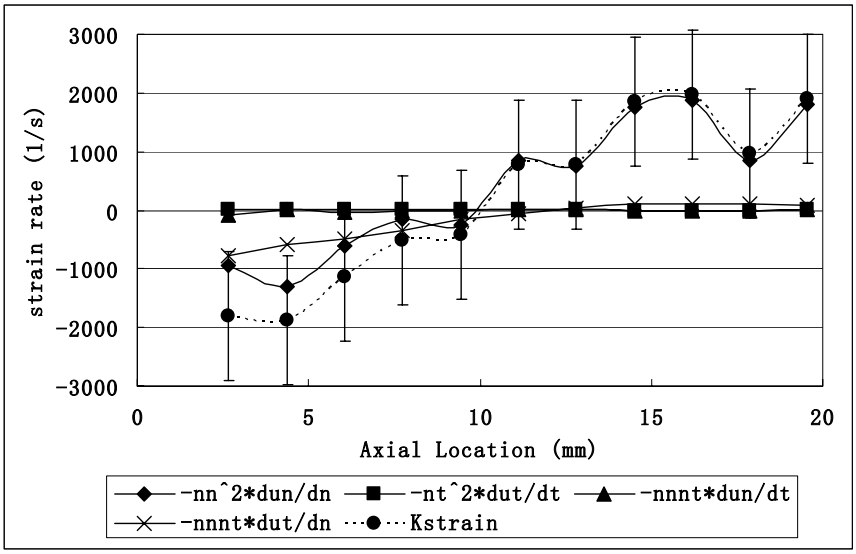

Figure 73: Four strain terms along the CH_4 flame in rotated Cartesian coordinate system

Figure 72 and Figure 73 plot the four contributing strain terms, plus their sum (the total hydrodynamic flame strain rate) along the methane flame. In Figure 72, start with the strain rate characteristics near the attachment point, z< 20 mm. In this region, the two dominant contributors to the flame strain flame remain the same as for the velocity gradients – the axial deceleration term, $\partial v/\partial z$ and the axial shearing term, $\partial v/\partial r$. However, because the flame is oriented nearly parallel to the flow (n_r ~0.95 and n_z ~0.15), the relative significance of these terms on the strain rate is inverted. As such, the largest straining term comes from the $-n_r^2 \frac{\partial u}{\partial r} \approx n_r^2 \frac{\partial v}{\partial z}$ term, a negative, or compression strain. The other axial deceleration term, $(-n_z^2 \frac{\partial v}{\partial z})$, is very small due to the low value of n_z. The large axial velocity shear term, $\partial v/\partial r$, is actually of secondary importance in this

region because of the low magnitude n_z in this region, $(-n_r n_z \frac{\partial v}{\partial r})$. This term is a positive, extensional straining term.

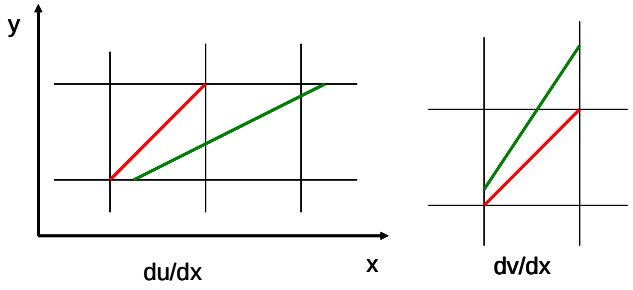

Figure 74: The manner in which flow strain terms strain the flame

Thus, we see that the flame strain characteristics are dominated by two factors – one due to flow deceleration and the other due to flow shear. Figure 74 shows how these two terms result in flame strain. The line segments illustrate two material lines, the red line at some initial instant and the green line at a later one, which is stretched or compressed due to flow velocity gradients

$$\kappa_{strain} = -n_n{}^2 \frac{\partial u_n}{\partial n} - n_t{}^2 \frac{\partial u_t}{\partial t} - n_n n_t \frac{\partial u_n}{\partial t} - n_n n_t \frac{\partial u_t}{\partial n} \quad (51)$$

Figure 73 shows the strain results under the rotated coordinate system, which follows the high speed jet. Since the new system follows the high speed jet, deceleration and shear terms can be distinguished. As expected, the sum of these terms, or total strain rate, is unaffected. The relative roles of these terms change greatly. The four strain terms in eqn (51) show that flow deceleration is the key contributor to flame strain. In general, flame front bends with high speed jet, so the flame normal almost coincides with the s

axis. It makes $n_n \approx 1.0$ and $n_t \approx 0.01$. The magnitude of $(-n_n n_t \frac{\partial u_t}{\partial n})$ are too small due to n_t. Physically, the flame front stays near the edge of high speed jet at the exit of premixer, so flow deceleration strongly compresses the flame surface. Moving downstream, the flame front still locates inside the shear layer, but slightly away from the center of high speed jet. In this area, the flow is accelerating, so the flame experiences positive stretch. Due to orientation of the flame front and the high speed jet, the shear terms is negligible relatively to the deceleration term.

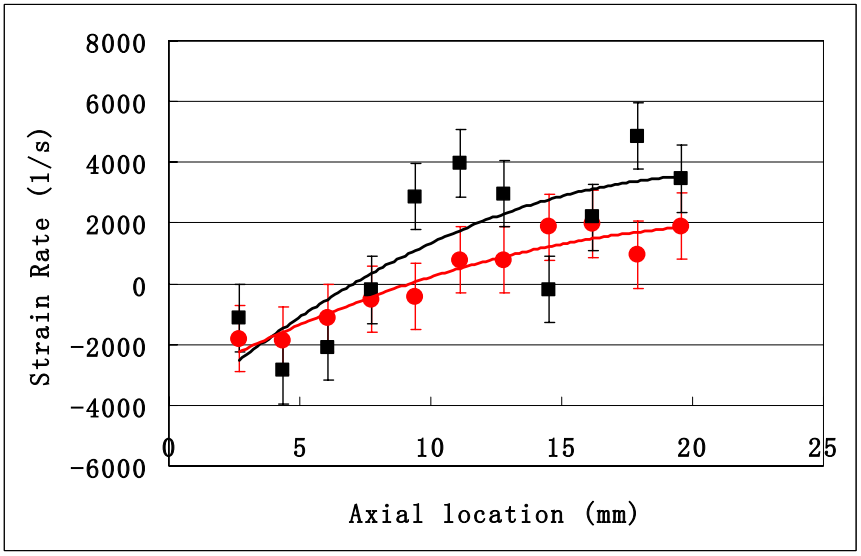

Figure 75: Total strain rate along the CH_4 flame determined by averaged flow field and averaged flame orientations (red circle); average of 40 instantaneous of velocity derivatives and flame orientations (black square)

It should be emphasized that all the calculations are obtained by multiplying velocity derivatives from averaged flow field and averaged flame orientations. The

results of this calculation are not necessarily the same as that obtained from averaging the instantaneous velocity derivatives and flame orientations. To illustrate the difference between these calculations, Figure 75 plots the strain rates for the methane flame determined by two methods. The solid black line indicates the trend line for strain rates from averaging of the instantaneous strain rates, and the red one is for strain rates from averaged flow field and averaged flame orientations. It can be seen that the trends are qualitatively similar, with quantitative differences

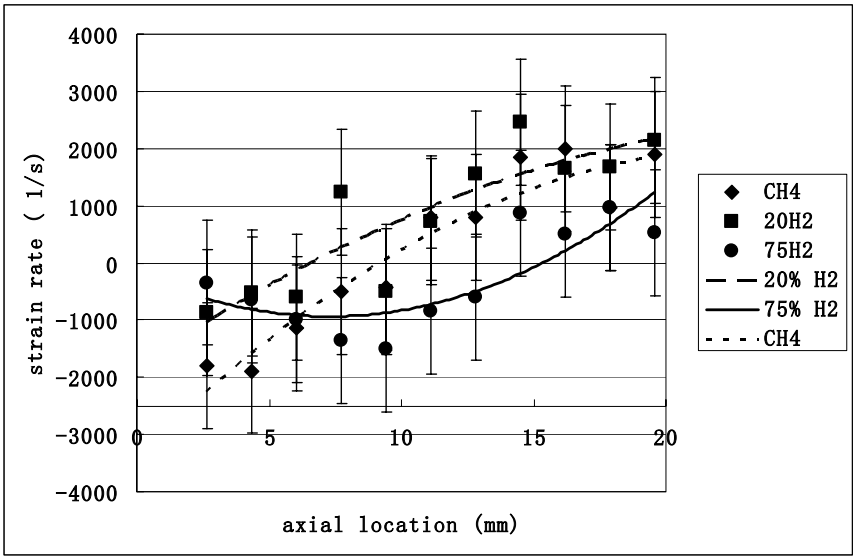

Figure 76: Flame strain rate along the flame for different hydrogen mixtures

The flame strain rates for different hydrogen mixtures, obtained from the average flame position and flow field, are plotted in Figure 76. It shows that there are systematic differences between the levels of flame strains along the flame for different mixtures. Methane flame and methane flame with 20%H_2 addition have a very similar trend. Near the nozzle exit, the flames are compressed. Moving downstream, the strain rate increases

toward zero and then to positive values. However, the highest hydrogen flame shows a slight different trend. The negative strain rate becomes positive further downstream than low hydrogen flames. This can be explained by the orientation of the flame. The flow fields for these flames are quantitatively similar, so the flame orientations are critical to the strain rates. Figure 77 show the values of n_x along the flame for three mixtures. It is clear that methane and 20/80% H_2/CH_4 flames have a similar trend as the methane flame, which results in the similar strain rates, see Figure 76. However, for high H_2 flame, n_x is smaller than low hydrogen flames near the exit of nozzle (0.97 vs. 0.99), which means that the flame bends outwardly more (or closer to the center of high speed jet). This makes the high hydrogen flame moves into the acceleration zone (positive strain rate) in further downstream than low hydrogen flames.

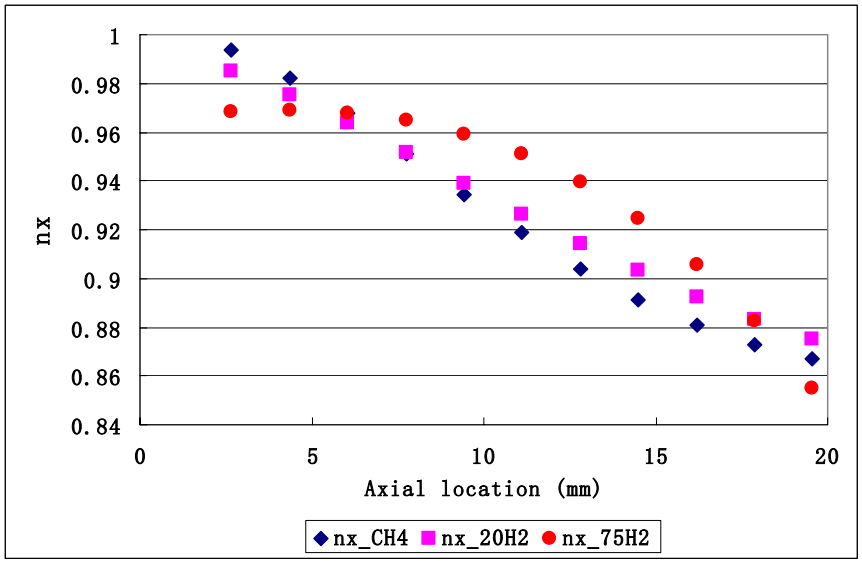

Figure 77: Orientations of flame fronts for 0/100(blue diamond), 20/80(pink square) and 75/25% (red circle) H_2/CH_4 flames.

6.4 Unsteady Flames

In unsteady region, the flame near-attachment point starts to become unsteady and exhibit local extinction events. To study the properties of unsteady flames, especially flame holes, PIV measurements were performed close to the stable/unsteady boundary, but removed from blowoff limit to avoid the flame dynamics near blowoff as discussed in chapter 5. The details of experimental conditions are shown in **Figure 58**. The left flame branch, which is attached to the centerbody, is considered here.

In general, the strain characteristics near attachment points for unsteady flames are qualitatively similar to stable flames, with quantitative differences. For example, Figure 78 shows the strain rates along 0/100, 20/80, and 50/50% H_2/CH_4 flames for unsteady flames. Near the nozzle exit, starting with a negative strain rate, flames are compressed. Moving downstream, the strain rate increases towards zero and then becomes positive values, where the flames are stretched. As in stable flames, flow deceleration is still the key contributor to flame strain. Figure 79 shows strain rates on unsteady methane flame determined by two methods. The solid black line indicates the trend for strain rates from averaging of 30 instantaneous strain rates. The red line indicates the trend from averaged flow field and flame orientations. As for stable flames, these two methods show a similar trend.

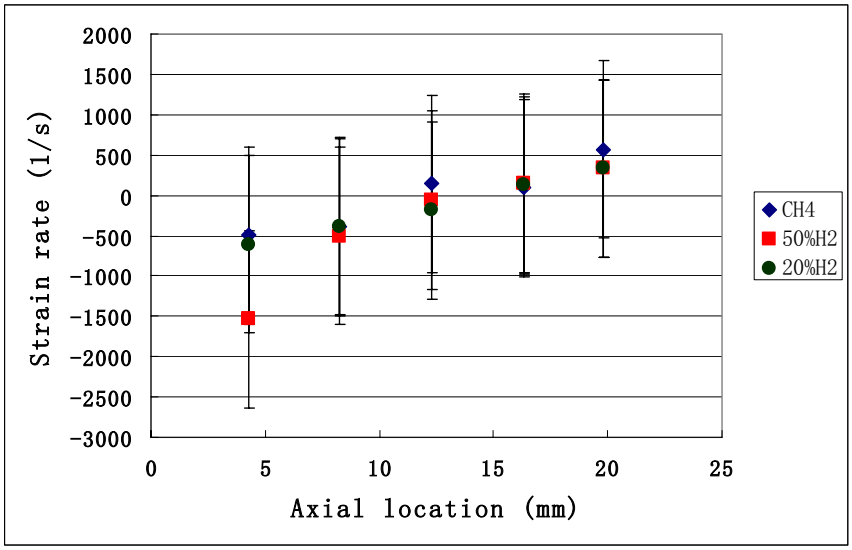

Figure 78: Total strain rates along flames of different hydrogen mixtures for unsteady flames

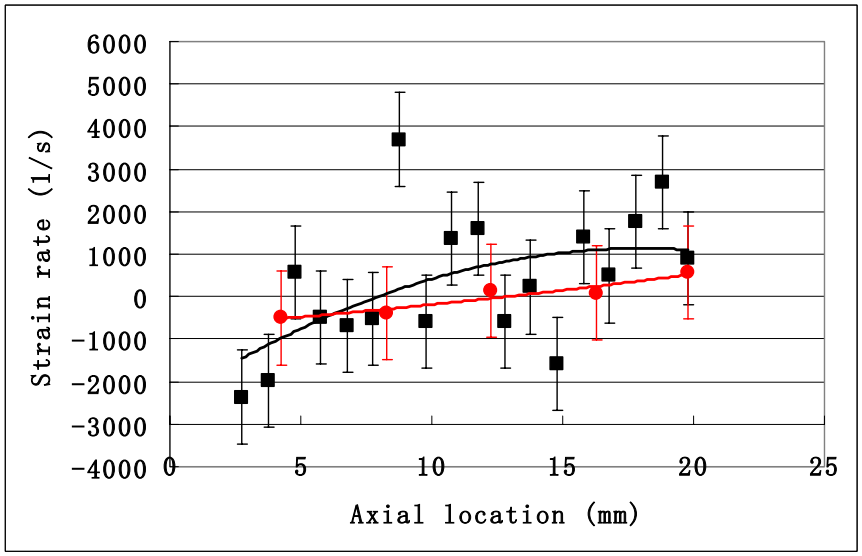

Figure 79: Total strain rate along unsteady CH_4 flame determined by averaged flow field and averaged flame orientations (red circle); average of 30 instantaneous of velocity derivatives and flame orientations (black square)

Holes are detected in the flame sheet for unsteady flames, see Figure 80. Those holes are defined as the broken area along the flame, where the gradient of particle densities falls below the threshold. However, it should be pointed out that there is a time delay between flame extinction and the formation of the hole. The flame front here is detected by the difference of densities, which is related to the temperatures. So when local extinction occurs, the density will not change immediately. A diffusion time should be considered, which should be associated with the thermal diffusion.

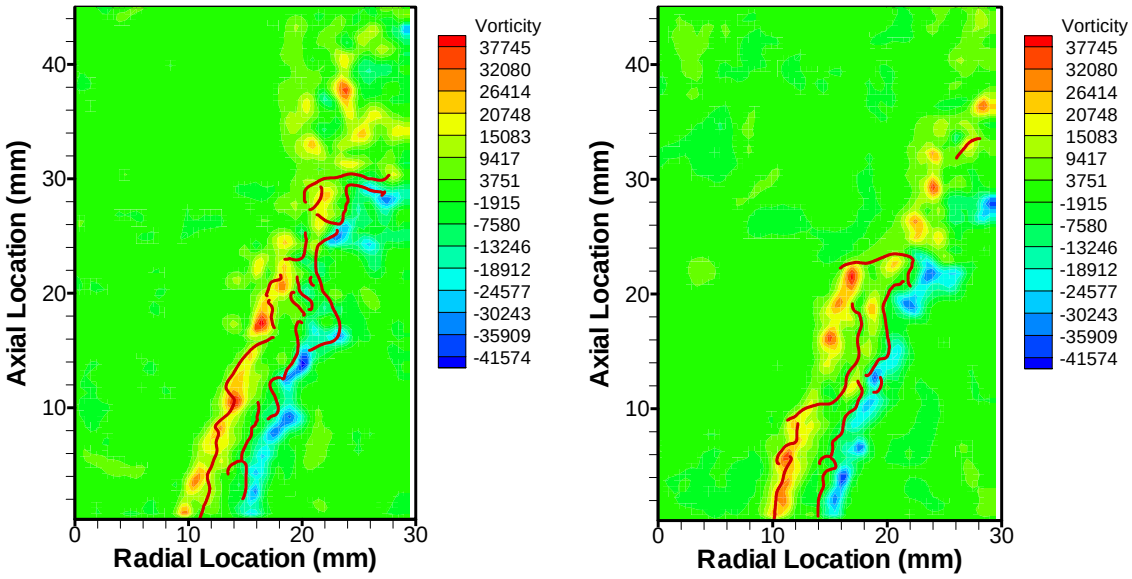

Figure 80: Two instantaneous iso-vorticity fields and flame fronts for unsteady CH_4 flame

Holes locations for 30 instantaneous CH_4 flame were recorded. Figure 81 shows the distribution of holes locations in axial direction. In this histogram-like plot, each bin is 1 mm wide in axial direction. The numbers of holes which fall into each bin are normalized by the total number of holes in 30 images. The data shows that there are no holes near the centerbody (2-5 mm). Moving downstream, the probability of holes distribution is gradually increases. As discussed above, the threshold used for holes

detection greatly affects the holes locations. However, if the threshold is higher, the holes will be bigger, which means that the curve shown in Figure 81 is shifted downstream. If the threshold is extremely high, some holes merge, but the trend in Figure 81 will not be changed greatly.

In this work, flame holes are hardly observed near the centerbody (0-5mm), although the magnitude of strain rate in this area is similar or even higher than the strain rates of downstream flame. One reason is that the holes are formed with a delay time, so that they are not detected immediately. However, it should be emphasized that the strain rates along the flame are negative in this area. As discussed in introduction, there is essentially no data on the dynamics of highly compressed flames.

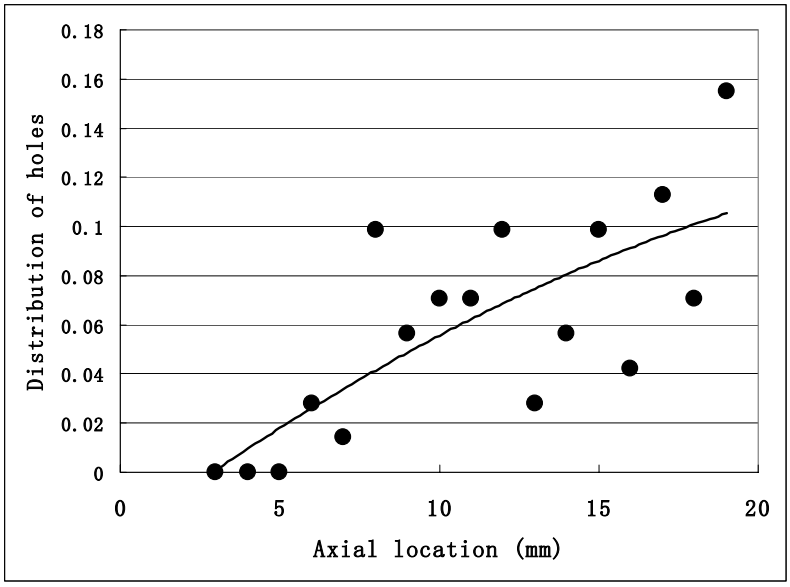

Figure 81: Holes distributions along unsteady CH_4 flame

It will next be shown that this distribution of holes can be understood by the time delay required for their detection and their convection. Assume that 5 holes are

generated randomly along the flame front (0-20mm) per microsecond. In addition, the formed holes propagate downstream with the flow at the speed of 30 m/s, which is related to the flow speed at the nozzle exit. The distribution of flame holes after 1000 microseconds is shown in **Figure 82**. In general, this result shows that more and more holes are distributed with downstream distance, similar to the trend in Figure 81. However, it also shows holes near the centerbody (0-5 mm) and the linear distribution, which are not observed in the experimental data.

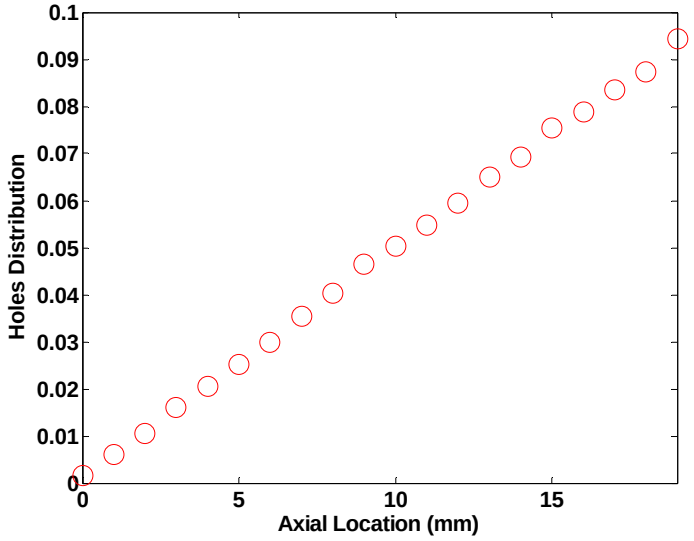

Figure 82: Holes distribution along the flame front. Holes are generated randomly along the flame and propagate downstream with the averaged flow speed.

The simulation above assumes that if a flame extinguishes, the hole can be detected immediately. In fact, once the flame locally experiences a high strain rate, which exceeds the extinction strain rate, it will take a response time for the flame to extinguish. This response time scale is related to the chemical time of the flame. In addition, there is a time delay between flame extinction and the formation of the hole.

When local extinction occurs, the densities across the flame will not change immediately. A diffusion time should be considered, which should be associated with the thermal diffusion. However, it is hard to give an appropriate and accurate delay time, which includes all the delays. So in this work, the delay time is just simply scaled by chemical time based on reaction layer thickness, $\tau_{delay} = \frac{l_r}{S_L}$ (l_r denotes the reaction layer thickness). It is clear that this time scale is not accurate, but it represents the importance of the delay time. This time scale is in the range of 0.0001 to 0.0002 s, which depends on the equivalence ratios and fuel types. After adding this assumption to this model, the simulation results are shown in Figure 83. These two distribution curves match very well along the flame. There are almost no holes lower than 5mm axial location. Downstream of that, more and more holes are distributed. Results of holes distribution for 50/50% H_2/CH_4 flame are plotted in Figure 84, which also shows that the simulation work matches the experimental data.

The results of this simulation work suggest that a random generated holes distribution with a delay time can be used to understand the holes distribution in experimental data. Once the hole is generated, it propagates downstream with the flow. Perhaps, some cold reactants enter the recirculation zone through these flame holes, and are recirculated back to the stabilization point of the flame. As lean blowoff is approached, more holes are generated, and more cold reactants enter the recirculation zone.

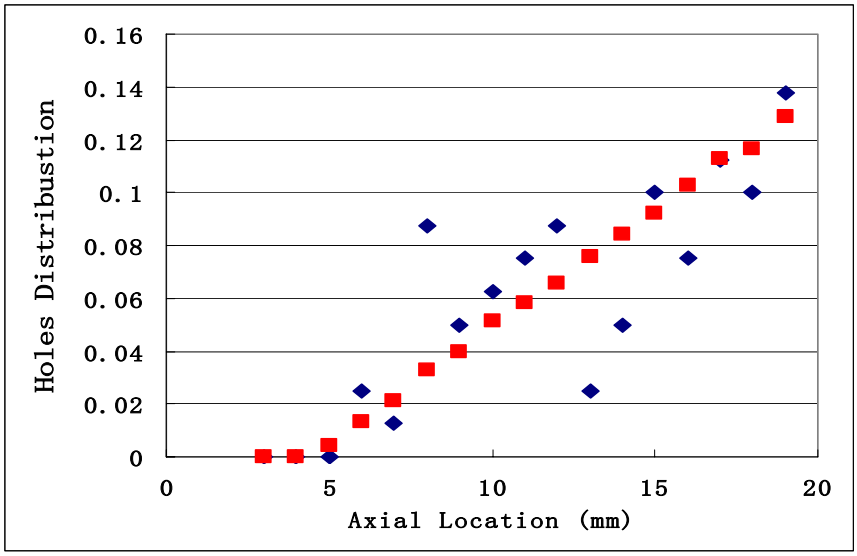

Figure 83: Holes distribution along the flame front for CH_4 flame. Holes are generated randomly along the flame with a delay time, and generated holes propagate downstream with the speed of 30 m/s. (Blue diamond: experiments; Red square: simulation)

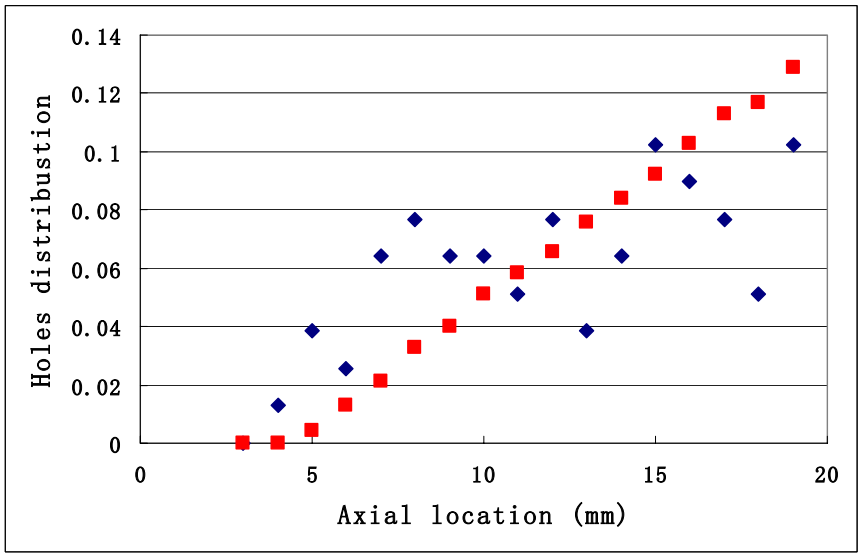

Figure 84: Holes distribution along the flame front for 50/50 H_2/CH_4 flame. Holes are generated randomly along the flame with a delay time, and generated holes propagate downstream with the speed of 30 m/s. (Blue diamond: experiments; Red square: simulation)

CHAPTER 7

CONCLUSIONS AND RECOMMENDATIONS

7.1 Conclusions of Present Work

The overall objective of this work was to characterize the lean blowoff phenomenon and develop methods for correlating and predicting lean blowoff of $H_2/CO/CH_4$ mixture in a swirl stabilized combustion system. This was accomplished by three efforts which delved into flame stabilization with increasing levels of quantitative and physical details. First, lean blowoff limits of $H_2/CO/CH_4$ mixtures were measured under different approach flow speeds, reactant temperatures, and combustion pressures. Correlations based upon both flow and mixture properties were then developed. Second, the blowoff phenomenology was systematically characterized as a function of the fuel compositions. The dynamic blowoff process was studied by chemiluminescence measurements, high speed imaging, and flow field measurements. The last effort quantitatively analyzed the strain characteristics in the vicinity of the attachment point of stable and unsteady flames.

The first part of this thesis concentrated on the correlations of lean blowoff limits. Tests were performed in a high pressure gas turbine combustor simulator under different test conditions (approach flow speed, reactant temperature, and combustor pressure). It was found that percentage of hydrogen dominates the lean blowoff limits of $H_2/CO/CH_4$ mixtures. In fact, the percentage of hydrogen the dominant variable describing fuel compositions and influences on blowoff limits, and many other physically meaningful variables are simply functions of percentage of hydrogen. Moreover, Damköhler number

correlation based on blowoff residence time can be used to correlate the blowoff limits over all flow velocities, pressures and temperatures for all mixtures with H_2 levels below around 50%. As the percentage of hydrogen increases over this level, the Damköhler number was decreased significantly. Preferential diffusion effect, which is associated with the high diffusivity of hydrogen, was suspected to be an important reason, given that the flame in a swirling combustor is highly strained. So a Damköhler number correlation with diffusion correction was developed, which is based on the local equivalence ratios. This modified Damköhler number has the capability for correlating and predicting the blowoff equivalence ratios for $H_2/CO/CH_4$ mixtures over all the ranges. More fundamentally, the variation of Damköhler number with the percentage of hydrogen is likely due to the fact that the controlling kinetic time scale is the inverse o f the extinction strain rate, as suggested by the results in chapter 4.

The second part of the study focused on the qualitative flame dynamics near blowoff. The objective of this part was to systematically characterize the blowoff phenomenology as a function of the H_2 levels in the fuel. Given that the key variable influencing these dynamics is H_2 level, only CH_4/H_2 mixtures were considered in this study. This work was accomplished through chemiluminescence measurements, high speed imaging, and velocity field measurements. It characterized the underlying flame dynamics near blowout in greater detail. As lean blowoff was approached, local extinction/reignition events were observed, similar to other studies in methane flames. These events were captured by OH* chemiluminescence measurements, which dropped to “near” zero values, indicating the occurrence of local extinction events. Moreover, as lean blowoff was approached, the frequency of events was increased greatly. High speed

imaging was used to visualize these events, and show a variety of highly dynamic flame features, which vary substantially with the H_2 levels in the fuel. A columnar flame shape was observed for high hydrogen flames. However, it should be emphasized that blowoff phenomenology is geometry dependent and is a function of boundary conditions. To verify the relative roles of fluid mechanics and chemical kinetics in causing the variation in near blowoff phenomenology, flow field measurements were obtained using PIV where the relative H_2/CH_4 mole fractions were varied, but by adjusting the overall mixture stoichiometry such that the gas expansion ratio across the flame and adiabatic flame temperature (calculated) remained nearly constant. Another set of data were obtained where both H_2/CH_4 mole fractions and flame temperatures were varied. Results from the first set illustrate that the time averaged flow field (locations of the recirculation zone boundaries) are identical, regardless of the fuel H_2/CH_4 ratio. In addition, the second set shows the flow field is also not very sensitive to the thermal expansion ratio. All the stable flames have an identical flow structures, which is significantly different with the nonreacting case. However, near blowoff, the size of the IRZ reduces as the percentage of H_2 increases. This result suggests that the average flow field structure is controlled by both the thermal expansion and kinetics. This suggests that the fluid mechanic structure of the flow for the near blowoff flames maybe due to fluid mechanics effects, as the flame can remain stabilized at lower temperatures(due to kinetic effects). The instantaneous flow fields show that the oscillation between "extinction" and "reignition" phases near blowoff is associated with an oscillation between two "stabilization points" of the flame. Chemical kinetics, particularly strain sensitivities, certainly exerts a role on this dynamic oscillation between the attached and unattached

flames. In general, the results show that the flame dynamics near blowoff is controlled by both fluid mechanics and chemical kinetics, and the flame temperature and extinction strain rate are two critical variables describing these influences.

The third part of this study focused on the strain characteristics near the attachment point. It characterized the flame strain for stable and unsteady flames in greater detail, and related to the blowoff correlation and extinction strain rate. Quantitative flow field measurements focused on a small area near the flame attachment point. A rotated Cartesian coordinate, which is attached to the high speed jet, was used to distinguish between the effects of flow deceleration and shearing on flame strain. The results show that flow deceleration is the key contributor to flame strain. In general, the flame front stays near the edge of high speed jet at the exit of premixer, so flame surface there is strongly compressed by flow deceleration. Moving downstream, the flame front is still located inside the flow shear layer, but slightly away from the center of high speed jet, where the flow is accelerating, so the flame experiences positive stretch. Due to the orientation of the flame front and the high speed jet, the shear term is negligible relative to the deceleration term. Holes on flame surface, generated by local extinction, are detected for unsteady flames near blowoff. The probability of a hole occurring at a given point monotonically grows with downstream distance. A model, which assumes that holes are generated with randomly spatial probability, and propagate downstream at the flow speed, simulates the measured distribution of holes. Extinction strain rates for H_2/CH_4 mixtures were calculated at the corresponding equivalence ratios and test conditions. They show that the extinction strain rate for flames at the boundary where

they become unsteady and exhibit holes is almost a constant, regardless of the fuel H_2/CH_4 ratio.

This present study confirms that lean blowoff occurs in at least two phases (or limits). The first is that a stable flame starts to become unsteady and exhibits local extinction events. The second was the actual blowoff event. The first was associated with flame strain level, which exceeds the extinction strain rate, leading to local extinction or flame "holes". This study has shown that H_2/CH_4 mixtures reach this limit at similar extinction strain rates. This indicates that a Damköhler number based on extinction strain rate at the first limit is also almost a constant for all H_2/CH_4 mixtures. Flames are very unsteady after passing the first limit, and have a variety of highly dynamic flame features as shown in Chapter 5. These features involve complex interactions between the inner recirculation zone (vortex breakdown bubble), outer recirculation zone of the rapid expansion, and flame extinction/reignition phenomenon, which are not well understood. However, this research shows that these flame dynamics near blowoff are functions of H_2 level *at the same boundary conditions*. Both chemical kinetics and fluid mechanics affects these flame dynamics. A Damköhler number, considering preferential diffusion effects, could correlate and predict the lean blowout limits (the second limit) very well. However, it is speculated that this Damköhler number correlation does not include the physics associated with the actual blowoff process. It probably still describes the first boundary. Damköhler number can be used to correlate blowoff, because these two limits are correlated, i.e., the lines representing these two limits are almost parallel with each other, see **Figure 58** in chapter 6. Diffusion phenomenon has been shown to be an important factor to lean blowoff in this study. This suggests that a well stirred reactor

mechanism for lean blowoff, in which transport phenomenon is insignificant, is probably not physically correct. The physical mechanism for the second limit (lean blowoff) is still unclear.

7.2 Recommendations for Future Studies

The following recommendations discuss the various improvements to this study that will help to improve the understanding of blowout phenomenon for syngas mixtures.

Improvement of the Damköhler number correlation in Chapter 4 can be achieved by utilizing the extinction strain rate to scale chemical time. However, a complete extinction strain rate database is still not available. A computation work focusing on it is recommended.

There is a clear absence of flame speed data, either laminar or turbulent, in this study. Unfortunately, due to convergence problems, laminar flame speeds for most of the test conditions in this work can not be calculated using CHEMKIN. COSILAB supplies the continuation method; however, it is not coupled with the flame speed model. Additional numerical work to couple this continuation method into flame speed model is necessary. One of the physical mechanisms of lean blowoff, flame propagation, can be verified if turbulent flame speeds can be modeled.

A better understanding of the flame dynamics near blowoff is required to understand the physical mechanism of lean blowoff. Unfortunately, the PIV system used in this work takes data with a frequency of around 15, which is too low to capture an extinction/reignition event. Moreover, the flame front was determined by gradient of particle densities in this study. A more accurate flame front can be determined by PLIF

technology. So a high frequency (>100Hz) simultaneous PIV and PILF measurements will be very effective.

In Chapter 6, the uncertainty for strain rate has the same magnitude as the averaged value. In addition, the strain rate calculation point in reactant side is relatively too far to the flame front, especially near the exit of nozzle. PIV measurements with a much smaller spatial resolution (0.5 mm in this study) can improve them.

The blowout correlation developed in this study has been tested in a variety of reactant temperature and combustion pressure with great success. However, this approach still needs to be tested under realistic industrial gas turbine conditions.

APPENDIX A

PIV UNCERTAINTY ANALYSIS

PIV was used in measuring flow field and strain rates in this work. This appendix focuses on analyzing the uncertainty in the processing of PIV data.

There are a number of potential systematic and random error sources in PIV measurements, as detailed in various sources, see [74, 82, 83]. Error due to out-of-plane motion is important to swirling flow. The laser sheet thickness, the duration between laser shots, and the seed density have been carefully optimized to minimize this error. Assuming an overall 10 m/s tangential velocity, the distance a particle travels between two successive laser shots is 50μm, 5% of the laser sheet thickness. Errors associated with identifying the cross-correlation peak are less than 2% [35]. Contribution from thermophoretic velocity bias is apparently not important in this high speed flow, where the average nozzle exit velocity is ~30 m/s. Eddies smaller than PIV spatial resolutions (0.5mm, Kolmogorov length scale is estimated to be ~ 0.1 mm), also contribute to the errors but are difficult to quantify [83]. Based on the analysis above and the results presented in [35, 82], velocity uncertainty in this study is estimated to be on the order of 5%.

Determining the velocity gradients required to evaluate Eqn.(50) requires getting as close as possible to the flame sheet in the strongly shearing flow, without allowing any bins to overlap the flame sheet itself, which would induce bias errors in the measurement. For this reason, derivatives were estimated using single-side differencing, as opposed to central differencing, which has larger uncertainties but allows one to get 16 pixels closer

to the flame. In general the velocity gradients were taken 0.5 to 1.0 mm away from the flame sheet in the reactant side. This method introduces systematic errors into estimation of the derivatives in the radial direction, such as $\frac{\partial u}{\partial r}$ (note that the shear layer is approximately 1-2 mm thick). The errors are much smaller for derivatives in the flow direction, such as $\frac{\partial u}{\partial z}$. Typical flame thicknesses are 0.1-0.2 mm, much smaller than this distance. A Monte-Carlo technique was used to estimate the uncertainties of velocity derivatives. Assume that velocity has a normal distribution, with a mean equal to the estimate from the experimental data and a standard derivative of 5%, the uncertainties in velocity derivatives is ~20%.

The local flame normal, is needed to evaluate eqn.(50). It is determined by fitting a least squares 3rd order polynomial through 11 points, 5 points each side (±0.15mm). The resultant uncertainty in the angular estimate is ± 3 degrees, based upon analysis of the variance of these 11 points about the curve. Local curvature is also determined from this polynomial. The minimal resolvable radius of curvature is ~0.3 mm, the size of Gaussian filter. However, the averaged curvature stretch term is negligible, due to the fact that strain term has at least one order larger magnitude than it.

Consider next the uncertainty in the overall strain rate, eqn.(50), which is a sum of several terms, each of which is a product of flame normals and velocity derivatives. Note that the flame is nearly vertical, implying that n_r~1 and n_z ~0. With regards to derivatives, the largest velocity gradient is the shearing term, $\partial v/\partial r$. The overall uncertainty in flame

strain rate is largely driven by two factors. First, term 4 in eqn.(50), $-n_r n_z \frac{\partial v}{\partial r}$, which is the product of the largest velocity gradient and the smallest normal component. Uncertainties in these normals are the single largest contributor to strain estimate uncertainties. Second, this term is positive, while the first term in eqn.(50) is negative. As shown in chapter 6, these two terms are of similar magnitude which implies that uncertainties in their individual values are magnified substantially in their difference. Because the uncertainties in several quantities are not small, particularly in the quantity of the normals, linearized error propagation approaches are not appropriate. As such, a Monte-Carlo technique was utilized, where the angle and local velocity were assumed to have a normal distribution with a mean equal to the measured value and standard deviation equal to the uncertainties quoted earlier. Then, 100,000 realizations of eqn.(50) were generated, resulting in a distribution of strain rate that was also close to Gaussian in shape. The uncertainties quoted in the results equal the standard deviation from this distribution. Typical values are 1100 1/s.

REFERENCES

[1] Ridchards, G.A., McMillian, M.M., Gemmen, R.S., Rogers,W.A., and Cully,S.R., "Issues for Low-Emission, Fuel-Flexible Power System", Prog. Energy Comb. Sci.,27, 2001, pp.141-169

[2] Schefer, R. W., Wicksall, D. W., and Agrawal, A. K., "Combustion of Hydrogen-Enriched Methane in a Lean Premixed Swirl-Stabilized Burner," Proc. Comb. Inst., Vol. 29, 2002, pp. 843-850.

[3] Shih, W. P., Lee, J., and Santavicca, D., "Stability and Emissions Characteristics of a Lean Premixed Gas Turbine Combustor," Proc. Comb. Inst., Vol. 26, 1996, pp. 2771-2778.

[4] Lewis, G. D., "Prediction of NOx Emissions," ASME Paper 81-GT-119, 1981.

[5] Zeldovich, J., "The Oxidation of Nitrogen in Combustion and Explosions", Acta. Physiochem., 21(4), 1946.

[6] Lefebvre, A. H., Gas Turbine Combustion, Taylor & Francis, Philadelphia, 1998.

[7] Klimstra, Jacob, "Interchangeability of Gaseous Fuels – The Importance of the Wobbe EXPERIMENTAL Index", SAE paper # 861578, 1986.

[8] Moliere, M., "Benefiting from the Wide Fuel Capability of Gas Turbines: A Review of Application Opportunities", ASME Paper # GT-2002-30017.

[9]Nicholson, H. and Field, J., "Some Experimental Techniques for the Investigation of the Mechanism of Flame Stabilization in the Wake of Bluff Bodies," Proc. Comb. Inst., Vol. 3, 1951, pp. 44-68.

[10]Nair, S., Lieuwen, T., "Acoustic Detection of Blowout in Premixed Flames", J. Propulsion and Power, Vol 21, No. 1, P32-39

[11] Nair, S., Rajaram, R., Meyers, A., Lieuwen, T., Tozzi, L., Beson, K., " Acoustic and Ion Sensing of Lean Blowout in an Aircraft Combustor Simulator", 43rd AIAA Meeting Papers, 2005, p 3627-3634

[12] Muruganandam, T., Kim,B., Olsen, R., Patel, M., Romig, B., and Seitzman, J., "Chemiluminescence based sensors for Turbine Engines", AIAA-2003-4490, 2003

[13] Muruganandam, T.M., Nair, S., Scarborough, D., Neumeier, Y., Jagoda, J, Lieuwen, T., Seitzman, J., Zinn, B., " Active Control of Lean blowout for Turbine Engine Combustors", J. Propulsion and Power, Vol. 21, No. 5, pp. 807-814.

[14] Law, C.K., " Combustion Physics", Cambridge University Press, New York, 2006

[15] Poinsot, T, Veynante, D., " Theoretical and Numerical Combustion", Edwards, Philadephia, 2001

[16] Law, C.K., Sung, C.J., "Structure, Aerodynamics,and Geometry of Premixed Flamelet", Progress in Engergy and Combustion Science, 26,459-505

[17] Glassman, I., Combustion, Academic Press: New York, 1996.

[18] Zukoski, E.E., "Afterburners", in Aerothermodynamics of Gas Turbine and Rocket Propulsion, G. Oates, Ed., 1997.

[19] Spalding, D., "Some Fundamentals of Combustion", Ch. 5, Butterworth Press: London, 1955

[20] Longwell, J., Frost, E., Weiss, M., "Flame Stability in Bluff-Body Recirculation Zones", Ind. Eng. Chem., Vol. 45 (8), pp. 1629-1633.

[21] Rizk, N. K., Lefebvre, A. H., "Influence of laminar flame speed on the blowoff velocity of bluff body stailized flames", AIAA Journal, v 22, n 10, pp 1444-1447

[22] Herbert, M.V., " Aerodynamic influences on flame stability", Progress in Combustion Science and Technology, v1, 1960, pp 61-109

[23] Williams, F. A., "Combustion Theory", Addison-Wesley Publishing company,1965

[24] A.A. Putnam, R.A. Jensen, "Application of Dimensionless Numbers to Flash-back and Other Combustion Phenomena" , Proc. Comb. Inst., 3rd, 1949, ,pp 89-98

[25] Radhakrishnan, K., Heywood, J., Tabaczynski, R., "Premixed Turbulent Flame Blowoff Velocity Correlation Based on Coherent Structures in Turbulent Flows", Comb. Flame,, 42, 1981, pp. 19-33.

[26] Plee, S.L, Mellor, A.M., "Characteristic Time Correlation for Lean Blowoff of Bluff Body Stabilized Flames", Comb. Flame,, 35, 1979, pp. 61-80.

[27] Loblich, K. R., " Semitheoretical Consideration on Scaling Laws in Flame Stabilization", Proc. Comb. Inst., 9th pp949-957

[28] S. Hoffmann, P. Habisreuther, B. Lenze, "Development and Assessment of Correlations for Predicting Stability Limits of Swirling Flames", Chemical Engineering and Processing, 33 (1994), pp 393-400

[29] Strakey, P., Sidwell, T., Ontko, J., " Investigation of he Effects of Hydrogen Addition on Lean Extinction in a Swirl Stabilized Combustor", Proceeding of Combustion Institute, 2006

[30] Lefebvre, A. H., " Gas Turbine Combustion", 2nd edition, Taylor&Francis, New York, 1999

[31] Zhang, Q., Noble, D.R., Meyers, A., Xu, K., Lieuwen, T., "Characterization Of Fuel Composition Effects In H2/CO/CH4 Mixtures Upon Lean Blowout", ASME Paper # GT2005-689017

[32] Lewis, B. and von Elbe, G., Combustion, flames and explosions of gases, 3rd edition, New York, Academic Press, 1987.

[33] Whol, K, "Quenching, Flashback,Blowoff-Theory and Experiment", pp68-89

[34] Krevelen., D. W. V., Chermin, H.A.G., " Generalized Flame Stability Diagram for the Predictino of Interchangeability of Gases", pp358-367

[35] Driscoll, J. F., Rasmussen, C. C., " Correlation and Analysis of Blowout Limits of Flames in High speed Airflows", Journal of Propulsion and Power, v21,No.6,2005,pp 1035-1044

[36] Kido, Hiroyuki, Nakahara, Masaya, Nakashima, Kenshiro, Hashimoto, Jun, “Influence of local flame displacement velocity on turbulent burning velocity”, Proc. Comb. Inst., Vol. 29, 2002, pp. 1855-1861

[37] Paul Clavin, “Dynamic Behavior of Premixed Flame Fronts in Laminar and Turbulent Flows”, Prog. Energy Comb. Sci.,Vol.11,1985,pp.1-59

[38] Chen, Jacqueline H., Im, Hong G., “Stretch Effects on the Burning Velocity of Turbulent Premixed Hydrogen/Air Flames”, Proc. Comb. Inst., Vol. 28, 2000, ,pp 211-218

[39] Maloney, D., “The Simulation Validation Project at NETL”, DOE Report, 2002.

[40] Schefer, R. W., “Hydrogen Enrichment for Improved Lean Flame Stability”, International Journal of Hydrogen Energy, 28, 2003, pp. 1131-1141.

[41] Wicksall, D., Agrawal, A., “Effects of Fuel Composition on Flammability Limit of a Lean, Premixed Combustor”, ASME Paper #2001-GT-0007

[42] Griebel, P., Boschek, E., Jansohn, P., “ Lean blowout Limits and NOx emissions of turbulent Lean Premixed Hydrogen-Enriched Methane/Air Flames at High Pressure”, Turbo Expo 2006, GT 2006-90490.

[43] Schefer, R. W., Wicksall, D. M., Agrawal, A.K., “Combustion of Hydrogen-Enriched Methane in a Lean Premixed Swirl-Stabilized Burner”, Proc. Comb. Inst., 29th, pp.843-851

[44] Yoshimura, T., McDonell, V., Samuelsen, S., “ Evaluation of Hydrogen Addition to Natural Gas on the Stability and Emission behavior of a Model Gas Turbine Combustor”, ASME paper GT2005-68785

[45] Vagelopoulos, C.M., Egolfopoulos, F.N., “Laminar Flame Speeds and Extinction Strains Rates of Mixtures of Carbon Monoxide with Hydrogen, Methane, and Air”, Proc. Comb. Inst., 1994, pp 1317

[46] Ren., J.Y., Qin, W., Egolfopoulos, F. N., Tsotsis, T. T., "Strain-rate Effects on Hydrogen-enhanced Lean Premixed Combustion", Combustion and Flame, v124, 717-720,2001

[47] Sankaran, Ramanan, Im, Hong G, "Dynamic Flammability Limits of Methane/Air Premixed Flames with Mixture Composition Fluctuations", Proc. Comb. Inst., Vol. 29, 2002, ,pp. 77-84

[48] Jackson, Gregory S., Sai, Roxanne, Plaia, Josephi M., Boggs, Christopher M., Kiger, Kenneth T., , "Influence of H2 on the Response of Lean Premixed CH4 Flames to High Strained Flows", Comb. Flame,, 132, 2003, pp. 503-511

[49]Nicholson, H. and Field, J., "Some Experimental Techniques for the Investigation of the Mechanism of Flame Stabilization in the Wake of Bluff Bodies," *Proc. Comb. Inst*., Vol. 3, 1951, pp. 44-68.

[50]Hertzberg, J. R., Shepherd, I. G., and Talbot, L., "Vortex Shedding Behind Rod Stabilized Flames," Combustion and Flame, Vol. 86, 1991, pp. 1-11.

[51] Hedman, P. O., Fletcher, T. H., Graham, S. G., Timothy, G. W., Flores, D. V., and Haslam, J. K., "Observations of Flame Behavior in a Laboratory-Scale Premixed Natural Gas/Air Gas Turbine Combustor from PLIF measurements of OH," ASME Paper GT-2002-30052, 2002.

[52] Norton, D. G., "Combustion characteristics and flame stability at the microscale: A CFD study of premixed methane/air mixtures," Chemical Engineering Science, Vol. 58 (21), 2003, pp. 4871-4882.

[53]Muruganandam, T., "Sensing and Dynamics of Lean blowout in a Swirl Dump Combustor", Ph. D. thesis , Georgia institute of Technology, 2006

[54]Law, C.K., Zhu, D.L. and Yu, G., "Propagation and extinction of stretched premixed flames", Proc. Combust. Inst., 21 (1986) 1419-1426

[55]Ramanan, S., Im, Hong. G. " Effect of Hydrogen Additions on Flammability Limit of Stretched Methane/Air Premixed Flames", Proceedings of 3rd Joint Meeting of U.S. section of Combustion Institute, 2003

[56] Bradley, D., Gaskell, P.H., Gu, X.J., Sedaghat, A., " Premixed Flamelet Modeling: Factors Influencing the Turbulent Heat Release Rate Source Term and the Turbulent Burning Velocity", Combust Flame, 143, 2005, 227-245

[57] Bradley D., Gaskell, P.H., Gu., X.J., " Burning Velocities, Markstein Lengths, and Flame Quenching for Spherical Methane-Air Flames: A Computational Study", Combust Flame, 104, 1996, 176-198

[58] Chung, S.H., Chung, D.H., Fu, C., Cho, F., " Local Extinction Karlovitz Number for Premixed Flames", Combust Flame, 106, 1996, 515-520

[59] Smooke, M.D., " On the Use of Adaptive Methods in Premixed Combustion", American Institute of Chemical Engineers, 1984, pp 25.

[60]Stahl, G., and Warnatz, G., "Numerical Investigation of Time-Dependent Properties and Extinction of Strained Methane--- and Propane-air Flamelets", Combust Flame, 85 285 1991

[61] Kee, R.J., Miller, J.A., Evans, G.H., and Dixon-Lewis,D., "A Computational Model of the Structure and Extinction of Strained, Opposed Flow, Premixed Methane-Air Flames", Proc. Combust. Inst., 22 (1990) 1479-1494

[62] Echekki, T, and Mungal, M.G., "Flame Speed Measurements at the Tip of a Slot Burner: Effects of Flame Curvature and Hydrodynamic Stretch", Proc. Combust. Inst., 23 (1990) 455-461

[63] Wagner, T.C., and Ferguson, C.R., "Bunsen Flame Hydrodynamics", Combust Flame,59, 1985, 267-272

[64] Karlovitz, B., Denniston Jr., D.W., Knapschaefer, D.H., Wells, F.E., "Studies on Turbulent Flames: A. Flame Propagation Across Velocity Gradients B. Turbulence Measurement in Flames", Proc. Combust. Inst., 4 (1953) 613-620

[65]Nair, S., Lieuwen, T., "Near-Blowoff Dynamics of a Bluff-body Stabilized Flame", Journal of Propulsion and power, v (2) (2007) 421-427

[66]Khosla, S. , Leach, T. and Smith, C., "Flame Stabilization and Role of von Karman Vortex Shedding Behind Bluff Body Flame Holders", AIAA-2007-5653, 2007

[67] Hong. G. Im, J.H. Chen, Combust Flame, "Preferential Diffusion Effects on the Burning Rate of Iinteracting Turbulent Premixed Hydrogen-Air Flames", 131 (3) (2002) 246-258

[68] J.H. Chen, Hong. G. Im, “Stretch Effects on the Burning Velocity of Turbulent Premixed Hydrogen/air Flames”, Proc. Combust. Inst., 28 (2000) 211-218

[69] J.F. Sriscoll, D.J. Sutkus, W.L. Roberts, M.E. Post, L.P. Goss, Combustion Science and Technology, 96 (4-6) (1994) 213-229

70] J.M. Donbar, J.F. Driscoll, C.D. Carter, Combust. Flame, “Strain Rates Measured Along the Wrinkled Flame Contour within Turbulent non-premixed Jet Flames”, 125 (2001) 1239-1257

[71] Lieuwen, T., Torres, H., Johnson, C., Daniel, B.R., Zinn, B.T., “A Mechanism for Combustion Instabilities in Lean Premixed Gas Turbine Combustors”, Journal of Engineering for Gas Turbines and Power, 123(1), 2001, pp. 182-190

[72] Williams, T. C., Schefer, R. W., Oefelein, J. C. and Shaddix, C. R., “An Idealized Gas Turbine Combustor for Performance Research and Validation of Large Eddy Simulations”, Review of Scientific Instruments (submitted) 2006

[73] Lilley, D. G., “ Swirl Flows in Combustion: a Review”, AIAA J. vol 15, No. 8, 1977

74 Raffel, M., Willert, C. and Kompenhans, J. “Particle image Velocimetry: A Practical Guide”, Springer, 1998 (3rd edition).

[75] J. Natarajan, S. Nandula, T. Lieuwen and J. Seitzman, “Laminar Flame Speeds of Synthetic Gas Fuel Mixtures”, ASME Paper # GT2005-68917.

[76] Kee RJ, Warnatz J, Miller Ja. “A FORTRAN Computer Code Package for the Evaluation of Gas-Phase Viscosities, Conductivities, and Diffusion Coefficients.” Technical Report SAND89-8009, Sandia National laboratories, 1983.

[77] G.Joulin, T.Mitani, “ Linear Stability Analysis of Two-Reactant Flame”, Comb. Flame,40,1981,pp.235-246

[78] Masaya Nakahara, Hiroyuki Kido, “ A Study of the Premixed Turbulent Combustion Mechanism Taking the Preferential Diffusion Effect into Consideration”, Memoirs of the Faculty of Engineering, Kyushu Univ., 58, 1998

[79] Yang, V., Huang, Y., “Bifurcation of Flame Structure in a Lean-Premixed Swirl-Stabilized Combustor: Transition from Stable to Unstable Flame”, Comb. Flame, 136, 2004, pp. 383-389

[80] Bradley, D., Gaskell, P. H., Gu, X. J., Lawes, M., Scott, M. J., “Premixed Turbulent Flame Instability and NO Formation in a Lean-Burn Swirl Burner”, Comb. Flame, 115, 1998, pp. 515-538

[81] Huang, Ying, Yang, Vigor, “ Swirling Flow Structures and Flame Characteristics in a Lean –Premixed Combustor”, AIAA-2004-0978

[82] Ji, Jun, Gore P. Jay, “Flow Structure in lean Premixed Swirling Combustion”, Proc. Comb. Inst., Vol. 29, 2002, pp. 861-867

[83] Filatyev, S.A., Driscoll, J.F., Carter, C.D., Donbar, J.M., “Measured Properties of Turbulenct Premixed Flames for Model Assessment, including Burning Velocities, Stretch Rates, and Surface Densities”, Comb. Flame, 141, 2005, pp. 1-21